Chapter 7

Magnetic Resonance (MR) Image Reconstruction

ch,mr

Contents

s,mr,intro

7.1 Introduction (s,mr,intro)

In Chapter 6 it was assumed that the measurements are samples of the Fourier transform of the unknown object $f(\vec{\mathrm{x}})$. That model is reasonable for some types of magnetic resonance (MR) scans, and many MR reconstruction methods are based on that model. However, for MR scans with long readout times, such as those used in fMRI, there are **relaxation effects** and/or **off-resonance effects** that depart from the simple Fourier model. This chapter discusses MR image reconstruction methods in the presence of such effects. [44, 45].

s,mr,model

7.2 Model (s,mr,model)

In the presence of **relaxation effects** and/or **off-resonance effects** a reasonably realistic model for MR measurements $\boldsymbol{y} = (y_1, \dots, y_{n_\mathrm{d}})$ is the following:

$$y_i = s(t_i) + \varepsilon_i, \qquad i = 1, \dots, n_\mathrm{d},$$

$$s(t) = \int_{\mathcal{D}} f(\vec{\mathrm{x}}) \, \mathrm{e}^{- z(\vec{\mathrm{x}}) \, t} \, \mathrm{e}^{-\imath 2\pi \vec{k}(t) \cdot \vec{\mathrm{x}}} \, \mathrm{d}\vec{\mathrm{x}}, \tag{7.2.1}$$

e,mr,st

where $\mathcal{D}$ denotes the object FOV and the complex quantity $z(\vec{\mathrm{x}})$ can include both relaxation effects and off-resonance effects as follows:

$$z(\vec{\mathrm{x}}) = \alpha(\vec{\mathrm{x}}) + \imath \, \omega(\vec{\mathrm{x}}) \, .$$

The real function $\alpha(\vec{\mathrm{x}})$ corresponds to the relaxation term (*e.g.*, an R_2^* map) at spatial position $\vec{\mathrm{x}}$, and the real function $\omega(\vec{\mathrm{x}})$ corresponds to the field inhomogeneity (*e.g.*, susceptibility) effect. Because both $\alpha(\vec{\mathrm{x}})$ and $\omega(\vec{\mathrm{x}})$ have inverse time units, we refer to $z(\vec{\mathrm{x}})$ as the ***rate map*** hereafter. For simplicity here, we address the problem where the *rate map* $z(\vec{\mathrm{x}})$ is known, *i.e.*, where we are given relaxation maps $\alpha(\vec{\mathrm{x}})$ and field maps $\omega(\vec{\mathrm{x}})$ and the goal is to reconstruct the object f from the measurements $\boldsymbol{y}$, *e.g.*, [59]. For field-corrected MR reconstruction, usually one assumes that $\alpha(\vec{\mathrm{x}})$ is zero. Numerous papers have addressed this problem; for an overview see [59]. Further applications of the general approach described here include situations where either the field map $\omega(\vec{\mathrm{x}})$ is unknown and also to be estimated, *e.g.*, [60–62], or the relaxation map $\alpha(\vec{\mathrm{x}})$ is also to be estimated, *e.g.*, [63, 64] or both, *e.g.*, [65–69]. We also focus on the case of a single receiver coil imaging although the methods extend readily to sensitivity encoded imaging with multiple receiver coils, *e.g.*, [70].

Failure to compensate for off-resonance effects leads to geometric distortions in echo-planar imaging, *e.g.*, [71, 72] and blurring when imaging with non-Cartesian trajectories.

We parameterize the object $f(\vec{\mathrm{x}})$ using a linear combination of n_p basis functions:

$$f(\vec{\mathrm{x}}) = \sum_{j=1}^{n_\mathrm{p}} x_j \, b(\vec{\mathrm{x}} - \vec{\mathrm{x}}_j) \, . \tag{7.2.2}$$

e,mr,basis

So the image reconstruction problem becomes that of estimating the parameter vector $\boldsymbol{x} = (x_1, \dots, x_{n_\mathrm{p}})$. For simplicity, we focus on rect functions (the voxel basis). We also assume that the *rate map* has (approximately) constant values over each voxel, so we can write

$$z(\vec{\mathrm{x}}) = \sum_{j=1}^{n_\mathrm{p}} z_j \, b(\vec{\mathrm{x}} - \vec{\mathrm{x}}_j),$$

where

$$z_j = \alpha(\vec{\mathrm{x}}_j) + \imath \, \omega(\vec{\mathrm{x}}_j), \qquad j = 1, \dots, n_\mathrm{p}. \tag{7.2.3}$$

e,mr,zj

For cases where the within-voxel gradients of the *rate map* are significant, one can use reduced voxel sizes to reduce signal loss [73] [74, p. 140]. However, such "over sampling" will increase computation. An alternative approach is proposed in §7.7 below.

Under these assumptions, the integral signal model (7.2.1) simplifies to the following sum[1]:

$$\bar{y}_i(\boldsymbol{x}) = \mathsf{E}[y_i] = B_i \sum_{j=1}^{n_\mathrm{p}} x_j \, \mathrm{e}^{-z_j t_i} \, \mathrm{e}^{-\imath 2\pi \vec{\nu}_i \cdot \vec{\mathrm{x}}_j} \, , \tag{7.2.4}$$

e,mr,ybi

[1] In problems where z_j is estimated by linearization, an extra "t_i" term appears in the summation [69]. One can absorb this into B_i and then all remaining formulas are also applicable to such problems.

where $\vec{\nu}_i = \vec{k}(t_i)$ denotes the (possible nonuniform) k-space sample locations, $B(\vec{\nu})$ denotes the $\bar{d}$-dimensional Fourier transform of $b(\vec{\mathrm{x}})$, and we define

$$B_i = B(\vec{\nu}_i) = \int b(\vec{\mathrm{x}}) \, \mathrm{e}^{-\imath 2\pi \vec{\nu}_i \cdot \vec{\mathrm{x}}} \, \mathrm{d}\vec{\mathrm{x}} \,.$$

In matrix-vector form:

e,mr,A

$$\bar{\boldsymbol{y}}(\boldsymbol{x}) = \boldsymbol{A}\boldsymbol{x}, \qquad \boldsymbol{A} = \{a_{ij}\}\,, \tag{7.2.5}$$

e,mr,aij

$$a_{ij} = B_i \, \mathrm{e}^{-z_j t_i} \, \mathrm{e}^{-\imath 2\pi \vec{\nu}_i \cdot \vec{\mathrm{x}}_j} \,. \tag{7.2.6}$$

Typically the matrix $\boldsymbol{A}$ is too large to be stored explicitly, so we would like to use procedures like FFT operations to evaluate $\boldsymbol{A}\boldsymbol{x}$, rather than explicit matrix-vector multiplication. Unfortunately, $\boldsymbol{A}$ is not a Fourier matrix in general. In any case, the MR reconstruction problem is to reconstruct $\boldsymbol{x}$ from $\boldsymbol{y}$ using (7.2.5).

7.3 Regularized LS reconstruction

Because MR measurements have white complex gaussian noise, we focus on methods that form an estimate $\hat{\boldsymbol{x}}$ of $\boldsymbol{x}$ by minimizing regularized least-squares cost functions of the form

e,mr,model,kost

$$\Psi(\boldsymbol{x}) = \frac{1}{2} \left\| \boldsymbol{y} - \bar{\boldsymbol{y}}(\boldsymbol{x}) \right\|^2 + \mathsf{R}(\boldsymbol{x}), \tag{7.3.1}$$

where $\mathsf{R}(\boldsymbol{x})$ denotes a roughness penalty function. (An unweighted norm is used in the usual case where the measurements have equal variances, although the approach generalizes readily to weighted norms.) Now the goal is to find the image $\hat{\boldsymbol{x}}$ that minimizes this cost function, typically by using gradient-based iterative algorithms. Most of the work in such algorithms is in computing the gradient of Ψ, and we focus on this computation hereafter.

One way to write the gradient of Ψ is:

e,mr,grad1

$$\nabla \Psi(\boldsymbol{x}) = -\boldsymbol{A}'(\boldsymbol{y} - \boldsymbol{A}\boldsymbol{x}) + \nabla \mathsf{R}(\boldsymbol{x}) \,. \tag{7.3.2}$$

The computational bottleneck in this expression is the calculation of the matrix-vector products $\boldsymbol{A}\boldsymbol{x}$ and $\boldsymbol{A}'\,\boldsymbol{r}$, where $\boldsymbol{r}$ denotes the residual $\boldsymbol{y} - \boldsymbol{A}\boldsymbol{x}$. Our previous approach [59] used the above gradient expression and combined NUFFTs [75] with temporal interpolation based on a "time-segmentation" approximation [76] so as to be able to compute efficiently $\boldsymbol{A}\boldsymbol{x}$ and $\boldsymbol{A}'\,\boldsymbol{r}$. We refer to (7.3.2) as the "**NUFFT approach**."

MIRT *NUFFT software is available [75]. See the* `nufft` *folder.*

An alternative, mathematically equivalent gradient expression is the following:

e,mr,grad2

$$\nabla \Psi(\boldsymbol{x}) = \boldsymbol{T}\boldsymbol{x} - \boldsymbol{b} + \nabla \mathsf{R}(\boldsymbol{x}), \tag{7.3.3}$$

where $\boldsymbol{T} = \boldsymbol{A}'\boldsymbol{A}$ and $\boldsymbol{b} = \boldsymbol{A}'\boldsymbol{y}$. Because $\boldsymbol{T}$ is Toeplitz when the *rate map* is zero, with some abuse of terminology we refer to (7.3.3) as the "**Toeplitz approach**." In the context of solving the LS problem $\min_{\boldsymbol{x}} \|\boldsymbol{y} - \boldsymbol{A}\boldsymbol{x}\|$, conventional wisdom would advise *against* using the **normal equations** $\boldsymbol{A}'\boldsymbol{A}\boldsymbol{x} = \boldsymbol{A}'\boldsymbol{y}$, because the condition number of $\boldsymbol{A}$ is squared: $\mathrm{cond}(\boldsymbol{A}'\boldsymbol{A}) = \mathrm{cond}^2(\boldsymbol{A})$, potentially leading to increased sensitivity to noise. and perhaps slower convergence rates. However, when $\boldsymbol{A}$ is ill-conditioned, *e.g.*, for irregular frequency sample locations, we should include appropriate regularization $\mathsf{R}(\boldsymbol{x})$ so that $\boldsymbol{A}'\boldsymbol{A} + \nabla^2 R$ is reasonably well-conditioned, in which case (7.3.3) need not be problematic.

Here, we first revisit and generalize the approximations used in evaluating (7.3.2). We then consider methods for computing efficiently the gradient expression (7.3.3). We then provide numerical results showing that using the Toeplitz approach (7.3.3) can reduce the compute time significantly relative to the NUFFT approach (7.3.2) while preserving image quality.

An interesting *open problem* is whether the recursive form (1.10.16) could be combined with FFT approaches to form an efficient iterative algorithm, somewhat akin to those in [77, 78].

7.4 Approximations for exponentials (s,mr,approx)

s,mr,approx

The problematic part of the expression (7.2.6) for the elements of the matrix $\boldsymbol{A}$ is the exponential terms $\mathrm{e}^{-z_j t_i}$. Direct implementation of $\boldsymbol{A}\boldsymbol{x}$ using (7.2.4) would require $O(n_{\mathrm{p}} n_{\mathrm{d}})$ computations, which is undesirably slow. To reduce computation, one must make approximations. We first review the previously proposed approximations for the exponential terms, and then describe a unified framework in which to propose new approximations.

7.4.1 Time segmentation (TS) approximations

In the context of MR reconstruction with field inhomogeneity correction, Noll et al. proposed to evaluate the exponentials $\mathrm{e}^{-z_j t_i}$ at a predetermined set of time points, $\{\check{t}_l : l = 1, \dots, L\}$, and then to use a linear interpolation method for times between those points [76, 79]. In our context, we can express this "**time segmentation**" approach as the following approximation:

$$\mathrm{e}^{-zt} \approx \sum_{l=1}^{L} b_l(t)\, \mathrm{e}^{-z\check{t}_l}, \qquad z \in \mathbb{C},$$

where each $b_l(t)$ denotes a temporal interpolator. Traditionally, shift-invariant temporal interpolators such as Hanning functions have been used [76]. These were generalized to min-max optimal temporal interpolators in [59], significantly reducing approximation error. (See §7.4.3.4 below.)

A limitation of the above approach is that it will incur approximation error even if the *rate map* $z(\vec{x})$ is completely uniform, if one uses conventional interpolators. To improve the time segmentation approach, one can first select a nominal *rate map* value $\bar{z}$ and then use following approximation:

$$\mathrm{e}^{-zt} \approx \mathrm{e}^{-\bar{z}t} \sum_{l=1}^{L} b_l(t)\, \mathrm{e}^{-(z-\bar{z})\check{t}_l}.$$

This "baseline-offset time segmentation" approach reverts to the classical method if one chooses $\bar{z} = 0$. Alternatively, if $z(\vec{x})$ is uniform with value $\bar{z}$, then the above approximation becomes exact if we choose $L = 1$ and $b_l(t_i) = 1$. (The lack of such a baseline $\bar{z}$ term may in part explain the poor performance of the Hanning interpolator in [59].)

Both the classical approach and our baseline-offset time-segmentation approximations can be expressed as follows:

$$\mathrm{e}^{-z_j t_i} \approx \sum_{l=1}^{L} b_{il} c_{lj}, \qquad b_{il} \triangleq b_l(t_i)\, \mathrm{e}^{-\bar{z}t_i}, \qquad c_{lj} \triangleq \mathrm{e}^{-(z_j-\bar{z})\check{t}_l}. \tag{7.4.1}$$

e,mr,ezt,time

The approximation reduces computation because it contains no terms that depend on both i and j.

7.4.2 Frequency segmentation

Instead of choosing time samples, an alternative approach is to choose a set of "frequency" samples $\{\check{z}_l : l = 1, \dots, L\}$ and interpolate between these values to evaluate the exponential [79–81]. In our context, we can express this "**frequency segmentation**" approach as the following approximation:

$$\mathrm{e}^{-zt} \approx \mathrm{e}^{-z\bar{t}} \sum_{l=1}^{L} c_l(z)\, \mathrm{e}^{-\check{z}_l(t-\bar{t})}, \qquad t \in \mathbb{R},$$

where $\bar{t}$ is a nominal time reference (*e.g.*, an echo time) and where each $c_l(\cdot)$ denotes a frequency-domain interpolator. In particular, we have

$$\mathrm{e}^{-z_j t_i} \approx \sum_{l=1}^{L} b_{il} c_{lj}, \qquad b_{il} \triangleq \mathrm{e}^{-\check{z}_l(t_i-\bar{t})}, \qquad c_{lj} \triangleq c_l(z_j)\, \mathrm{e}^{-z_j\bar{t}}. \tag{7.4.2}$$

e,mr,ezt,freq

The classical approach uses $\bar{t} = 0$, but this choice may be suboptimal unless the interpolators c_{lj} are chosen carefully.

In the original version [79], the c_{lj} values were chosen to be either nearest-neighbor, linear, or Hanning interpolators, and the choice $L > \frac{4}{\pi}\frac{\omega_{\max}-\omega_{\min}}{2}(t_{n_\mathrm{d}} - t_1)$ was recommended. (See also [82].) Later, Man et al. described a least-squares approach (*cf.* (7.4.6) below) to choosing the interpolation functions $c_l(\cdot)$ for the frequency-segmentation approach [81], and recommended choosing $L > \frac{1}{\pi}\frac{\omega_{\max}-\omega_{\min}}{2}(t_{n_\mathrm{d}} - t_1)$, for uniformly spaced $\check{z}_l$ values.

In the frequency segmentation approach, a practical issue is choosing the frequency samples $\{\check{z}_l\}$. The traditional choice is to use equally-spaced frequencies that span the range of frequencies in the field map. As shown in §7.4.5, that choice is suboptimal for nonuniform field map distributions. Instead, it is preferable to concentrate more frequency components where they are most needed based on the *rate map* histogram. (When the z_j values are complex, a 2D histogram is needed with separate axes for the real and imaginary components.) One expedient choice uses the asymptotic theory of quantization, which specifies the optimal density of centroids for high-rate quantization [83]. Another option is to use the iterative Lloyd-Max algorithm for scalar quantizer design to find an "optimal" set of L

frequency values. (When the relaxation map is nonzero, one could could use the LBG algorithm for two-component vector quantization.) To reduce computation, one can first finely quantize the z_j values and then apply *weighted* versions of Lloyd-Max or LBG to choose the $\check{z}_l$ quickly.

MIRT *See* `lloyd_max_hist.m` *and* `highrate_centers.m`.

7.4.3 Generalized approximations

Comparing (7.4.1) and (7.4.2), we see that both "time segmentation" and "frequency segmentation" lead to approximations of the form

$$\mathrm{e}^{-z_j t_i} \approx \sum_{l=1}^{L} b_{il} c_{lj}, \qquad j = 1, \dots, n_\mathrm{p}, \qquad i = 1, \dots, n_\mathrm{d}, \tag{7.4.3}$$

e,mr,ezt,cd

but with different choices for the b_{il} and c_{lj} terms. Substituting such an approximation into the discrete signal model (7.2.4) and rearranging yields

$$\bar{y}_i(\boldsymbol{x}) = [\boldsymbol{A}\boldsymbol{x}]_i \approx B_i \sum_{l=1}^{L} b_{il} \left[\sum_{j=1}^{n_\mathrm{p}} (x_j c_{lj}) \, \mathrm{e}^{-\imath 2\pi \vec{\nu}_i \cdot \vec{\mathrm{x}}_j} \right]. \tag{7.4.4}$$

e,mr,ybi,cd

In matrix form,

$$\boldsymbol{A} \approx \mathsf{diag}\{B_i\} \sum_{l=1}^{L} \mathsf{diag}\{b_{il}\} \, \boldsymbol{G} \, \mathsf{diag}\{c_{lj}\},$$

where $\boldsymbol{G}$ denotes the $n_\mathrm{d} \times n_\mathrm{p}$ NUFFT operator having elements $g_{ij} = \mathrm{e}^{-\imath 2\pi \vec{\nu}_i \cdot \vec{\mathrm{x}}_j}$. We can evaluate this expression efficiently using L NUFFT calls, because the inner bracketed expression is an NUFFT of the signal $(x_1 c_{l1}, \dots, x_{n_\mathrm{p}} c_{l n_\mathrm{p}})$. Thus, from the point of view of rapid computation, time segmentation and frequency segmentation are equally viable methods, and are both special cases of the general form (7.4.3). For a given L, *any* choices for the b_{il} and c_{lj} terms lead to the same compute time for evaluating $\boldsymbol{A}\boldsymbol{x}$ and $\boldsymbol{A}'\boldsymbol{y}$.

Because compute times are determined only by L (and n_p and n_d), rather than by the form of b_{il} and c_{lj}, we should choose the b_{il} and c_{lj} terms to *minimize the error* in the approximation (7.4.3). Let $\boldsymbol{B} = \{b_{il}\} \in \mathbb{C}^{n_\mathrm{d} \times L}$ and $\boldsymbol{C} = \{c_{lj}\} \in \mathbb{C}^{L \times n_\mathrm{p}}$. We would like to find choices for $\boldsymbol{B}$ and $\boldsymbol{C}$ that are "optimal" in some sense, without necessarily being constrained to the exponential forms used in (7.4.1) and (7.4.2).

The possibility of using non-exponential bases was explored in [81] using SVD analysis. However, that investigation used equally weighted, equally-spaced frequency samples, which corresponds implicitly to *rate maps* having uniform distributions (a rectangular histogram). The next subsections describe some possible approaches for designing $\boldsymbol{B}$ and $\boldsymbol{C}$ for *patient-specific rate maps*, which in general do not have uniform distributions. The work in [81] focused on conjugate-phase reconstruction, where the approximations are used only once. In contrast, in iterative image reconstruction the approximations are used every iteration, so it can be beneficial to design improved interpolators prior to iterating.

7.4.3.1 Min-max approximations

In the spirit of previous min-max methods [59, 75], one approach to choosing $\boldsymbol{B}$ and $\boldsymbol{C}$ would be to try to minimize the worst-case error using a min-max criterion:

$$\arg\min_{\boldsymbol{B},\boldsymbol{C}} \max_{ij} \left| \mathrm{e}^{-z_j t_i} - \sum_{l=1}^{L} b_{il} c_{lj} \right|.$$

In matrix notation, we have

$$\arg\min_{\boldsymbol{B},\boldsymbol{C}} \| \boldsymbol{E} - \boldsymbol{B}\boldsymbol{C} \|_\infty,$$

where $\boldsymbol{E}$ is the $n_\mathrm{d} \times n_\mathrm{p}$ matrix with elements $e_{ij} = \mathrm{e}^{-z_j t_i}$. We are unaware of an efficient algorithm for solving this min-max problem. Efficient solutions are essential because we may wish to redesign $\boldsymbol{B}$ and $\boldsymbol{C}$ for each object's *rate map*.

7.4.3.2 Weighted least-squares approximations

A simpler alternative would be to minimize the **Frobenius norm**

$$\arg\min_{\boldsymbol{B},\boldsymbol{C}} \|\boldsymbol{E} - \boldsymbol{B}\boldsymbol{C}\|_{\text{Frob}}^2 = \arg\min_{\boldsymbol{B},\boldsymbol{C}} \sum_{i=1}^{n_\text{d}} \sum_{j=1}^{n_\text{p}} \left| \mathrm{e}^{-z_j t_i} - \sum_{l=1}^{L} b_{il} c_{lj} \right|^2, \tag{7.4.5}$$

e,mr,BC,wls

or a weighted generalization thereof. This minimization is a "principal components" problem (see §26.12) that is solved by the **SVD** of $\boldsymbol{E}$. This solution can be of theoretical interest as a performance benchmark, but appears to require too much memory and computation for routine use.

Rather than optimizing both $\boldsymbol{B}$ and $\boldsymbol{C}$ jointly, one can first choose $\boldsymbol{B}$ heuristically and then find the matrix $\boldsymbol{C}$ that optimizes (7.4.5), or one can first choose $\boldsymbol{C}$ and then optimize $\boldsymbol{B}$. These two alternatives are explored next.

s,mr,hist,pc

7.4.3.3 Histogram principal components

For a given matrix $\boldsymbol{B}$, the LS-optimal choice of $\boldsymbol{C}$ is given by

$$\boldsymbol{c}_j = [\boldsymbol{B}'\boldsymbol{B}]^{-1}\boldsymbol{B}'\boldsymbol{e}_j, \tag{7.4.6}$$

e,mr,approx,vc,ls

where $\boldsymbol{e}_j = (\mathrm{e}^{-z_j t_1}, \dots, \mathrm{e}^{-z_j t_{n_\text{d}}})$ is the jth column of $\boldsymbol{E}$ and $\boldsymbol{c}_j = (c_{1j}, \dots, c_{Lj})$ is the jth column of $\boldsymbol{C}$. If the columns of $\boldsymbol{B}$ are orthonormal, computing $\boldsymbol{c}_j$ becomes simply $\boldsymbol{c}_j = \boldsymbol{B}'\boldsymbol{e}_j$. Because there is no loss in generality in considering only choices for $\boldsymbol{B}$ having orthonormal columns, we now focus on choosing $\boldsymbol{B}$ efficiently.

Suppose we histogram the *rate map* values $\{z_j\}$ into $K \ll n_\text{p}$ bins with centers $\tilde{z}_k$, $k = 1, \dots, K$, possibly spaced unequally, and let h_k denote the number of z_j values in the kth bin. Then a natural approximation to (7.4.5) is the following WLS criterion:

$$\arg\min_{\boldsymbol{B}} \sum_{k=1}^{K} h_k \left\| \tilde{\boldsymbol{e}}_k - \boldsymbol{B}\boldsymbol{B}'\tilde{\boldsymbol{e}}_k \right\|^2, \tag{7.4.7}$$

e,mr,approx,hk

where $\boldsymbol{B}$ must have L orthonormal columns and we define $\tilde{\boldsymbol{e}}_k = (\mathrm{e}^{-\tilde{z}_k t_1}, \dots, \mathrm{e}^{-\tilde{z}_k t_{n_\text{d}}})$. The solution to this minimization problem is given by the first L singular vectors of the $n_\text{d} \times K$ matrix $\left[\sqrt{h_1}\tilde{\boldsymbol{e}}_1 \ \dots \ \sqrt{h_K}\tilde{\boldsymbol{e}}_K\right]$. (See §26.12.) Because $K \ll n_\text{p}$, this SVD is much more practical than (7.4.5).

A benefit of this approach is that we can examine the singular values to determine how many components L are needed to ensure a given desired approximation accuracy. In particular, if the *rate map* is uniform, using only one component will provide exact results, whereas conventional linear interpolation would require many sample points.

s,mr,lsts

7.4.3.4 Least-squares time-segmentation approach

Instead of optimizing over both $\boldsymbol{B}$ and $\boldsymbol{C}$, a simpler approach is to choose the matrix $\boldsymbol{C}$ that corresponds to the time segmentation approximation (7.4.1), and then optimize $\boldsymbol{B}$ by least squares [59]. (When $\boldsymbol{B}$ is thus optimized, the $\bar{z}$ term in (7.4.1) is unnecessary.) Letting $\boldsymbol{b}(t_i) = (b_1(t_i), \dots, b_L(t_i))$ denote the ith row of $\boldsymbol{B}$, we want

$$\boldsymbol{b}(t) = \arg\min_{\boldsymbol{b} \in \mathbb{C}^L} \sum_{j=1}^{n_\text{p}} \left| \mathrm{e}^{-z_j t} - \sum_{l=1}^{L} b_l \, \mathrm{e}^{-z_j \check{t}_l} \right|^2. \tag{7.4.8}$$

e,mr,approx,lsts,b

Slightly generalizing [59], the solution to this problem is

$$\boldsymbol{b}(t) = [\boldsymbol{X}'\boldsymbol{X}]^{-1}\boldsymbol{X}'\boldsymbol{e}(t), \tag{7.4.9}$$

e,mr,c,lsts

where the j,lth element of $\boldsymbol{X}$ is $\mathrm{e}^{-z_j \check{t}_l}$, *i.e.*, $\boldsymbol{X} = \boldsymbol{C}^T$, and $e_j(t) = \mathrm{e}^{-z_j t}$. Thus

$$[\boldsymbol{X}'\boldsymbol{e}(t)]_l = \sum_{j=1}^{n_\text{p}} \mathrm{e}^{-z_j^* \check{t}_l} \, \mathrm{e}^{-z_j t}, \qquad l = 1, \dots, L.$$

This can be computed in $O(n_\text{p} L)$ for each t_i. Similarly,

$$[\boldsymbol{X}'\boldsymbol{X}]_{l',l} = \sum_{j=1}^{n_\text{p}} \mathrm{e}^{-z_j^* \check{t}_{l'}} \, \mathrm{e}^{-z_j \check{t}_l}, \qquad l, l' = 1, \dots, L,$$

which can be computed in $O(n_\mathrm{p} L^2)$ independently of t_i. So overall, precomputing (prior to iterating) the interpolation matrix $\boldsymbol{B}$ requires $O(Ln_\mathrm{p}(n_\mathrm{d}+L)+L^3 n_\mathrm{d})$. If the z_j values are purely imaginary, then one can simplify the calculation further [59].

We have observed empirically that if the *rate map* consists of a finite number of components, *i.e.*, for each j we have $z_j \in \{\tilde{z}_1, \dots, \tilde{z}_K\}$, then the time segmentation approach works perfectly when $L = K$. Proving this property formally is an *open problem.*

7.4.3.5 Histogram-based time-segmentation approach

Instead of using all n_p *rate map* values in the LS criterion (7.4.8), we can reduce computation significantly by histogramming the *rate map* values and replacing the above sums over j with smaller weighted sums over the histogram bins [59]. Specifically, consider the following WLS criterion

$$\boldsymbol{b}(t) = \arg\min_{\boldsymbol{b} \in \mathbb{C}^L} \sum_{k=1}^{K} h_k \left| \mathrm{e}^{-\tilde{z}_k t} - \sum_{l=1}^{L} b_l \, \mathrm{e}^{-\tilde{z}_k \check{t}_l} \right|^2, \tag{7.4.10}$$

e,mr,approx,lsts,b,hist

where h_k was defined before (7.4.7). If we use $K \ll n_\mathrm{p}$ histogram bins, then the computation of $\boldsymbol{B}$ reduces to $O(LK(n_\mathrm{d} + L) + L^3 n_\mathrm{d})$. When the *rate map* z_j is purely imaginary, then one can use FFTs to further reduce computation in the usual case where the histogram bin centers are spaced equally [59, 81].

7.4.4 Approximation summary

The preceding subsections described a variety of possible methods for choosing the basis $\boldsymbol{B}$ and coefficient $\boldsymbol{C}$ matrices for approximating the exponential term $\mathrm{e}^{-z_j t_i}$ in (7.2.6). After using one of these choices, we can evaluate $\boldsymbol{A}\boldsymbol{x}$ and $\boldsymbol{A}'\boldsymbol{y}$ efficiently using (7.4.4), which requires L NUFFT calls. As demonstrated in [59], the approximation (7.4.4) enables practical gradient-based optimization to find the reconstructed image $\hat{\boldsymbol{x}}$.

For the methods described here, we have separated the problems of designing the "temporal" interpolators $\boldsymbol{B}$ and $\boldsymbol{C}$ and of designing the interpolators that are used in the frequency domain for the NUFFT operation. Whether one could design both interpolators simultaneously to improve accuracy (or reduce computation) is an interesting *open problem.* A starting point for such an approach would be the **Frobenius norm** designs considered by Neislony and Steidl [84], or the "type 3" NUFFT described by Lee and Greengard [85], who noted that

$$\mathrm{e}^{-\imath z_j t_i} \, \mathrm{e}^{-\imath 2\pi \vec{\nu}_i \cdot \vec{\mathrm{x}}_j} = \mathrm{e}^{-\imath \vec{u}_j \cdot \vec{v}_i}$$

where $\vec{u}_j \triangleq (z_j, \vec{\mathrm{x}}_j)$, $\vec{v}_i \triangleq (t_i, 2\pi\vec{\nu}_i)$. In other words, this is a $\bar{d}+1$-dimensional NUFFT problem! See also [86].

MIRT *See* `mri_exp_approx.m` *and* `Gmri.m`.

7.4.5 Evaluation of approximations (s,mr,eval)

s,mr,eval

We evaluated the approximations described in §7.4 using the four fieldmaps shown in Fig. 7.4.1. Two of the maps are synthetic; the first corresponding to a fieldmap with a discrete set of frequency offsets, and the second corresponding to a linear ramp in resonant frequency across the field of view. The other two maps were acquired using standard delayed-echo field mapping methods on a GE 3T MR scanner. One map was a brain slice at a level near the ear canals [87], whereas the other was a cylinder phantom to which metal had been attached to induce severe field inhomogeneity. Fig. 7.4.2 shows the histograms of these field maps.

For evaluation, we used t_i values with 5 μs sampling for $n_\mathrm{d} = 3770$, corresponding to a 18.855 ms readout time, which is typical for one-shot spiral trajectories on our 3T GE scanner for 64×64 brain scans with a 22 cm FOV.

Fig. 7.4.3 shows the normalized root mean-squared error (NRMSE), defined by $\frac{1}{n_\mathrm{p}} \|\boldsymbol{E} - \boldsymbol{B}\boldsymbol{C}\|_\mathrm{Frob}$ (see (7.4.5)), as a function of L for each of the four fieldmaps shown in Fig. 7.4.1. Naturally, as the number of approximation terms L increases, the error decreases. As expected, field maps that cover a larger range of resonant frequency offsets require larger values of L for adequate accuracy. In all cases, for any given L the SVD approach has the minimum error. We compared two approaches to choosing the frequency samples for the frequency segmentation (FS) method. We first tried uniformly spaced frequency samples; we found that this worked well *only* for the ramp phantom, which has a uniform field histogram. As an alternative, we applied the Lloyd-Max algorithm from scalar quantizer design to the fieldmap histograms to choose the frequency samples. This reduced error in all cases. For small values of L, the SVD method yielded much lower error than the time segmentation (TS) approximation with uniform time samples,

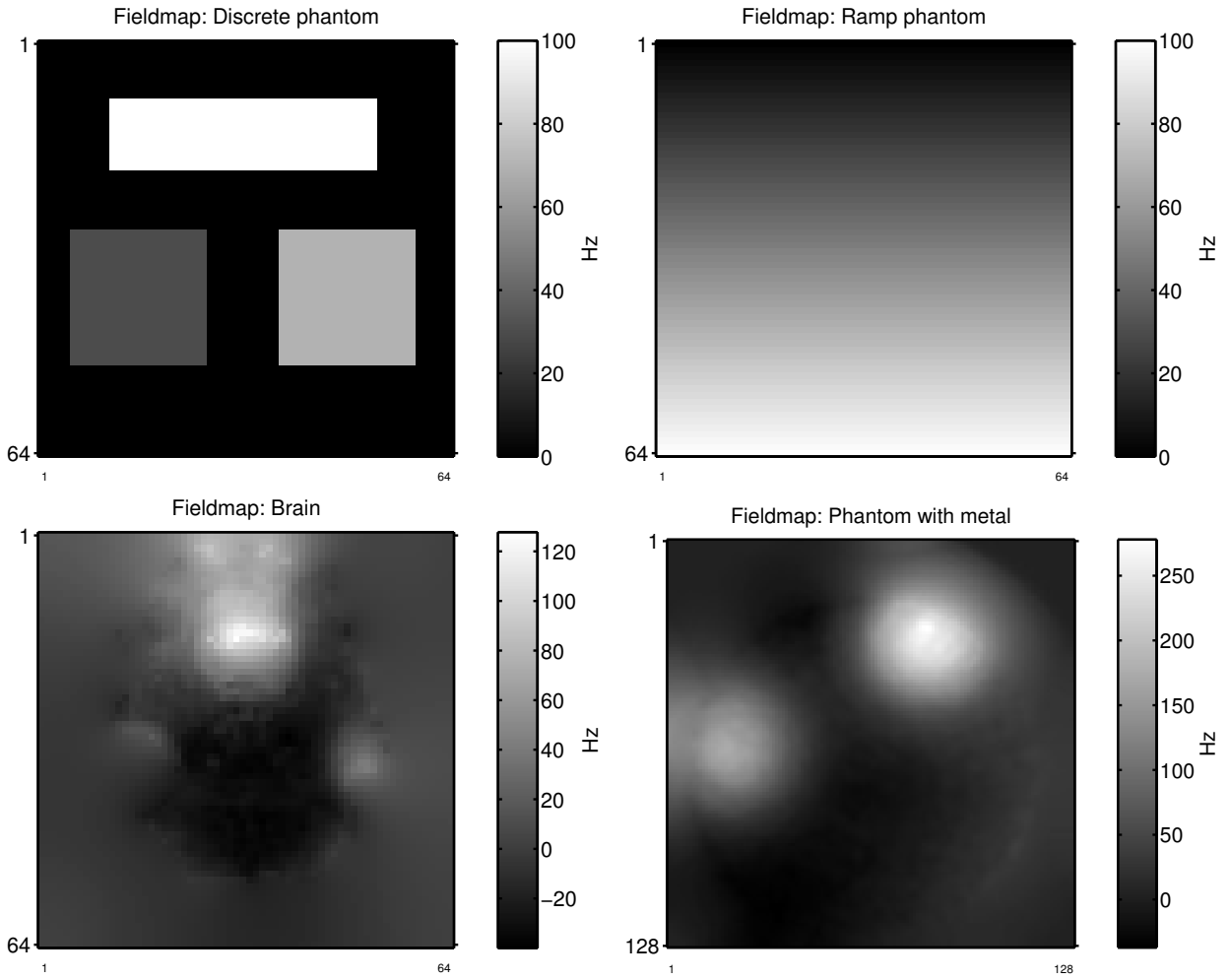

fig_mri_exp_maps

Figure 7.4.1: Four field maps used to evaluate the exponential approximations.

even though the TS approach had been optimized as described in §7.4.3.4. However, as L increased, the TS method approached the SVD accuracy, yet requires less computation for determining $\boldsymbol{B}$ and $\boldsymbol{C}$.

Fig. 7.4.4 shows the basis components $\boldsymbol{B}$ for the brain fieldmap for both the SVD approximation and for the time-segmentation approximation. The SVD components are approximately sinusoidal in nature, whereas the time-segmentation components are more sinc-like. It is interesting that despite the large differences between these bases, the approximation accuracies are very similar.

Table 7.1 shows the minimum value of L necessary to achieve a NRMSE value less than 0.01 for the four approximation methods shown in Fig. 7.4.3 and the four field maps shown in Fig. 7.4.1. Interestingly, the time segmentation (TS) method required exactly the same number of terms as the SVD method for all cases. From these representative results, we conclude that time segmentation approximations, when optimized as described in §7.4.3.4, are suitable for routine use, and $L < 10$ should be adequate for typical situations. This conclusion is fortuitous because the Toeplitz approach described in §7.5 is most efficient when implemented with the time segmentation approximations.

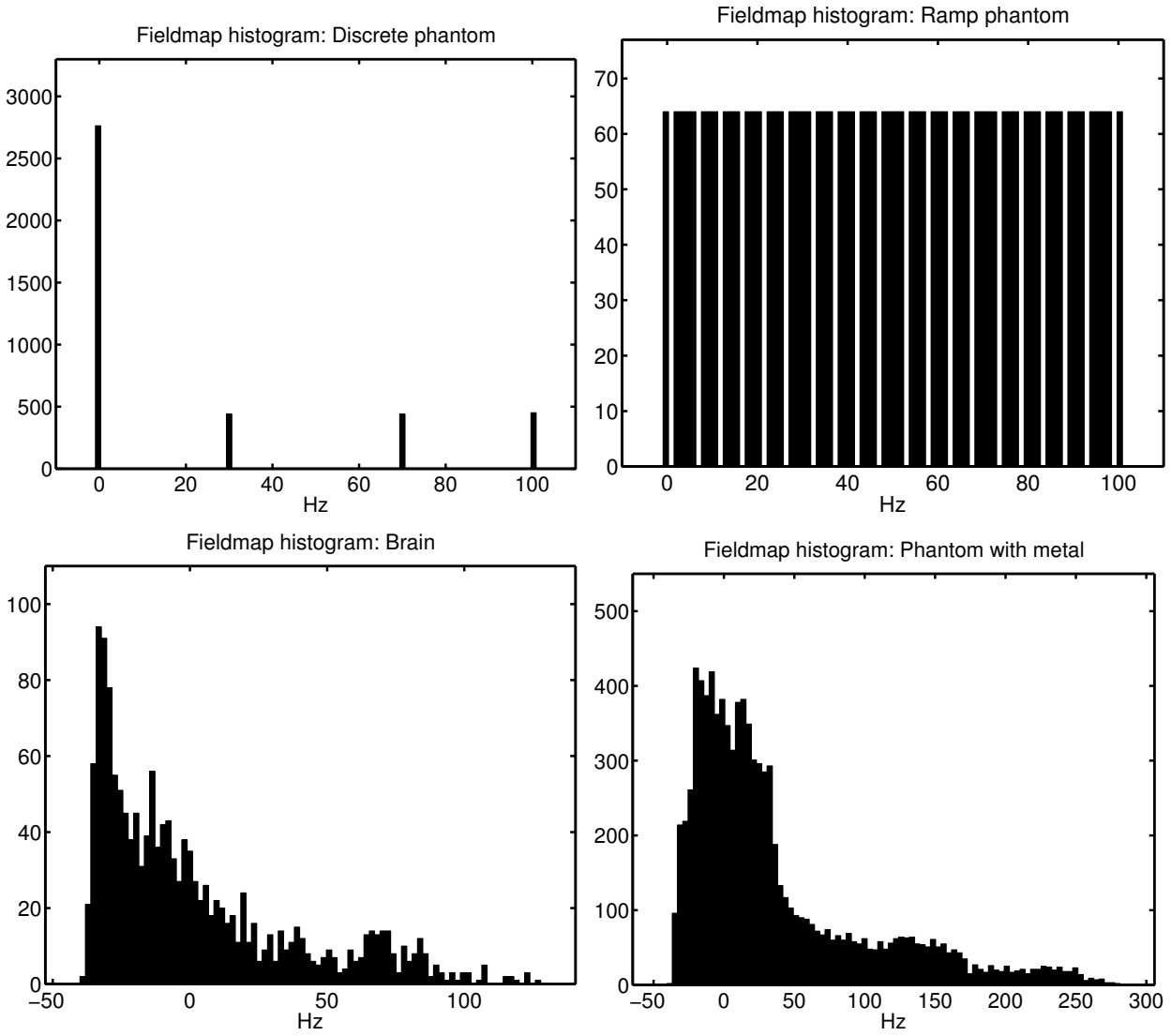

fig_mri_exp_hists

Figure 7.4.2: Histograms of the four field maps shown in Fig. 7.4.1.

	Approximation Method			
Phantom	FS uniform	FS quantized	TS uniform	SVD
Discrete phantom	6	4	4	4
Ramp phantom	5	5	5	5
Brain	7	6	6	6
Phantom with metal	11	10	9	9

Table 7.1: Minimum value of L necessary to achieve NRMSE < 0.01 for each approximation method and for the four field maps.

tab,mr,min,L

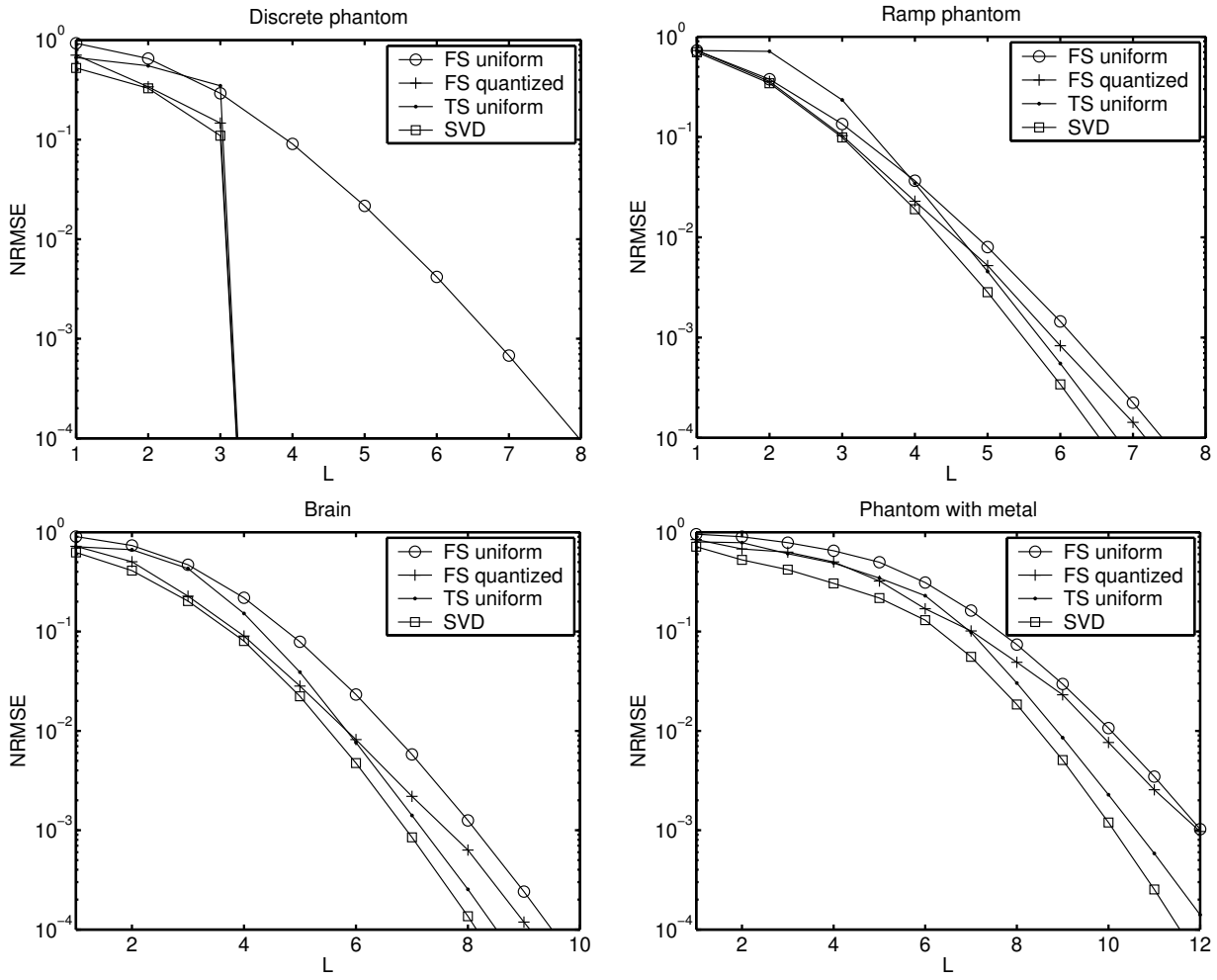

Figure 7.4.3: Normalized root mean-squared error (NRMSE) for various approximations of the exponentials $\mathrm{e}^{-z_j t_i}$, fig_mri_exp_nrmse
for the field maps shown in Fig. 7.4.1, for a 18.855 ms readout.

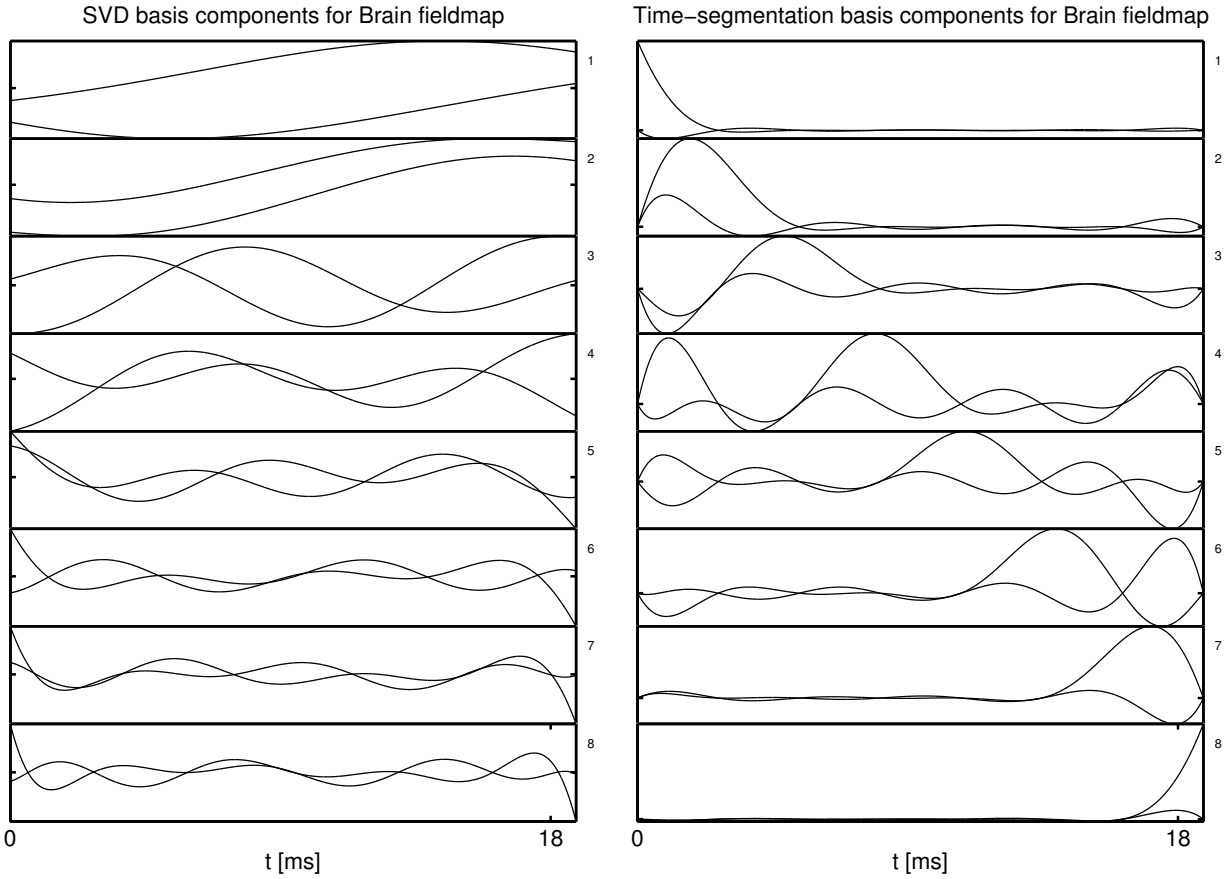

Figure 7.4.4: Basis components $\boldsymbol{B}$ for the brain field map for the SVD approximation and for the time-segmentation approximation. fig_mri_exp_basis

s,mr,toep

7.5 Toeplitz approach (s,mr,toep)

Now we turn to computing the "Toeplitz approach" (7.3.3) efficiently. Under the model (7.2.5), the matrix $\boldsymbol{T}$ in (7.3.3) has the following elements:

$$T_{kj} = [\boldsymbol{A}'\boldsymbol{A}]_{kj} = \sum_{i=1}^{n_\mathrm{d}} a_{ik}^* a_{ij} = \sum_{i=1}^{n_\mathrm{d}} |B_i|^2 \, \mathrm{e}^{-(z_k^* + z_j)t_i} \, \mathrm{e}^{-\imath 2\pi \vec{\nu}_i \cdot (\vec{\mathrm{x}}_j - \vec{\mathrm{x}}_k)} \,. \tag{7.5.1}$$

e,mr,T

In the usual case where the voxel centers $\vec{\mathrm{x}}_j$ are spaced equally, this matrix would be Toeplitz[2] in the absence of relaxation effects and off-resonance effects, *i.e.*, when $z(\vec{\mathrm{x}}) = 0$. The pure Toeplitz form has been used previously to accelerate MR image reconstruction [88, 89]..

In the presence of such effects, $\boldsymbol{T}$ is not Toeplitz due to the problematic term $\mathrm{e}^{-(z_k^* + z_j)t_i}$. So we must introduce approximations to develop fast methods for computing the matrix-vector product $\boldsymbol{T}\boldsymbol{x}$ required in the gradient calculation (7.3.3). Two possible approaches are described next.

7.5.1 $O(L^2)$ approach

One approach is to separate the problematic exponential first, and then make approximations as follows:

$$\mathrm{e}^{-(z_k^* + z_j)t_i} = \mathrm{e}^{-z_k^* t_i} \, \mathrm{e}^{-z_j t_i} \approx \left[\sum_{l'=1}^{L} b_{il'} c_{l'k} \right]^* \left[\sum_{l=1}^{L} b_{il} c_{lj} \right] ,$$

i.e., to invoke an approximation of the form (7.4.3) twice. Substituting into (7.5.1) and rearranging leads to the following:

$$\boldsymbol{T} \approx \sum_{l'=1}^{L} \sum_{l=1}^{L} \boldsymbol{D}_{l'}' \boldsymbol{T}_{l'l} \boldsymbol{D}_l , \tag{7.5.2}$$

e,mr,T,approx,L2

where

$$[\boldsymbol{T}_{l'l}]_{kj} = \sum_{i=1}^{n_\mathrm{d}} |B_i|^2 \, b_{il'}^* b_{il} \, \mathrm{e}^{-\imath 2\pi \vec{\nu}_i \cdot (\vec{\mathrm{x}}_j - \vec{\mathrm{x}}_k)}$$
$$\boldsymbol{D}_l = \mathsf{diag}\{c_{lj}\} \,.$$

Each matrix $\boldsymbol{T}_{l'l}$ is Toeplitz, so we can multiply this approximation to $\boldsymbol{T}$ by a vector $\boldsymbol{x}$ using L^2 pairs of FFTs. (See §6.8 and [27].) An advantage of this approach is that one can use the $\boldsymbol{B}$ and $\boldsymbol{C}$ matrices corresponding to any exponential approximation. But a significant disadvantage is that it requires $O(L^2)$ computation.

7.5.2 $O(L)$ approach

To reduce computation, we would like to use an approximation for the problematic exponential term that will allow us to "separate" the $z_k^* + z_j$ term in (7.5.1) after making the approximation. Of the various approximation methods described in §7.4, only the time segmentation approach appears to have the desired property. (Fortunately the time segmentation approach is also sufficiently accurate, as shown in Table 7.1.) Substituting the approximation (7.4.1) into (7.5.1) yields the following approximation to the elements of $\boldsymbol{T}$:

$$\begin{aligned} T_{kj} &\approx \sum_{i=1}^{n_\mathrm{d}} |B_i|^2 \left[\sum_{l=1}^{L} b_l(t_i) \, \mathrm{e}^{-(z_k^* + z_j)\check{t}_l} \right] \mathrm{e}^{-\imath 2\pi \vec{\nu}_i \cdot (\vec{\mathrm{x}}_j - \vec{\mathrm{x}}_k)} \\ &= \sum_{l=1}^{L} \mathrm{e}^{-z_k^* \check{t}_l} \left[\sum_{i=1}^{n_\mathrm{d}} |B_i|^2 \, b_l(t_i) \, \mathrm{e}^{-\imath 2\pi \vec{\nu}_i \cdot (\vec{\mathrm{x}}_j - \vec{\mathrm{x}}_k)} \right] \mathrm{e}^{-z_j \check{t}_l} \,. \end{aligned} \tag{7.5.3}$$

e,mr,Tkj,approx

In matrix form,

$$\boldsymbol{T} \approx \sum_{l=1}^{L} \boldsymbol{D}_l' \boldsymbol{T}_l \boldsymbol{D}_l , \tag{7.5.4}$$

e,mr,T,approx

[2] Strictly speaking, if $\bar{d} = 1$, then $\boldsymbol{T}$ would be Toeplitz, whereas if $\bar{d} = 2$, then $\boldsymbol{T}$ would be block Toeplitz with Toeplitz blocks [27]. (One shudders to consider the 3D terminology.) For simplicity, we simply say "Toeplitz."

where the elements of each matrix $\boldsymbol{T}_l$ are defined by

$$[\boldsymbol{T}_l]_{kj} = \sum_{i=1}^{n_\mathrm{d}} |B_i|^2 \, b_l(t_i) \, \mathrm{e}^{-\imath 2\pi \vec{\nu}_i \cdot (\vec{\mathrm{x}}_j - \vec{\mathrm{x}}_k)} \tag{7.5.5}$$

s,mr,toep,Tl

$$\boldsymbol{D}_l = \mathsf{diag}\left\{ \mathrm{e}^{-z_j \check{t}_l} \right\}. \tag{7.5.6}$$

s,mr,toep,Dl

Each matrix $\boldsymbol{T}_l$ is Toeplitz, so one can multiply $\boldsymbol{T}_l$ by a vector efficiently using a pair of FFTs. (See §6.8 and [27].) These FFTs use the first row of $\boldsymbol{T}_l$, which we precompute. Each $\boldsymbol{D}_l$ matrix is diagonal, so multiplying with it is trivial. Thus, to compute $\boldsymbol{T}\boldsymbol{x}$ (approximately) requires L pairs of FFTs, for an operation count of $O(LN \log N)$. In contrast, the NUFFT approach that uses the gradient expression in (7.3.2) requires L pairs of NUFFTs, which is more computation due to interpolations [75]. (See §6.6.)

A subtle but key issue in using (7.5.3) is choosing the interpolators $\boldsymbol{b}(t)$. If the *rate map* z_j contains frequency offsets in the range ν_min to ν_max, then the term $\mathrm{e}^{-(z_k^* + z_j)t}$ will contain frequency offsets in the range $-(\nu_\mathrm{max} - \nu_\mathrm{min})$ to $\nu_\mathrm{max} - \nu_\mathrm{min}$. In other words, its "bandwidth" is twice as wide as the bandwidth of $\mathrm{e}^{-z_j t}$. So we have found that it can be necessary to use larger values of L for the Toeplitz approximation (7.5.3) than for the NUFFT approximation (7.4.4). Nevertheless, by avoiding DFT interpolations, the Toeplitz approach is still faster than the NUFFT approach.

Generalizing (7.4.8), we would like to choose $\boldsymbol{B}$ via the following LS criterion:

$$\boldsymbol{b}(t) = \arg\min_{\boldsymbol{b} \in \mathbb{C}^L} \sum_{j=1}^{n_\mathrm{p}} \sum_{k=1}^{n_\mathrm{p}} \left| \mathrm{e}^{-(z_k^* + z_j)t} - \sum_{l=1}^{L} b_l \, \mathrm{e}^{-(z_k^* + z_j)\check{t}_l} \right|^2.$$

For a fieldmap with a given histogram $\{h_k\}$, the histogram of $z_k^* + z_j$ is given by the auto-correlation function of h_k. So to design $\boldsymbol{b}(t)$ for the Toeplitz approach, we first find the fieldmap histogram, then compute the auto-correlation function of that histogram, and then apply the WLS criterion (7.4.10) using that auto-correlated histogram. We found that this approach provided much improved accuracy relative to using (7.4.10) with the original histogram. Furthermore, because an "auto-correlated" histogram is symmetric about zero, the resulting $\boldsymbol{B}$ matrix is real valued, which saves computation in precomputing the Toeplitz kernels in (7.5.5).

Algorithm

- Determine the relaxation map and/or the field map to form the *rate map* $z(\vec{\mathrm{x}})$.
- Compute the histogram of that *rate map*, and then the auto-correlation function of that histogram.
- Using that auto-correlated histogram, use (7.4.10) to compute the interpolators $\boldsymbol{B}$ and the coefficients $\boldsymbol{C}$ using the LS time-segmentation method of §7.4.3.4 for $l = 1 \ldots, L$.
- Precompute $\boldsymbol{b} = \boldsymbol{A}'\boldsymbol{y}$ using the combination of temporal interpolation and NUFFT methods described in [59, 75]. Because this need only be done once, rather than each iteration, it can be done with a high accuracy approximation.
- Precompute the first row of $\boldsymbol{T}_l$ for $l = 1, \ldots, L$ using (7.5.5), in preparation for using a $2\times$ over-sampled FFT to perform the operation of matrix-vector multiplication by $\boldsymbol{T}_l$ [27]. This requires L pairs of NUFFT calls.
- Using (7.5.4) to compute $\boldsymbol{T}\boldsymbol{x}$ approximately for the gradient expression (7.3.3), apply a gradient-based optimization method such as the CG algorithm to find $\hat{\boldsymbol{x}}$ iteratively.

Fig. 7.5.1 illustrates the data flow.

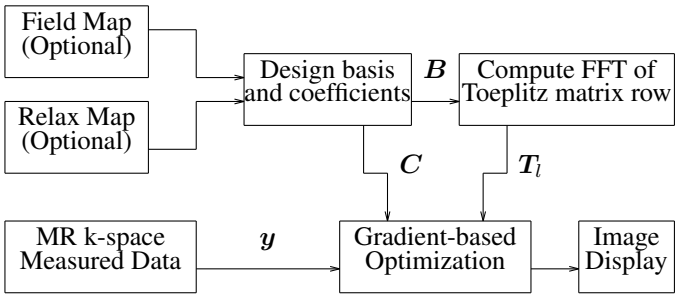

fig,mr,block

Figure 7.5.1: Block diagram of MR image reconstruction data flow.

s,mr,precon

7.5.3 Preconditioning (s,mr,precon)

When $z(\vec{\mathrm{x}}) = 0$, the matrix $\boldsymbol{T}$ in (7.5.1) is Toeplitz, and there are excellent circulant preconditioners available [27]. When $z(\vec{\mathrm{x}}) \neq 0$, then $\boldsymbol{T}$ is a approximately the "weighted sum" of Toeplitz matrices shown in (7.5.4). Finding an

effective preconditioner for this sum is an *open problem*, although preconditioners have been developed for other shift-variant problems [27, 90].

todob: clever FFT precon for CS pMRI: [91]

7.6 Simulation (s,mr,sim)

s,mr,sim

We compared four methods for field-corrected MR image reconstruction: (i) the conjugate-phase reconstruction method [76] using Voronoi-based density compensation factors [92] and the LS-optimal time-segmentation approximation described in §7.4.3.4, (ii) the CG-NUFFT method based on the gradient expression (7.3.2), using the time-segmentation approximation described in §7.4.3.4 [59], (iii) and the CG-Toeplitz method based on the gradient expression (7.3.3) using the $O(L)$ approximation described in §7.5, and (iv) for completeness, the conjugate-phase method *without* field correction. For the CG methods we used quadratic regularization with a small regularization parameter, chosen such that the FWHM of the PSF was about 1.36 pixels. For simplicity we initialized the CG algorithms with $\boldsymbol{x} = \boldsymbol{0}$.

To evaluate the methods quantitatively, we performed simulations using the brain fieldmap shown in Fig. 7.4.1, and the synthetic image shown in Fig. 7.6.1. We evaluated the reconstruction methods for two k-space trajectories: (1) conventional 64×64 Cartesian sampling with 4096 k-space points, and (2) a spiral trajectory containing 3770 points. The sampling time is 5 μs, so the data acquisition time was 20.48 ms for the Cartesian case, and 18.855 ms for the spiral case. This spiral trajectory is used routinely on our GE 3T MR system. To generate the (noiseless) simulated data $\bar{\boldsymbol{y}}$, we used the exact system matrix (7.2.6).

For all methods, we estimated only the 2936 pixels within the elliptical region of interest shown in Fig. 7.6.1. For reconstruction, we used NUFFTs with $2\times$ over-sampling and $J = 6$, which we have found previously to be sufficiently accurate.

Fig. 7.6.2 and Fig. 7.6.3 show the NRMS error, defined as $\|\hat{\boldsymbol{x}} - \boldsymbol{x}_{\mathrm{true}}\| \,/\, \|\boldsymbol{x}_{\mathrm{true}}\| \cdot 100\%$, as a function of iteration for the values of L listed. Larger values of L did not reduce the error further. Because there was no noise in the simulated k-space data, the lower limit on NRMS error is a function of the (modest) regularization used and the inherent NUFFT approximations. For these values of L (or larger) the CG algorithm converged well before 20 iterations.

Fig. 7.6.4 and Fig. 7.6.5 show the NRMS error as a function of L. For the spiral trajectory, the CG-Toeplitz approach requires L to be slightly larger than that of the CG-NUFFT approach to achieve the same accuracy.

Fig. 7.6.6 and Fig. 7.6.7 show the reconstructed images for the Cartesian and spiral trajectories, respectively. Based on the results in Fig. 7.6.4 and Fig. 7.6.5, we used $L = 6$ for the conjugate phase and CG-NUFFT approaches, and $L = 7$ or $L = 8$ for the CG-Toeplitz approach.

(We also investigated much longer readout times, *e.g.*, 25ms, and found that even larger L values were needed.)

Table 7.2 compares the CPU time of the various reconstruction methods (using MATLAB's `cputime` on a Dell 650n with 3.06GHz Xeon CPU). For the CG methods, the times are for 15 iterations, which appears adequate based on Fig. 7.6.2 and Fig. 7.6.3. The total times shown in the table include the time required to "precompute" $\boldsymbol{B}$, $\boldsymbol{C}$, etc. The Toeplitz approach shows significant acceleration. In MATLAB, for the same L the Toeplitz approach runs about several times faster per iteration than the NUFFT approach, because it avoids the NUFFT interpolations. Even though the Toeplitz approach requires a slightly larger value for L and requires precomputing the kernels of the $\boldsymbol{T}_l$ terms, overhead that partly diminishes the advantage of the Toeplitz approach, the overall compute time is still reduced significantly.

To investigate whether the approximations would increase sensitivity to noise, we added several different levels of pseudo-random white complex gaussian noise to $\bar{\boldsymbol{y}}$ and repeated the reconstructions. Table 7.2 shows that the noise properties of the CG-NUFFT and CG-Toeplitz approach are indistinguishable, because the chosen L values ensure that approximation error is negligible relative to estimation error.

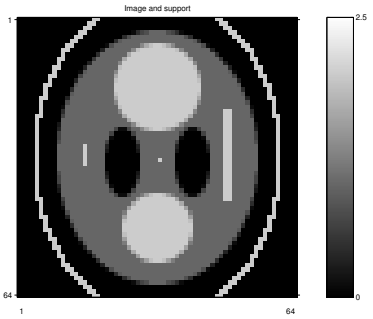

Figure 7.6.1: True image $\boldsymbol{x}$ used in simulations. Only pixels within the outer ellipse were reconstructed.

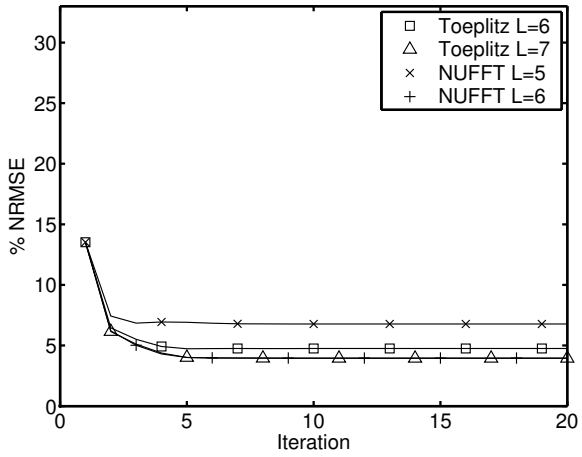

Figure 7.6.2: NRMSE of $\hat{\boldsymbol{x}}$ versus iteration for the two CG reconstruction methods for the Cartesian trajectory.

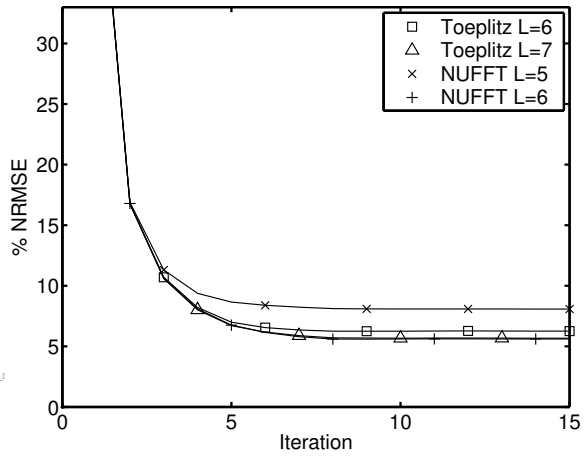

Figure 7.6.3: NRMSE of $\hat{\boldsymbol{x}}$ versus iteration for the two CG reconstruction methods for the spiral trajectory.

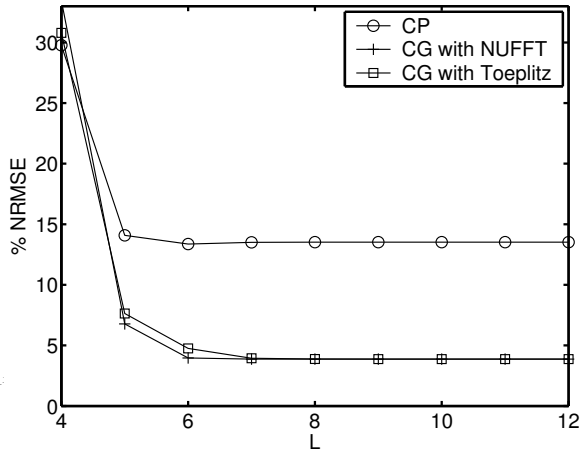

Figure 7.6.4: NRMSE of $\hat{\boldsymbol{x}}$ versus approximation order L for the three field-corrected reconstruction methods for the Cartesian trajectory.

		Precomputation						NRMS % vs SNR		
Method	L	$\boldsymbol{B}$,$\boldsymbol{C}$	$\boldsymbol{A}'\boldsymbol{D}\boldsymbol{y}$	$\boldsymbol{b} = \boldsymbol{A}'\boldsymbol{y}$	$\boldsymbol{T}_l$	15 iter	Total Time	∞	50 dB	40 dB
Conj. Phase	6	0.4	0.2				0.6	30.7	37.3	46.5
CG-NUFFT	6	0.4				5.0	5.4	5.6	16.7	26.5
CG-Toeplitz	8	0.4		0.2	0.6	1.3	2.5	5.5	16.7	26.4

Table 7.2: CPU times (seconds), including precomputation times, and NRMS error (%) for three field-corrected MR image reconstruction methods. The proposed CG-Toeplitz approach is faster than CG-NUFFT yet equally accurate. tab,mr,cpu

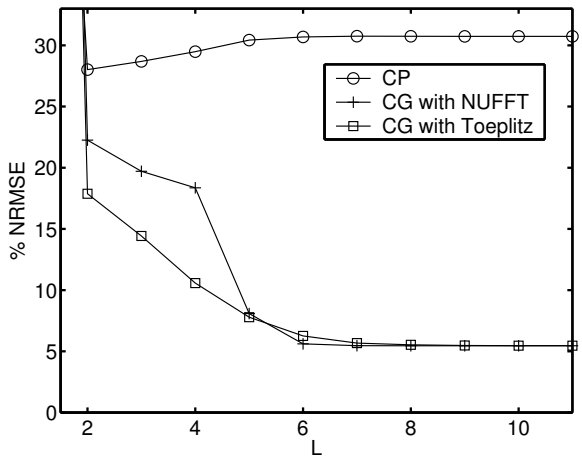

Figure 7.6.5: NRMSE of $\hat{\boldsymbol{x}}$ versus approximation order L for the three field-corrected reconstruction methods for the spiral trajectory. fig_mri_

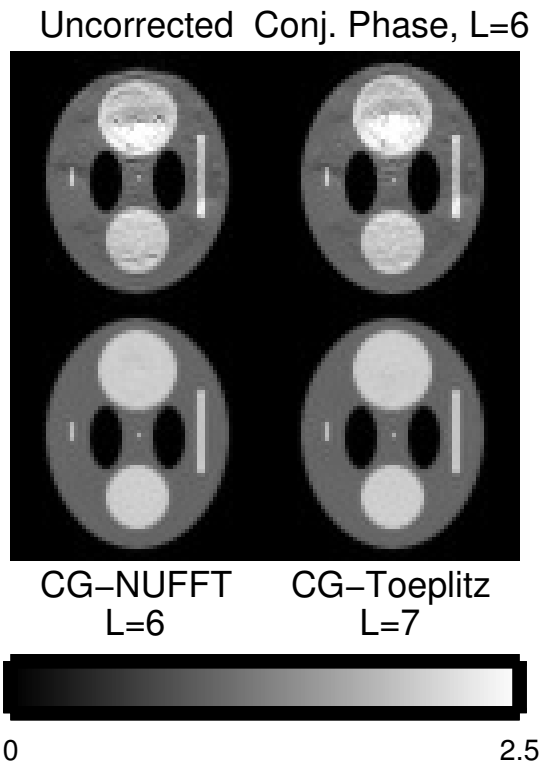

Figure 7.6.6: Reconstructed images for the Cartesian trajectory. fig_mri_race_xh_cartesian

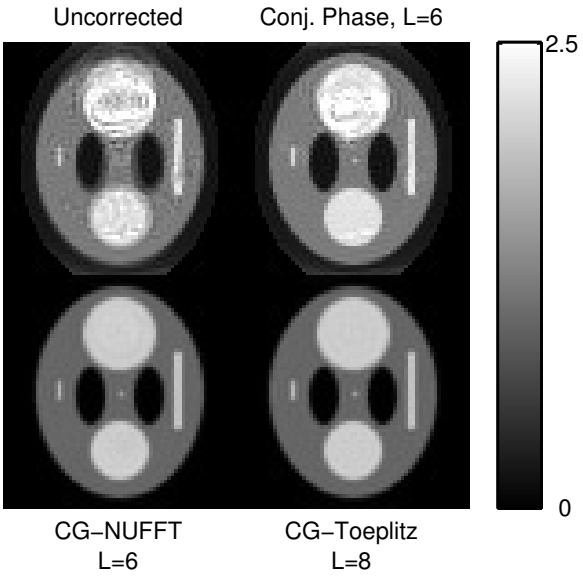

Figure 7.6.7: Reconstructed images for the spiral trajectory. fig_mri_race_xh_spiral3

7.7 Field gradients (s,mr,grad)

s,mr,grad

The assumption that the field map $\omega(\vec{\mathrm{x}})$ is constant over each voxel is inaccurate in regions with susceptibility gradients [87]. A more accurate model than (7.2.4) is to assume that $\omega(\vec{\mathrm{x}})$ is a linear function within each voxel:

$$z(\vec{\mathrm{x}}) = \sum_{j=1}^{n_\mathrm{p}} [z_j + \imath \vec{\gamma}_j \cdot (\vec{\mathrm{x}} - \vec{\mathrm{x}}_j)] \, b(\vec{\mathrm{x}} - \vec{\mathrm{x}}_j),$$

where $\vec{\gamma}_j$ denotes the gradient vector of $\omega(\vec{\mathrm{x}})$ at the center of each voxel. (These gradients can be estimated from measured field maps [87].) Under this more general model, the signal equation (7.2.1) simplifies as follows:

$$\begin{aligned}
\bar{y}_i(\boldsymbol{x}) = \mathsf{E}[y_i] &= \int \sum_{j=1}^{n_\mathrm{p}} x_j \, b(\vec{\mathrm{x}} - \vec{\mathrm{x}}_j) \, \mathrm{e}^{-[z_j + \imath \vec{\gamma}_j \cdot (\vec{\mathrm{x}} - \vec{\mathrm{x}}_j)] t_i} \, \mathrm{e}^{-\imath 2\pi \vec{\nu}_i \cdot \vec{\mathrm{x}}} \, \mathrm{d}\vec{\mathrm{x}} \\
&= \sum_{j=1}^{n_\mathrm{p}} x_j \int b(\vec{\mathrm{x}}') \, \mathrm{e}^{-\left[z_j + \imath \vec{\gamma}_j \cdot \vec{\mathrm{x}}'\right] t_i} \, \mathrm{e}^{-\imath 2\pi \vec{\nu}_i \cdot (\vec{\mathrm{x}}' + \vec{\mathrm{x}}_j)} \, \mathrm{d}\vec{\mathrm{x}}', \quad \vec{\mathrm{x}}' = \vec{\mathrm{x}} - \vec{\mathrm{x}}_j \\
&= \sum_{j=1}^{n_\mathrm{p}} x_j \left[\mathrm{e}^{-z_j t_i} \, B\left(\vec{\nu}_i + \frac{t_i}{2\pi} \vec{\gamma}_j \right) \right] \mathrm{e}^{-\imath 2\pi \vec{\nu}_i \cdot \vec{\mathrm{x}}_j} \, .
\end{aligned} \tag{7.7.1}$$

e,mr,ybi,grad

For a fast implementation, here we need to make an approximation of the form

$$\mathrm{e}^{-z_j t_i} \, B\left(\vec{\nu}_i + \frac{t_i}{2\pi} \vec{\gamma}_j \right) \approx \sum_{l=1}^{L} b_{il} c_{lj}.$$

To choose $\boldsymbol{B}$ and $\boldsymbol{C}$ here, we can histogram the z_j and $\vec{\gamma}_j$ values and apply the histogram PCA method described in §7.4.3.3.

todoa: study full SVD for this case? Man's argument that exponential basis is nearly optimal would not apply here.

todoa: because B is sinc = sin(x) / x, then perhaps we still almost have exponentials here!

todoa: idea: for estimating field map and its gradients, parameterize map, map-x-gradient, and map-y-gradient, and penalize difference between the map finite differences and the map-*-gradient.

todoa: susp gradient about 0.02 G/cm, whereas slice-selection gradient about 0.5 G/cm

We have focused in this section on local gradients in the field map $\omega(\vec{\mathrm{x}})$. Using Laplace transforms instead of Fourier transforms, one could generalize the results to consider gradients in the relaxation map $\alpha(\vec{\mathrm{x}})$, but that is unlikely to have significant effects.

todoa: [93] susceptibility gradient mapping (SGM)

7.8 Through-plane field gradients

In the recent literature on MR image reconstruction, iterative methods have been proposed for reconstructing fMRI images while compensating for the effects of **field inhomogeneity** *e.g.*, [59, 94]. However, the existing methods assume that the field inhomogeneity is constant within each voxel. In practice, the field varies across each voxel, a physically important property that is ignored by the existing methods. The through-plane field gradients are particularly important and are the focus here.

For slice-selective MR imaging a reasonable model for the received signal is

$$s(t) = \iiint h(z) \, f(x,y,z) \, \mathrm{e}^{-\imath \omega(x,y,z) t} \, \mathrm{e}^{-\imath 2\pi (k_x(t) x + k_y(t) y)} \, \mathrm{d}x \, \mathrm{d}y \, \mathrm{d}z, \tag{7.8.1}$$

e,mr,grad,s

where $h(z)$ denotes the (known) slice-selection profile, $f(x,y,z)$ denotes the (unknown) transverse magnetization, ω (x,y,z) denotes the off-resonance frequency (field map) and $(k_x(t), k_y(t))$ denotes the k-space trajectory of the scan. The goal in 2D imaging is to estimate $f(x,y,0)$ from noisy samples of the received signal $s(t)$.

In fMRI, through-plane field gradients cause spins in different planes within a voxel to become out of phase and thus lead to significant signal losses in images reconstructed by conventional methods. Iterative image reconstruction methods offer the option of modeling the effects of through-plane field gradients and thus may provide improved

image quality. If we focus on the through-plane field gradients (and ignore for simplicity the in-plane field gradients) a reasonable model for the off-resonance frequency (field map) is

$$\omega(x,y,z) = \sum_{j=1}^{n_\mathrm{p}} \mathrm{rect}_2\left(\frac{x-x_j}{\Delta}, \frac{y-y_j}{\Delta}\right)(\omega_j + 2\pi g_j z) \tag{7.8.2}$$

e,mr,grad,om

where (x_j, y_j) denotes the center of the jth voxel, ω_j denotes the off-resonance frequency at the center of the jth voxel and g_j denotes the field map through-plane gradient within the jth voxel, in units of Hz per cm. We can determine $\{\omega_j\}$ and $\{g_j\}$ using field map estimation methods and central differences [95]. For the transverse magnetization of the object we use the usual series expansion model:

$$f(x,y,z) = \sum_{j=1}^{n_\mathrm{p}} f_j \,\mathrm{rect}_2\left(\frac{x-x_j}{\Delta}, \frac{y-y_j}{\Delta}\right). \tag{7.8.3}$$

e,mr,grad,f

Substituting (7.8.2) and (7.8.3) into (7.8.1) and simplifying leads to the model

$$\begin{aligned} s(t) &= \iint \sum_{j=1}^{n_\mathrm{p}} H(tg_j)\, f_j \,\mathrm{rect}_2\left(\frac{x-x_j}{\Delta}, \frac{y-y_j}{\Delta}\right) \mathrm{e}^{-\imath\omega_j t}\, \mathrm{e}^{-\imath 2\pi(k_x(t)x + k_y(t)y)} \,\mathrm{d}x\,\mathrm{d}y \\ &= \mathrm{sinc}_2(k_x(t)\Delta, k_y(t)\Delta) \sum_{j=1}^{n_\mathrm{p}} H(tg_j)\, \mathrm{e}^{-\imath\omega_j t}\, \mathrm{e}^{-\imath 2\pi(k_x(t)x_j + k_y(t)y_j)}\, f_j, \end{aligned} \tag{7.8.4}$$

e,mr,grad,s,disc

where H denotes the Fourier transform of h. In the absence of through-plane field gradients, *i.e.*, if $g_j = 0$, then the above model is equivalent to the approach described in [59, 94] and is thus amenable to the fast iterative algorithms described therein. However, the presence of the term $H(tg_j)$ prohibits use of those previous methods.

To address this problem, we consider a 2nd-order Taylor expansion of H around the point $g_j = 0$:

$$H(\nu) \approx H(0) + \frac{1}{2}\ddot{H}(0)\,\nu^2 = 1 + \frac{1}{2}\ddot{H}(0)\,\nu^2, \tag{7.8.5}$$

e,mr,grad,H

where we assume that $\dot{H}(0) = 0$ because the slice profile $h(z)$ is symmetric, and furthermore that the slice profile is normalized such that $H(0) = 1$. For example, for a gaussian slice profile with $h(z) = (1/\triangle_\mathrm{z})\,\mathrm{e}^{-\pi(z/\triangle_\mathrm{z})^2}$, we have $H(\nu) = \mathrm{e}^{-\pi(\triangle_\mathrm{z}\nu)^2}$ so $\ddot{H}(0) = -2\pi\triangle_\mathrm{z}^2$. As another example, if $h(z) = (1/\triangle_\mathrm{z})\,\mathrm{rect}(z/\triangle_\mathrm{z})$ then $H(\nu) = \mathrm{sinc}(\triangle_\mathrm{z}\nu)$ so $\ddot{H}(0) = -\triangle_\mathrm{z}^2\,\pi^2/3$. Physically, these negative signs correspond to the signal loss associated with through-plane gradients.

Substituting (7.8.5) into (7.8.4) leads to the approximate signal model

$$s(t) \approx \mathrm{sinc}_2(k_x(t)\Delta, k_y(t)\Delta) \sum_{j=1}^{n_\mathrm{p}} \mathrm{e}^{-\imath\omega_j t}\, \mathrm{e}^{-\imath 2\pi(k_x(t)x_j + k_y(t)y_j)}\, f_j \tag{7.8.6}$$

$$+ \frac{1}{2}\ddot{H}(0)\,t^2\,\mathrm{sinc}_2(k_x(t)\Delta, k_y(t)\Delta) \sum_{j=1}^{n_\mathrm{p}} \mathrm{e}^{-\imath\omega_j t}\, \mathrm{e}^{-\imath 2\pi(k_x(t)x_j + k_y(t)y_j)}\, (g_j^2 f_j). \tag{7.8.7}$$

e,mr,grad,s,approx

This model is now amenable to the types of fast algorithms described in [59, 94]. Essentially, to compute the signal samples $s(t_i)$ using the above model requires *two* time-segmented NUFFT calls [59], one applied to $\{f_j\}$ itself, and the other applied to $\left\{g_j^2 f_j\right\}$, along with some other simple multiplication operations.

To increase accuracy, one could use a 4th-order Taylor series, which would then require three time-segmented NUFFT calls for each signal evaluation (or adjoint thereof). Alternatively, one could apply generalizations any of the approximations described in §7.4 [94], *i.e.*, find b_{il} and c_{lj} values for which

$$H(t_i g_j)\,\mathrm{e}^{-\imath\omega_j t_i} \approx \sum_{l=1}^{L} b_{il} c_{lj},$$

which leads to the signal approximation

$$s(t_i) \approx \sum_{l=1}^{L} b_{il}\,\mathrm{sinc}_2(k_x(t_i)\Delta, k_y(t_i)\Delta) \left[\sum_{j=1}^{n_\mathrm{p}} \mathrm{e}^{-\imath 2\pi(k_x(t_i)x_j + k_y(t_i)y_j)}\, (c_{lj} f_j)\right].$$

This can be implemented using L NUFFT calls. An intriguing option is the histogram PCA approach of §7.4.3.3.

s,mr,fieldmap

7.9 Fieldmap estimation (s,mr,fieldmap)

For field-corrected MR image reconstruction, one must have available an estimate of the fieldmap $\boldsymbol{\omega} = (\omega_1, \dots, \omega_{n_\mathrm{p}})$. A common approach to measuring fieldmaps is to acquire two scans of the object with slightly different echo times, and then to reconstruct images $\boldsymbol{y}$ and $\boldsymbol{z}$ (without field correction) from those two scans. The usual model for those reconstructed images is

e,mr,fieldmap,yz

$$\begin{aligned} y_j &= f_j + \varepsilon_j \\ z_j &= f_j \, \mathrm{e}^{\imath \omega_j \triangle_\mathrm{T}} + \eta_j, \end{aligned} \tag{7.9.1}$$

where $\triangle_\mathrm{T}$ denotes the echo-time difference, f_j denotes the underlying complex transverse magnetization in the jth voxel, and ε_j and η_j denote (complex) noise. The goal is to estimate $\boldsymbol{\omega}$ from $\boldsymbol{y}$ and $\boldsymbol{z}$, whereas $\boldsymbol{f} = (f_1, \dots, f_{n_\mathrm{p}})$ is a nuisance parameter vector. For simplicity, we define the unknown phase to be $x_j = \omega_j \triangle_\mathrm{T}$, so that the goal is to estimate $\boldsymbol{x}$ from $\boldsymbol{y}$ and $\boldsymbol{z}$. The next section reviews the standard approach for this problem. Subsequent sections describe three new and improved methods.

7.9.1 Conventional phase / fieldmap estimator

The usual estimator $\hat{x}_j$ uses the phase difference of the two images, computed as follows:

e,mr,fieldmap,usual

$$\hat{x}_j = \angle(y_j^* z_j) = \angle z_j - \angle y_j, \tag{7.9.2}$$

and the fieldmap estimate is simply a scaled version: $\hat{\omega}_j = \hat{x}_j / \triangle_\mathrm{T}$. This expression would work perfectly in the absence of noise and phase wrapping, within any voxels where $|f_j| > 0$. However, (7.9.2) can be very sensitive to noise, particularly in voxels where the image magnitude $|f_j|$ is small relative to the noise deviations. Furthermore, that estimate ignores our *a priori* knowledge that fieldmaps tend to be smooth or piecewise smooth. Although one could try to smooth the above estimate using a lowpass filter, usually many of the $\hat{x}_j$ values are severely corrupted so smoothing will further propagate such errors. Instead, we propose below to integrate the smoothing into the estimation of $\boldsymbol{x}$ in the first place, rather than trying to "fix" the noise in $\hat{\boldsymbol{x}}$ by post processing.

s,mr,fieldmap,ml

7.9.2 Maximum-likelihood phase / fieldmap estimation

The conventional estimate (7.9.2) appears to disregard noise effects, so a natural approach is to estimate $\boldsymbol{x}$ using a maximum likelihood (ML) method based on a statistical model for the measurements $\boldsymbol{y}$ and $\boldsymbol{z}$. In MR, the k-space measurements have zero-mean white gaussian complex noise, and we furthermore assume that the additive noise values in $\boldsymbol{y}$ and $\boldsymbol{z}$ in (7.9.1) are independent and have the same variance σ^2. Under these assumptions, the joint log-likelihood for $\boldsymbol{f}$ and $\boldsymbol{x}$ given $\boldsymbol{y}$ and $\boldsymbol{z}$ is

$$\log \mathsf{p}(\boldsymbol{y}; \boldsymbol{f}) + \log \mathsf{p}(\boldsymbol{z}; \boldsymbol{f}, \boldsymbol{x}) \equiv \frac{-1}{2\sigma^2} \sum_{j=1}^{n_\mathrm{p}} |y_j - f_j|^2 + |z_j - f_j \, \mathrm{e}^{\imath x_j}|^2 \,,$$

where "$\equiv$" denotes equality to within constants independent of $\boldsymbol{x}$. Thus, simultaneous ML estimation of $\boldsymbol{f}$ and $\boldsymbol{x}$ is achieved by the following minimization problem:

$$\min_{\boldsymbol{x} \in \mathbb{R}^{n_\mathrm{p}}} \min_{\boldsymbol{f} \in \mathbb{C}^{n_\mathrm{p}}} \sum_{j=1}^{n_\mathrm{p}} \left\| \begin{bmatrix} y_j \\ z_j \end{bmatrix} - \begin{bmatrix} 1 \\ \mathrm{e}^{\imath x_j} \end{bmatrix} f_j \right\|^2 .$$

This problem is quadratic in f_j, leading to the following ML estimate:

$$\hat{f}_j = \frac{y_j + \mathrm{e}^{-\imath x_j} z_j}{2}.$$

Substituting this estimate back into the cost function and simplifying yields the following minimization problem for ML estimation of $\boldsymbol{x}$:

e,mr,fieldmap,ml,kost

$$\min_{\boldsymbol{x}} \Psi(\boldsymbol{x}), \quad \Psi(\boldsymbol{x}) = \sum_{j=1}^{n_\mathrm{p}} \frac{1}{2} \left| y_j - \mathrm{e}^{-\imath x_j} z_j \right|^2 . \tag{7.9.3}$$

Now note that

$$\frac{1}{2}\left|y_j - \mathrm{e}^{-\imath x_j}\, z_j\right|^2 \equiv -\frac{1}{2}\left(y_j\, \mathrm{e}^{\imath x_j}\, z_j^* + y_j^*\, \mathrm{e}^{-\imath x_j}\, z_j\right) = -\operatorname{real}\left\{y_j^*\, \mathrm{e}^{-\imath x_j}\, z_j\right\} = -\left|y_j z_j\right| \cos(\angle z_j - \angle y_j - x_j)\,.$$

Thus the cost function is equivalent to

$$\Psi(\boldsymbol{x}) \equiv \sum_{j=1}^{n_\mathrm{p}} \left|y_j z_j\right| \left[1 - \cos(\angle z_j - \angle y_j - x_j)\right]. \tag{7.9.4}$$

e,mr,fieldmap,Kx,ML

The ML estimate is not unique here due to the possibility of phase wrapping. But ignoring that issue, because $1-\cos(t)$ has a minimum at zero, the ML estimate of $\boldsymbol{x}$ is $\hat{x}_j = \angle z_j - \angle y_j$, which is simply the usual estimate (7.9.2) once again. Thus the usual method is in fact an ML estimator under the white gaussian noise model!

7.9.3 Penalized likelihood phase / fieldmap estimation

The ML estimator ignores our *a priori* knowledge that fieldmaps tend to be spatially smooth functions due to the physical nature of main field inhomogeneity and susceptibility effects. A natural approach to incorporating this characteristic is to add a regularizing roughness penalty to the cost function. (A similar approach was applied for estimating spin density, T_1, and T_2 maps in [114].) Here we regularize only the phase map $\boldsymbol{x}$ and not the magnetization map $\boldsymbol{f}$; we expect $\boldsymbol{f}$ to be far less smooth because it contains anatomical details. Such regularization is equivalent to replacing ML estimation with a certain Bayesian MAP estimator. In either case, the resulting regularized cost function has the form

$$\Psi(\boldsymbol{x}) = \sum_{j=1}^{n_\mathrm{p}} \left|y_j z_j\right| \left[1 - \cos(\angle z_j - \angle y_j - x_j)\right] + \beta\, \mathsf{R}(\boldsymbol{x}), \tag{7.9.5}$$

e,mr,fieldmap,Kx,PL

where $\mathsf{R}(\boldsymbol{x})$ is a spatial roughness penalty. This cost function automatically gives low weight to any voxels where the magnitude $|y_j z_j|$ is small. (Similar weighting appeared in the weighted phase estimate proposed in [115] for angiography.) For such voxels, the regularization term will have the effect of smoothing or extrapolating the neighboring values. Thus, this approach avoids the phase "outlier" problem that plagues the usual estimate (7.9.2) in voxels with low signal magnitude.

If $\boldsymbol{x}$ corresponds to a $M \times N$ fieldmap $x[m,n]$, then a typical regularizing roughness penalty uses the differences between horizontal and vertical neighboring voxel values as follows:

$$\mathsf{R}(\boldsymbol{x}) = \sum_{m=1}^{M-1} \sum_{n=0}^{N-1} \psi(x[m,n] - x[m-1,n]) + \sum_{m=0}^{M-1} \sum_{n=1}^{N-1} \psi(x[m,n] - x[m,n-1])\,. \tag{7.9.6}$$

e,mr,fieldmap,R,1st

Usually ψ is differentiable, so we can minimize the cost function $\Psi(\boldsymbol{x})$ either by conventional gradient descent methods or by optimization transfer methods as described in §20.18. In particular, in the usual case where $\dot{\psi}(t)\,/t$ is bounded by unity, then the following iteration is guaranteed to decrease $\Psi(\boldsymbol{x})$ monotonically:

$$\boldsymbol{x}^{(n+1)} = \boldsymbol{x}^{(n)} - \mathsf{diag}\left\{\frac{1}{|y_j z_j| + \beta \cdot 4}\right\} \nabla \Psi(\boldsymbol{x}^{(n)}), \tag{7.9.7}$$

e,mr,fieldmap,xnn

because the second derivative of $1-\cos t$ is bounded above by unity. This algorithm will converge to a local minimizer of $\Psi(\boldsymbol{x})$ within the "basin" that contains the initial estimate [116]. We use the ML estimate to initialize $\boldsymbol{x}^{(0)}$.

7.9.4 Phase-based estimator

An alternative approach is to discard the magnitude of z_j and y_j and use only the phases $\angle z_j$ and $\angle y_j$. The distribution of these phases is given in [117], along with a convenient approximation. The drawback of using only the phase information is that it disregards the fact that the magnitude f_j is the same (in the absence of motion etc.) between z_j and y_j, and this constraint adds information. Quantifying the benefit of this constraint is an *open problem.*

7.9.5 PWLS fieldmap estimator

Usually the time delay $\triangle_\mathrm{T}$ is chosen to ensure that there will be little if any phase wrapping. In such cases, we can simplify computation by approximating the $1 - \cos$ term in (7.9.5) with its second-order Taylor series: $1 - \cos(t) \approx$

$t^2/2$. Substituting this approximation into (7.9.5) leads to the following penalized weighted least squares (PWLS) cost function for estimating $\boldsymbol{x}$:

$$\hat{\boldsymbol{x}} = \arg\min_{\boldsymbol{x}} \Psi(\boldsymbol{x}), \qquad \Psi(\boldsymbol{x}) = \sum_{j=1}^{n_\mathrm{p}} w_j \frac{1}{2} \left(\angle z_j - \angle y_j - x_j \right)^2 + \beta \, \mathsf{R}(\boldsymbol{x}), \tag{7.9.8}$$

e,mr,fieldmap,pwls

where we define a magnitude-dependent weighting function as follows:

$$w_j \triangleq |y_j z_j| \,. \tag{7.9.9}$$

e,mr,fieldmap,wj

Similar PWLS estimators have been applied in a variety of applications, including PET image reconstruction [118] and in **gradient vector flow** [119] for contour estimation. Such estimators give more weight to the "good data" and less weight to the noisy data, and use regularization to control noise. Weighting has been used previously for field map fitting, *e.g.*, [80].

In the current image processing literature, edge-preserving potential functions ψ are quite popular. However, because fieldmaps are spatially smooth and often free of "edges," typically we use the quadratic function $\psi(t) = t^2/2$. Because in this case the cost function (7.9.8) is quadratic, it is minimized easily by the conjugate-gradient (CG) algorithm. We denote the resulting method as QPWLS-CG. If one encounters fieldmaps that have steep gradients, then it may be preferable to use an edge-preserving potential function ψ. In such cases one can use a CG algorithm with a modified line search [90] to minimize Ψ efficiently. However, the model (7.9.1) may be unrealistic if the field gradients are so steep that there is substantial within-voxel variation. For such cases it may be necessary to consider other formulations such as the k-space approach described in §7.9.8.

To further simplify processing, one could binarize the weights w_j using a threshold:

$$w_j \triangleq \begin{cases} 1, & |y_j z_j| > \gamma \\ 0, & \text{otherwise}, \end{cases} \tag{7.9.10}$$

e,mr,fieldmap,wj,binary

where we set the threshold γ to include only voxels with "sufficiently large" magnitude, *e.g.*, $\gamma = 0.4 \max_j |y_j z_j|$. This approach was used routinely in our group prior to the development of the ML-based weighting in (7.9.8).

The primary limitation on of the cost function (7.9.8) is that it ignores any **phase wrap** that may occur when evaluating (7.9.2). If such phase wrap is possible, then it may be preferable to use the penalized likelihood estimator (7.9.5).

MIRT *See* `mri_phase_denoise.m`.

7.9.6 Results

Fig. 7.9.1 shows an example of the data magnitude $|y_j|$ and the usual phase estimate (7.9.2) which is very noisy. It also shows the penalized likelihood estimate based on (7.9.7), the QPWLS estimate from (7.9.8), and the QPWLS estimate using (7.9.10). The normalized RMS difference between the penalized likelihood method and the QPWLS approximation (7.9.8) was 3.1%, whereas the QPWLS results based on the binary weights (7.9.10) differed by over 40% normalized RMS.

For a quantitative evaluation, Fig. 7.9.2 shows a simulation case. We used the fieldmap shown in Fig. 7.9.2 as the true fieldmap. We multiplied the magnitude image shown in Fig. 7.9.2 by $\mathrm{e}^{\imath \omega_j \triangle_\mathrm{T}}$ and added complex white gaussian noise, yielding an SNR of 16.4 dB. Fig. 7.9.3 shows a second simulation, using a synthetic fieldmap, where the SNR was 10.1 dB. The accuracy of the estimated fieldmaps is summarized in the following table.

	Simulation 1		Simulation 2	
Method	RMS Error [Hz]	Max Error [Hz]	RMS Error [Hz]	Max Error [Hz]
Conventional	23.3	270	16.0	198
Penalized-likelihood	2.7	19	5.9	63
QPWLS (ML w_i)	2.7	20	5.8	64
QPWLS (simple w_i)	14.3	119	8.6	110

In all of these results, and others not shown, the PL method and the QPWLS method using (7.9.9) performed the best. Compared to penalized-likelihood, the QPWLS cost function is somewhat easier to minimize, so QPWLS with the approximation (7.9.8) is a practical and accurate approach in the usual cases where phase wrapping is not expected.

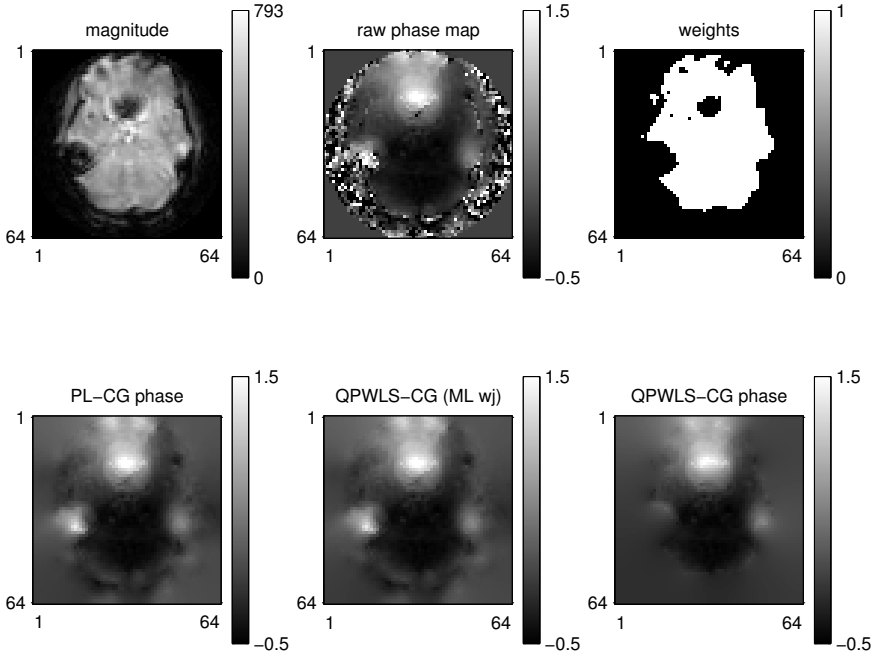

Figure 7.9.1: Top row: magnitude image $|y_j|$, usual phase estimate (7.9.2), and binary weights w_j in (7.9.10). Bottom row (phase estimates): penalized likelihood using (7.9.7), QPWLS using (7.9.8), and QPWLS using (7.9.10). fig_mr_phase_pl

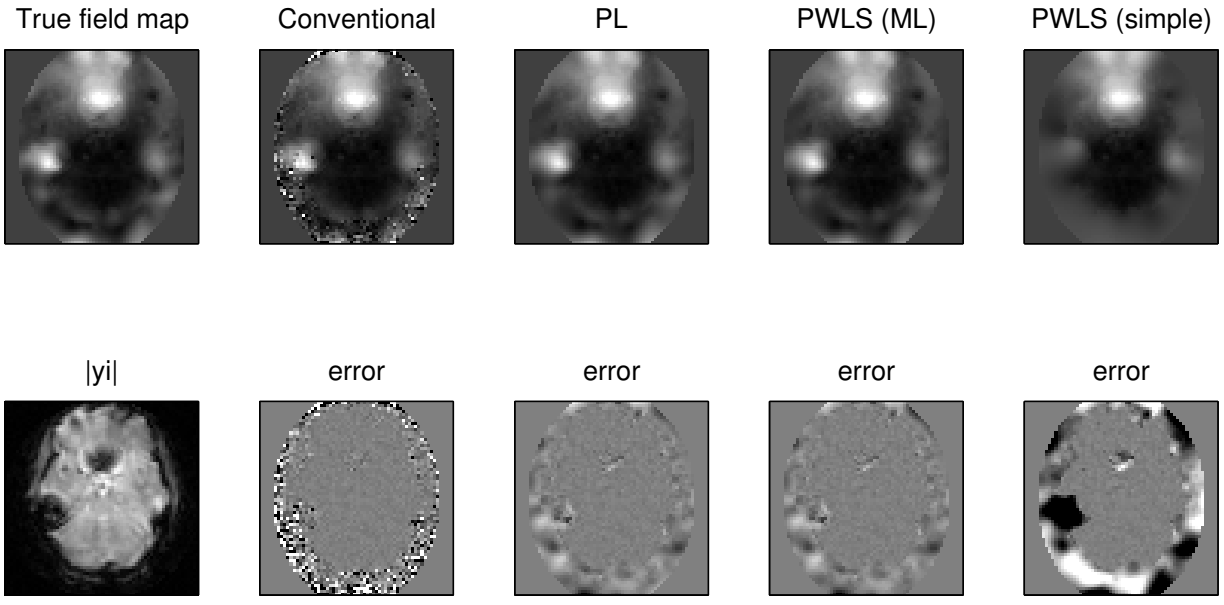

Figure 7.9.2: Images used for fieldmap smoothing simulation. Top row: true field map $x_j/\triangle_{\mathrm{T}}$, usual estimate (7.9.2), penalized likelihood using (7.9.7), QPWLS using (7.9.8), and QPWLS using (7.9.10). Display range from -40 to 120 Hz. Bottom row magnitude image $|y_j|$, and error of each estimate, displayed over the range -20 to 20 Hz. fig_mr1_phase_denoise_sim1

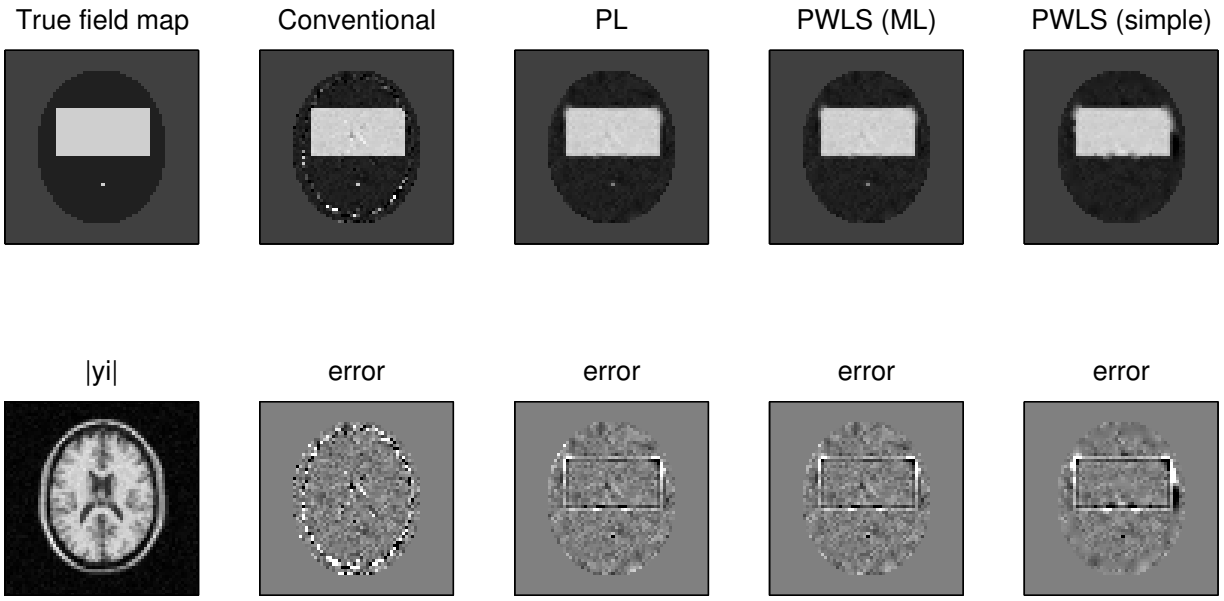

fig_mri_phase_denoise_sim2

Figure 7.9.3: Simulation results using a synthetic fieldmap. (Display is same as Fig. 7.9.2.)

7.9.7 Spatial resolution analysis of fieldmap estimation

One drawback of the regularized methods (7.9.5) and (7.9.8) above is that the user must select the regularization parameter β, which could seem tedious if one uses trial-and-error methods. Fortunately, it is particularly simple to analyze the spatial resolution properties for this problem, using the methods in [120] for example. (See Chapter 22.) The local frequency response of the QPWLS estimator (7.9.8) at the jth voxel can be shown to be

e,mr,fieldmap,Hoo

$$H(\Omega_1, \Omega_2) \approx \frac{1}{1 + \beta / w_j (\Omega_1^2 + \Omega_2^2)^p}, \tag{7.9.11}$$

where $p = 1$ for regularization based on first-order differences as in (7.9.6), and $p = 2$ for 2nd-order finite differences. (See [121] for related analysis.) Using this form, one can use the inverse 2D DSFT to compute the PSF $h[m, n]$ and tabulate its FWHM as a function of β / w_j. Fig. 7.9.4 shows this FWHM as a function of $\log_2(\beta / w_j)$, for both $p = 1$ and $p = 2$. The FWHM increases monotonically with β, as expected, although the "knees" in the curve are curious. Nevertheless, one can use this graph to select the appropriate β given the desired spatial resolution in the estimated fieldmap. To simplify such selection, we normalize the weights in (7.9.9) by the median of the nonzero values so that the "typical" w_j value is unity. The resulting spatial resolution will be inherently nonuniform, with more smoothing in the regions with low magnitudes w_j and vice versa. One could explore modified regularization methods [120] to make the resolution uniform, but in this application nonuniform resolution seems appropriate because the goals include "interpolating" across signal voids.

Fig. 7.9.5 shows that the *shape* of the PSF depends strongly on whether one uses regularization based on 1st-order or 2nd-order finite differences. These profiles suggest that 2nd-order differences are preferable because the PSF tails decrease more rapidly even though the FWHM values are identical.

MIRT *See* `qpwls_psf.m`.

s,mr,fieldmap,kspace

7.9.8 Fieldmap estimation in k-space

The methods described above estimate the fieldmap from two *reconstructed* images. To work well, those images should be relatively free of artifacts, blur, and distortions, necessitating appropriate data acquisition types. For pulse sequences with long readout times, it may be more appropriate to estimate the fieldmap directly from the raw k-space data. A typical scenario is that we can collect two sets of k-space data, with slightly different echo times. A reasonable model for the data is:

$$\mathsf{E}\left[y_i^{(l)}\right] = \int f(\vec{x}) \, \mathrm{e}^{-\imath \, \omega(\vec{x})(t_i + l \triangle_\mathrm{T})} \, \mathrm{e}^{-\imath 2\pi \vec{\nu}_i \cdot \vec{x}} \, \mathrm{d}\vec{x}, \qquad l = 0, 1.$$

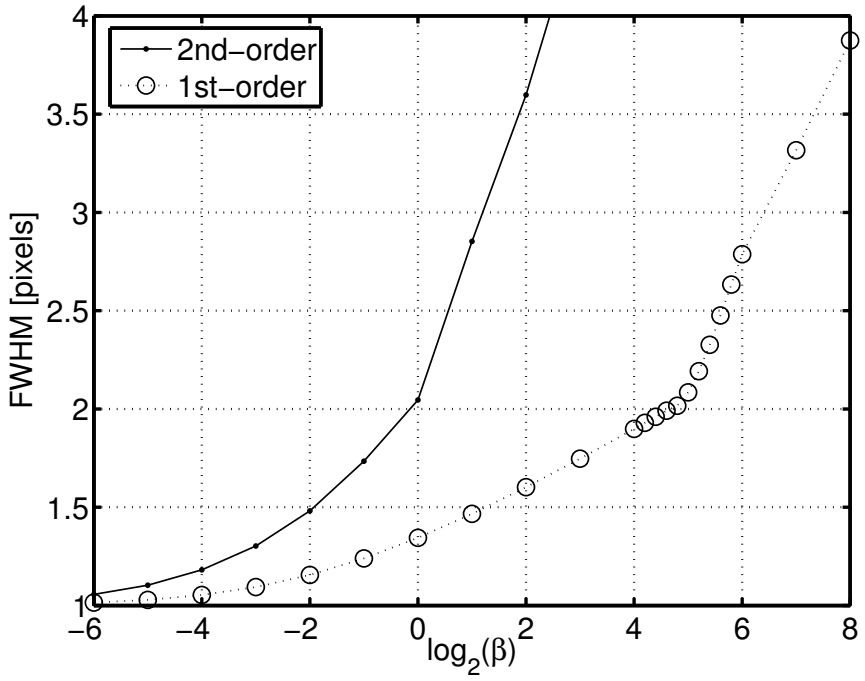

fig_mr_fieldmap_psf

Figure 7.9.4: Angularly averaged FWHM of PSF for fieldmap estimation as a function of $\log_2 \beta$ for $w_j = 1$.

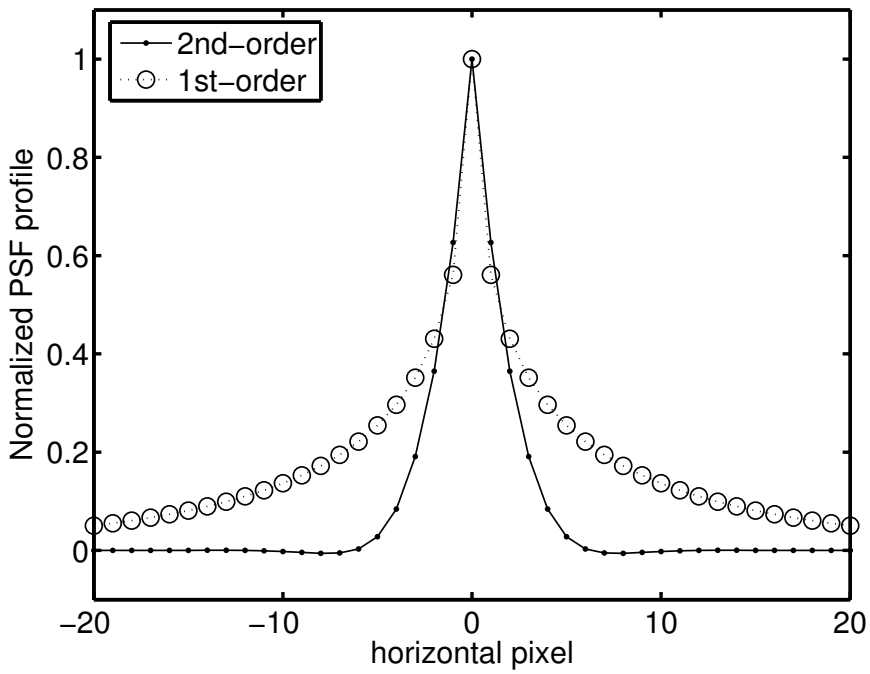

Figure 7.9.5: Profiles through reconstructed PSF corresponding to (7.9.11) for regularization based on 1st-order or 2nd-order finite differences. The regularization parameter β was chosen in both cases so that the FWHM was 3 pixels.

fig_mr_fieldmap_psf_profile

We want to estimate $f(\vec{x})$ and $\omega(\vec{x})$ from $\boldsymbol{y}^{(0)}$ and $\boldsymbol{y}^{(1)}$. This is a joint estimation problem like that described in [62]. One can define a cost function in terms of $\boldsymbol{f}$ and $\boldsymbol{\omega}$, and then alternate between holding $\boldsymbol{\omega}$ fixed and minimizing over $\boldsymbol{f}$ (using the conjugate gradient methods) and then holding $\boldsymbol{f}$ fixed and minimizing over $\boldsymbol{\omega}$ (using steepest descent [62] or linearization [69] or optimization transfer methods akin to [122]). These k-space methods require considerably more computation than the image domain methods, so one should first apply an image-domain method to get a reasonable initial estimate of the fieldmap $\boldsymbol{\omega}$. It might be particularly easy to implement such methods using modified EPI trajectories [123].

todob: elaborate on approach in [122] *i.e.*, separate regularization of magnitude and phase. In particular, as suggested by Gary Glover (at ISBI 2004?), could start by deriving a majorizer for both magnitude and phase jointly See also [124–126].

It would be of interest to generalize the approach to phased array coils *cf.*, [127].

todoa: using multiple echos [47, 128, 129].

s,mr,relaxmap

7.10 Relaxation map estimation (s,mr,relaxmap)

In some MR applications, it is useful to estimate tissue relaxation parameters, particularly T_2, on a pixel-by-pixel basis, *e.g.*, [130–132]. One approach to measuring such relaxation parameters is to acquire a "baseline" scan of the object and then acquire $L \geq 1$ additional scans having different echo times. One then reconstructs images $\boldsymbol{y}$ and $\boldsymbol{z}_1, \ldots, \boldsymbol{z}_L$ from those scans. The usual model for those reconstructed images is

$$\begin{aligned} y_j &= f_j + \varepsilon_j \\ z_{lj} &= f_j \, \mathrm{e}^{-\tau_l x_j} + \eta_j, \end{aligned} \tag{7.10.1}$$

e,mr,relaxmap,yz

where τ_l denotes the echo-time difference of the lth scan relative to the baseline scan, f_j denotes the underlying complex transverse magnetization in the jth voxel for the baseline scan, and ε_j and η_j denote (complex) noise. The goal is to estimate the relaxation parameters $\boldsymbol{x} = (x_1, \ldots, x_{n_\mathrm{p}})$ and the magnetization values $\boldsymbol{f} = (f_1, \ldots, f_{n_\mathrm{p}})$ from the images $\boldsymbol{y}$ and $\{\boldsymbol{z}_l\}$. The most challenging aspect of this problem is that the signal model (7.10.1) depends nonlinearly on the relaxation parameters $\boldsymbol{x}$. The next section reviews the standard approach for this problem. Subsequent sections describe new methods.

7.10.1 Conventional relaxation map estimator

The usual estimator $\hat{x}_j$ uses a pixel-wise LS fit to the log of the image magnitudes, as follows:

$$\underset{\beta_0, x_j}{\arg\min} \left\| \begin{bmatrix} \log|y_j| \\ \log|z_{1j}| \\ \vdots \\ \log|z_{Lj}| \end{bmatrix} - \begin{bmatrix} 1 & 0 \\ 1 & -\tau_1 \\ \vdots & \vdots \\ 1 & -\tau_L \end{bmatrix} \begin{bmatrix} \beta_0 \\ x_j \end{bmatrix} \right\|.$$

The solution is:

$$\hat{x}_j = \frac{\tau_s \log|y_j| + \sum_{l=1}^{L} (\tau_s - (L+1)\tau_l) \log|z_{lj}|}{(L+1) \sum_{l=1}^{L} \tau_l^2 - \tau_s^2}, \tag{7.10.2}$$

e,mr,relaxmap,usual

where $\tau_s \triangleq \sum_{l=1}^{L} \tau_l$. In particular, when $L = 1$ this simplifies to

$$\hat{x}_j = \frac{\log|y_j| - \log|z_{1j}|}{\tau_1}. \tag{7.10.3}$$

e,mr,relaxmap,xhj,L=2

These expressions would work perfectly in the absence of noise, within any voxels where $|f_j| > 0$. However, (7.10.2) can be very sensitive to noise, particularly in voxels where the image magnitude $|f_j|$ is small relative to the noise deviations. One could apply post-processing to try to filter out the noise, *e.g.*, [133], but it would be preferable to reduce the errors at the outset.

s,mr,relaxmap,ml

7.10.2 Maximum-likelihood relaxation map estimation

Because the conventional estimate (7.10.2) appears to disregard noise effects, a natural approach is to estimate $\boldsymbol{x}$ using a maximum likelihood (ML) method based on a statistical model for the measurements $\boldsymbol{y}$ and $\boldsymbol{z} = \boldsymbol{z}_1, \ldots, \boldsymbol{z}_L$. In MR, the measurements have white gaussian complex noise, and we assume that the additive noise values in $\boldsymbol{y}$ and $\boldsymbol{z}$ in (7.10.1) are independent and have the same variance σ^2. Under these assumptions, the log-likelihood for $\boldsymbol{f}$ and $\boldsymbol{x}$ given $\boldsymbol{y}$ and $\boldsymbol{z}$ is

$$\log \mathsf{p}(\boldsymbol{y}; \boldsymbol{f}) + \log \mathsf{p}(\boldsymbol{z}; \boldsymbol{f}, \boldsymbol{x}) \equiv \frac{-1}{2\sigma^2} \sum_{j=1}^{n_\mathrm{p}} \left[|y_j - f_j|^2 + \sum_{l=1}^{L} \left| z_{lj} - f_j \, \mathrm{e}^{-\tau_l x_j} \right|^2 \right],$$

where "$\equiv$" denotes equality to within constants independent of $\boldsymbol{x}$. We would like to jointly minimize over $\boldsymbol{f}$ and $\boldsymbol{x}$ for simultaneous ML estimation For the case $L = 1$, one can show (with tedious algebra) that (7.10.3) is in fact the ML estimate of x_j. For $L > 1$, there is no apparent simple expression for the ML estimate, but presumably it is still sensitive to noise for voxels where $|f_j|$ is small, because when $|f_j|$ is small, the measurements z_{lj} in (7.10.1) depend only weakly on x_j.

7.10.3 Penalized-likelihood relaxation map estimation

To control noise, we introduce regularization, albeit cautiously because relaxation maps are likely to be much less smooth than fieldmaps and sensitivity maps, because relaxation is a tissue characteristic. We propose the following regularized cost function:

$$\sum_{j=1}^{n_\mathrm{p}} \left[|y_j - f_j|^2 + \sum_{l=1}^{L} \left| z_{lj} - f_j \, \mathrm{e}^{-\tau_l x_j} \right|^2 \right] + \beta \, \mathsf{R}(\boldsymbol{x}) + \mathsf{R}_0(\boldsymbol{f}), \tag{7.10.4}$$

e,mr,relaxmap,Kx,PL

where $\mathsf{R}(\boldsymbol{x})$ and $\mathsf{R}_0(\boldsymbol{f})$ are spatial roughness penalties. We will use edge-preserving regularization.

To minimize this cost function, we initialize $\hat{\boldsymbol{x}}$ using the usual estimator (7.10.2). We then alternate between updating $\hat{\boldsymbol{f}}$ and then updating $\hat{\boldsymbol{x}}$. The data-fit term above is quadratic in $\boldsymbol{f}$, so the CG algorithm is well suited to updating $\hat{\boldsymbol{f}}$. For updating $\hat{\boldsymbol{x}}$, one option is to use CG after linearizing around the previous estimate of $\boldsymbol{x}$. Alternatively, we can apply optimization transfer methods. We rewrite the second term above as

$$\sum_{j=1}^{n_\mathrm{p}} \sum_{l=1}^{L} \bar{\mathsf{h}}_i(x_j; z_{lj}, f_j, \tau_l),$$

where we define the marginal negative log-likelihood by

$$\bar{\mathsf{h}}_i(x; z, f, t) = \frac{1}{2} \left| z - f \, \mathrm{e}^{-tx} \right|^2 \equiv \frac{1}{2} |f|^2 \, \mathrm{e}^{-2tx} - \mathrm{real}\{z^* f\} \, \mathrm{e}^{-tx} \, .$$

The second derivative of this function is

$$\frac{\partial^2}{\partial x^2} \ddot{\mathsf{h}}_i(x; z, f, t) = 2t^2 |f|^2 \, \mathrm{e}^{-2tx} - t^2 \, \mathrm{real}\{z^* f\} \, \mathrm{e}^{-tx} = t^2 \, \mathrm{e}^{-tx} \left(2 |f|^2 \, \mathrm{e}^{-tx} - \mathrm{real}\{z^* f\} \right),$$

which, for $x \geq 0$, is bounded above by

$$\breve{c}_i = 2t^2 |f|^2 + t^2 \left[- \mathrm{real}\{z^* f\} \right]_+ .$$

Thus we can use a separable quadratic surrogate with those (maximum) curvatures to minimize the above cost function with respect to $\boldsymbol{x}$ via a monotonic algorithm.

todo: does it satisfy the conditions in [49]? if so, replace with optimal curvature. paul reggentin project w15

7.10.4 Multiple receive coils

If we have multiple receive coils, an appropriate measurement model is

$$z_{klj} = s_{kj} f_j \, \mathrm{e}^{-\tau_l x_j} + \varepsilon_{klj}$$

for $k = 1, \ldots, K$ where K is the number of coils and for $l = 0, \ldots, L$ where $\tau_0 = 0$, and where s_{kj} is the sensitivity of the kth coil at the jth voxel. Ignoring possible noise correlation between coils, the negative log-likelihood is

$$\mathsf{L}(\boldsymbol{x}, \boldsymbol{s}, \boldsymbol{f}) = \frac{1}{2\sigma^2} \sum_{k=1}^{K} \sum_{l=0}^{L} \left| z_{klj} - s_{kj} f_j \, \mathrm{e}^{-\tau_l x_j} \right|^2 .$$

We can jointly estimate the underlying object $\boldsymbol{f}$, the sensitivity maps $\boldsymbol{s}_1, \ldots, \boldsymbol{s}_K$ for each coil, and the relaxation map $\boldsymbol{x}$ by combining this log-likelihood with appropriate regularizers. We would use strong quadratic regularization for the coil sensitivity maps because they are smooth functions.

For optimization we need the following partial derivatives:

$$\frac{\partial}{\partial x_j} \mathsf{L}(\boldsymbol{x}, \boldsymbol{s}, \boldsymbol{f}) = \frac{1}{\sigma^2} \sum_{k=1}^{K} \sum_{l=0}^{L} \mathrm{real}\left\{ s_{kj}^* f_j^* \tau_l \, \mathrm{e}^{-\tau_l x_j} \left(z_{klj} - s_{kj} f_j \, \mathrm{e}^{-\tau_l x_j} \right) \right\}$$

$$\frac{\partial^2}{\partial x_j^2} \mathsf{L}(\boldsymbol{x}, \boldsymbol{s}, \boldsymbol{f}) \approx \frac{1}{\sigma^2} \sum_{k=1}^{K} \sum_{l=0}^{L} \left| s_{kj} f_j \tau_l \, \mathrm{e}^{-\tau_l x_j} \right|^2 \approx \kappa_j^2 \triangleq \frac{1}{\sigma^2} \sum_{l=0}^{L} \tau_l \sum_{k=1}^{K} |z_{klj}|^2 .$$

We want a "typical" κ_j value in a good signal region to be about unity to facilitate regularization parameter selection. Let $\bar{\kappa}$ denote, say, the median of the κ_j values in the high signal regions. Then we normalize the data by

$$\tilde{z}_{klj} \triangleq z_{klj} / \bar{\kappa},$$

so that the typical κ_j value will be about unity.

7.10.5 Regularized linear LS relaxation map estimation

Regularized (linear) weighted least-squares methods are also be possible for this problem by taking the logarithm of the magnitudes of y_j and z_{lj} [68].

s,mr,relaxmap,kspace

7.10.6 Relaxation map estimation from k-space data

The image-domain measurement model (7.10.1) assumes implicitly that all of the relaxation occurs at the echo time. In practice, there is also relaxation during the signal readout, *e.g.*, [132], and in some types of scans modeling this relaxation may be important, so we may want to estimate the relaxation map directly from the k-space data. Furthermore, starting with reconstructed images (7.10.1) requires that we either fully sample k-space, or use parallel imaging and/or compressed sensing to handle under-sampled k-space data. Since f_j is complex and x_j is real, there are 3 real unknown parameters per voxel, whereas there are $2(L+1)$ complex reconstructed image values per voxel in (7.10.1) so possibly even more under-sampling could be tolerated. Exploiting this potential is an *open problem*. Ignoring field inhomogeneity, a reasonable model for the k-space data is:

$$\mathsf{E}\left[y_i^{(l)}\right] = \int f(\vec{\mathrm{x}}) \, \mathrm{e}^{-(t_i+\tau_l)\,\alpha(\vec{\mathrm{x}})} \, \mathrm{e}^{-\imath 2\pi \vec{\nu}_i \cdot \vec{\mathrm{x}}} \, \mathrm{d}\vec{\mathrm{x}}, \qquad l = 0, 1, \ldots, L,$$

where $\alpha(\vec{\mathrm{x}})$ denotes the unknown relaxation map. We want to estimate $f(\vec{\mathrm{x}})$ and $\alpha(\vec{\mathrm{x}})$ from $\left\{\boldsymbol{y}^{(l)}\right\}$. This is a joint estimation problem like that described in [69]. One can define a cost function in terms of $\boldsymbol{f}$ and $\boldsymbol{\alpha}$, and then alternate between holding $\boldsymbol{\alpha}$ fixed and minimizing over $\boldsymbol{f}$ (using the conjugate gradient methods) and then holding $\boldsymbol{f}$ fixed and minimizing over $\boldsymbol{\omega}$ (using steepest descent with linearization [69]). Developing suitable optimization transfer methods akin to [122] is an *open problem*. These k-space methods require considerably more computation than the image domain methods, so one should first apply an image-domain method to get a reasonable initial estimate of the relaxation map $\boldsymbol{\alpha}$.

There is also an exponential relationship between contrast concentration and MR signal in some applications, *e.g.*, [134]. Adapting the techniques described above to such applications is an interesting *open problem*.

s,mr,blmap

7.11 B1+ map estimation (s,mr,b1map)

A challenge in MR imaging is that RF transmit coils produce nonuniform field strengths, so an excitation pulse will produce tip angles that vary substantially from the desired tip angle over the field of view. For parallel transmit excitation (using a coil array), it is important to have a map of the B1+ field strength (and phase) for RF pulse design.

A conventional approach to B1 mapping is to collect two scans, one of which uses twice the RF amplitude of the other, *e.g.*, [135–139]. A model for the reconstructed images is

$$y_{j1} = f_j \sin(\alpha_j) + \varepsilon_{1j}$$
$$y_{j2} = f_j \sin(2\alpha_j) + \varepsilon_{1j},$$

where α_j is the unknown tip angle at the jth voxel. Estimating α_j is equivalent to estimating the B1+ field strength at the jth voxel. Using the double angle formula:

$$\frac{\mathsf{E}[y_{j2}]}{\mathsf{E}[y_{j1}]} = \frac{\sin(2\alpha_j)}{\sin(\alpha_j)} = 2\cos(\alpha_j)\,.$$

The standard estimate of α_j is a method-of-moments estimator that ignores the noise in the data:

e,mr,blmap,alf

$$\hat{\alpha}_j = \arccos\left(\frac{1}{2}\frac{y_{j2}}{y_{j1}}\right). \tag{7.11.1}$$

This method has several limitations. It performs poorly in image regions with low spin density, *i.e.*, where y_{j1} is small. It suffers from 2π ambiguities if α_j is too large, yet it would be sensitive to noise if α_j is too small. And it does not immediately generalize to the more general case where we acquire multiple scans to cover a larger range of tip angles, possibly even angles that are larger than 2π in some image regions.

7.11.1 Signal model for multiple coils, multiple tip angles

Suppose there are K coils and we separately transmit from each coil and then receive from a common coil. Suppose for each coil we apply a sequence of L nominal tip angles with known relative RF amplitudes a_l, for $l = 1, \dots, L$. We model the resulting $K \times L$ reconstructed images as follows:

e,mr,blmp,yjkl

$$y_{jkl} = f_j \, \mathrm{e}^{\imath\varphi_{jk}} \sin(a_l x_{jk}) + \varepsilon_{jkl} \tag{7.11.2}$$

for $k = 1, \dots, K$ and $j = 1, \dots, n_\mathrm{p}$, where f_j denotes the underlying object transverse magnetization in the jth voxel, φ_{jk} denotes the phase of the kth coil at the jth voxel, and ε_{jkl} denotes zero-mean complex gaussian noise. Finally, x_{jk} denotes the unknown "B1 map" that relates RF amplitude to tip angle at the jth voxel for the kth coil. If the units of the amplitudes a_l are gauss, then the units of x_{jk} will be radians per gauss. More typically, the units of a_l are arbitrary, and all that is known is their relative values. In this case x_{jk} will have units such that the product of a_l and x_{jk} has units of radians. This should suffice for RF pulse design.

The goal is to estimate each B1 map $\boldsymbol{x}_k \triangleq (x_{1k}, \dots, x_{n_\mathrm{p}k})$ and phase map $\boldsymbol{\phi}_k \triangleq (\varphi_{1k}, \dots, \varphi_{n_\mathrm{p}k})$ from the reconstructed images $\{y_{jkl}\}$. The underlying magnetization $\boldsymbol{f} \triangleq (f_1, \dots, f_{n_\mathrm{p}})$ is also unknown but is a **nuisance parameter**. We would like the estimator to work robustly even in image regions where f_j is small.

If f_j were allowed to be complex, then the model above would be non-identifiable because we could add phase to $\boldsymbol{f}$ and subtract the same phase from each $\boldsymbol{\phi}_k$ and $\mathsf{E}[y_{jkl}]$ would remain unchanged. To make the problem identifiable, one could assume that φ_{j1} is zero and then all the other φ_{jk} values would be relative phases. Instead, we take the approach of constraining $\boldsymbol{f}$ to be real. This reduces the ambiguity to a sign change of $\boldsymbol{f}$ and a corresponding π phase shift in each φ_{jk}.

Kerr et al. [140] consider a similar problem, except they assume the a_l values are powers of two, and they use the following cost function:

$$\sum_l \left(|y_{jkl}| - |f_j| \sin(|a_l x_{jk}|)\right)^2.$$

This cost function does not corresponding to the complex gaussian statistical model for the data. They applied a general purpose minimization method from MATLAB. Most importantly, for each voxel they used only the value of tip index l for which the tip was closest to $\pi/2$. In contrast, we use all the data at every voxel, with a statistically motivated cost function, and a minimization algorithm that is tailored to this problem. We allow arbitrary choices for the a_l values, although powers of two may be a reasonable choice.

7.11.2 Regularized estimator

We propose to jointly estimate the B1 maps $\boldsymbol{x} = (\boldsymbol{x}_1, \dots, \boldsymbol{x}_K)$, the phase maps $\boldsymbol{\phi} = (\boldsymbol{\phi}_1, \dots, \boldsymbol{\phi}_K)$, and the object $\boldsymbol{f}$ by finding minimizers of the following cost function:

$$\Psi(\boldsymbol{x}, \boldsymbol{\phi}, \boldsymbol{f}) = \sum_{k=1}^{K} \left[\sum_{j=1}^{n_\mathrm{p}} \sum_{l=1}^{L} \frac{1}{2} \left| y_{jkl} - f_j \, \mathrm{e}^{\imath \varphi_{jk}} \sin(a_l x_{jk}) \right|^2 + \beta_1 \, \mathsf{R}(\boldsymbol{x}_k) + \beta_2 \, \mathsf{R}(\boldsymbol{\phi}_k) \right] .$$

We use quadratic regularization for the B1 maps $\boldsymbol{x}_k$ and the phase maps $\boldsymbol{\phi}_k$ because these are expected be spatially smooth [141, 142], although edge-preserving regularization could be used if needed. However, we choose not to regularize the magnetization image $\boldsymbol{f}$ because it will contain detailed structural information.

There is no analytical solution for the minimizer of $\Psi(\boldsymbol{x}, \boldsymbol{\phi}, \boldsymbol{f})$ over all three sets of parameters, so iterative methods are required. We consider an block alternating minimization approach in which we minimize Ψ by cycling over each of the three parameter types and minimizing with respect to one parameter vector while holding the other two at their most recent values.

For given estimates of $\boldsymbol{\phi}$ and $\boldsymbol{x}$, the minimizer of Ψ with respect $\boldsymbol{f}$ is found analytically to be

$$f_j = \mathrm{real} \left\{ \frac{\sum_{k=1}^{K} \sum_{l=1}^{L} \mathrm{e}^{-\imath \varphi_{jk}} \sin(a_l x_{jk}) \, y_{jkl}}{\sum_{k=1}^{K} \sum_{l=1}^{L} \sin^2(a_l x_{jk})} \right\} . \tag{7.11.3}$$

e,mr,blmap,fj

For given $\boldsymbol{\phi}$ and $\boldsymbol{f}$ values, the problem of minimizing Ψ with respect to the B1 map $\boldsymbol{x}_k$ appears nontrivial because of the nonlinearity of $\sin(a_l x_{jk})$. Consider just one term in this cost function:

$$\psi(y, g, a, x) = \frac{1}{2} |y - g \sin(ax)|^2 \equiv - \mathrm{real}\{y g^*\} \sin(ax) + \frac{1}{2} |g|^2 \sin^2(ax) .$$

The relevant derivatives of this term are:

$$\begin{aligned} \frac{\partial}{\partial x} \psi(y, g, a, x) &= - \mathrm{real}\{y g^*\} \, a \cos(ax) + |g|^2 \, a \sin(ax) \cos(ax) \\ &= -a \cos(ax) \, \mathrm{real}\{g^* \, (y - g \sin(ax))\} \\ \frac{\partial^2}{\partial x^2} \psi(y, g, a, x) &= \mathrm{real}\{y g^*\} \, a^2 \sin(ax) + |g|^2 \, a^2 \cos(2ax) . \end{aligned} \tag{7.11.4}$$

e,mr,blmap,dder

An upper bound for the curvature is

$$\begin{aligned} \frac{\partial^2}{\partial x^2} \psi(y, g, a, x) &\le a^2 \left[|yg| \sin(ax) + |g|^2 \cos(2ax) \right] \\ &\approx a^2 |g|^2 \left[\sin^2(ax) + \cos(2ax) \right] = a^2 |g|^2 \cos^2(ax) \le a^2 |g|^2 . \end{aligned}$$

Thus, using the quadratic majorizer principles described in [143] and Chapter 12, a natural iteration for updating $\boldsymbol{x}_k$ is:

$$\boldsymbol{x}_k^{(n+1)} = \boldsymbol{x}_k^{(n)} - \mathsf{diag} \left\{ \frac{1}{\sum_{l=1}^{L} a_l^2 |f_j|^2 + r \beta_1} \right\} \nabla_{\boldsymbol{x}_k} \Psi(\boldsymbol{x}^{(n)}, \boldsymbol{\phi}, \boldsymbol{f}) .$$

The factor "r" depends on the choice of the regularizer $\mathsf{R}(\boldsymbol{x}_k)$; see (1.11.5) and Example 12.6.1. For 2nd-order finite differences with the 8 nearest neighbors, this factor is $4 \cdot 4 \cdot (2 + 2/\sqrt{2})$.

MIRT *See* `Robject.denom`.

For given $\boldsymbol{f}$ and $\boldsymbol{x}$ values, the problem of finding the minimizer with respect to the phase map $\boldsymbol{\phi}$ has essentially the same mathematical form as the fieldmap estimation problem described in (7.9.3) and (7.9.5). In particular,

$$\sum_{k=1}^{K} \sum_{l=1}^{L} \frac{1}{2} \left| y_{jkl} - f_j \, \mathrm{e}^{\imath \varphi_{jk}} \sin(a_l x_{jk}) \right|^2 \equiv - \sum_{k=1}^{K} \mathrm{real} \left\{ \left[f_j \sum_{l=1}^{L} \sin(a_l x_{jk}) \, y_{jkl} \right] \mathrm{e}^{-\imath \varphi_{jk}} \right\} . \tag{7.11.5}$$

e,mr,blmap,kost,phi

Therefore we can apply the iteration (7.9.7) with appropriate variables, as follows:

$$\boldsymbol{\phi}_k^{(n+1)} = \boldsymbol{\phi}_k^{(n)} - \mathsf{diag} \left\{ \frac{1}{\sum_{l=1}^{L} |y_{jkl} f_j \sin(a_l x_{jk})| + r \beta_2} \right\} \nabla_{\boldsymbol{\phi}_k} \Psi(\boldsymbol{x}, \boldsymbol{\phi}^{(n)}, \boldsymbol{f}) .$$

Note that the only "coupling" between the estimates for the various coils occurs in the object update (7.11.3). The updates to the B1 maps $\boldsymbol{x}_k$ and the phase maps φ_k are decoupled, so they can be parallelized.

s,mr,b1map,init

7.11.3 Initialization

The cost function Ψ is nonconvex, so the alternating minimization algorithm described above will descend from the initial estimates to a local minimum [116]. Thus it is desirable to choose reasonable initial estimates. For $\boldsymbol{x}_k$, the standard double angle method (7.11.1) is a natural choice. For φ_k, (7.11.5) suggests:

$$\varphi_{jk} = \angle \left(f_j \sum_{l=1}^{L} \sin(a_l x_{jk}) \, y_{jkl} \right).$$

Finally, for $\boldsymbol{f}$ we can use (7.11.3).

MIRT *See* `mri_b1map`.

7.11.4 Cramér-Rao bound analysis

What are the optimal relative amplitudes $\{a_l\}$ for B1 mapping? To address this question, we turn to the **Cramér-Rao** bound (**CRB**). Consider the 1D model

$$y_l = g \sin(a_l x) + \varepsilon_l,$$

with independent complex gaussian noise. Let $\theta = a_1 x$ and define $c_l = a_l / a_1$. Then the negative log-likelihood for θ

$$-\log \mathsf{p}(\boldsymbol{y}; \theta) \equiv \sum_{l=1}^{L} \frac{1}{2\sigma^2} |y_l - g \sin(c_l \theta)|^2$$

so the Fisher information with respect to θ is, using (7.11.4):

$$-\mathsf{E}\left[\frac{\partial^2}{\partial \theta^2} \log \mathsf{p}(\boldsymbol{y}; \theta) \right] = \frac{|g|^2}{\sigma^2} \sum_{l=1}^{L} c_l^2 \left[\sin^2(c_l \theta) + \cos(2 c_l \theta) \right] = \frac{|g|^2}{\sigma^2} \sum_{l=1}^{L} c_l^2 \cos^2(c_l \theta) \,.$$

This expression is the product of a signal-to-noise ratio, $|g|^2/\sigma^2$, times a factor that depends both on the tip angle θ, and the relative amplitudes $\{c_l\}$. We would like the estimator to have high Fisher information *regardless of the (unknown) value of* θ. A natural criterion is to maximize the worst-case Fisher information:

$$\max_{\{c_l\}} \min_{\theta} \sum_{l=1}^{L} c_l^2 \cos^2(c_l \theta) = \left[\cos^2(\theta) + \sum_{l=2}^{L} c_l^2 \cos^2(c_l \theta) \right].$$

Performing this optimization numerically, we find that $\boldsymbol{c} = (1, 2)$ is optimal for $L = 2$. For $L = 3$, the best choice depends on the maximum relative amplitude allowed. If we require $c_3 < 4.3$, then the optimum is $\boldsymbol{c} = (1, c_3 - 1, c_3)$, *e.g.*, $\boldsymbol{c} = (1, 3, 4)$. If we can allow $c_3 > 4.3$, then the optimum is $\boldsymbol{c} = (1, c_3/2, c_3)$, and one should increase c_3 as much as possible to maximize the worst-case Fisher information, *e.g.*, $\boldsymbol{c} = (1, 3, 6)$. The choice $\boldsymbol{c} = (1, 3, 4)$ has slightly higher worst-case Fisher information than the choice $\boldsymbol{c} = (1, 2, 4)$, and also has modestly better mean Fisher information (averaged over possible θ values). It seems difficult to generalize these conclusions to $L > 3$, so one would need to use numerical methods.

7.11.5 Simulation study

To evaluate the regularized B1 map estimation method described above, we performed a simulation study using the true images shown in Fig. 7.11.3. We simulated noisy reconstructed images for $L = 3$ different nominal tip angles and $K = 4$ different transmit coils using the measurement model (7.11.2). The relative amplitudes were $a_l = (10, 20, 30)$. We added complex gaussian noise such that the SNR, defined by $10 \log_{10}(\|\boldsymbol{y}\| / \|\boldsymbol{y} - \mathsf{E}[\boldsymbol{y}]\|)$ was about 21 dB, yielding the images shown in Fig. 7.11.1. Fig. 7.11.2 shows the initial estimates using the methods described in §7.11.3. Note that the standard double angle method only uses two of the three scans. Fig. 7.11.4 shows the regularized estimates. The reduced noise due to regularization and due to using all the scan data is evident.

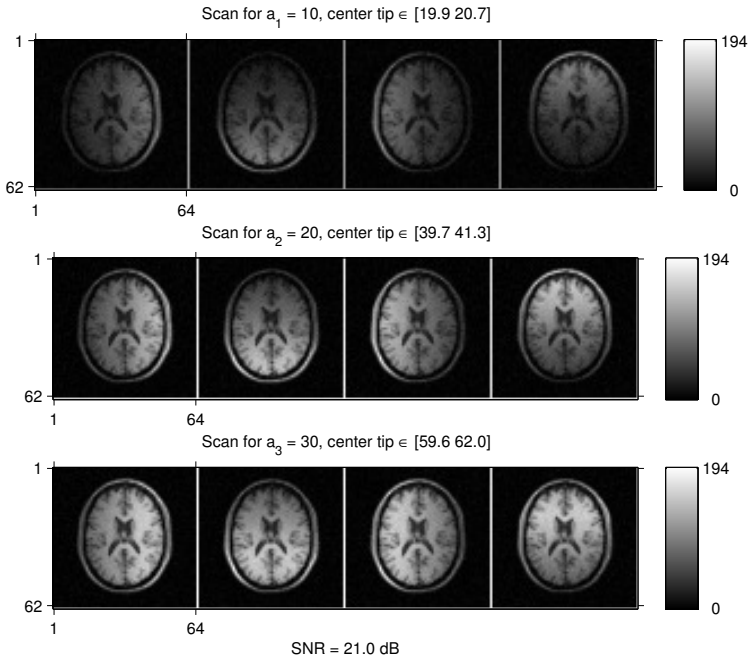

fig_mri_blmap_siml_yi

Figure 7.11.1: Simulated MR scans for $L = 3$ different nominal tip angles for $K = 4$ different transmit coils.

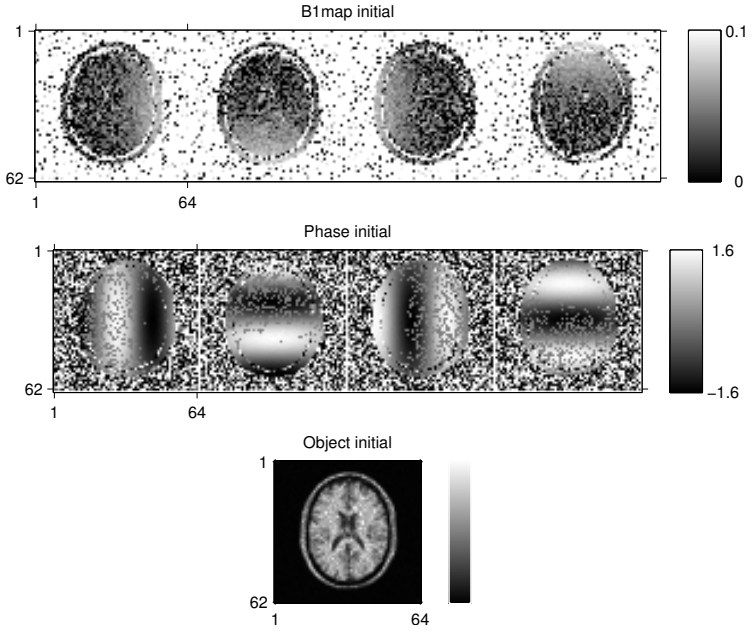

fig_mri_blmap_sim1_init

Figure 7.11.2: Initial estimates of B1 maps, phase maps, and object.

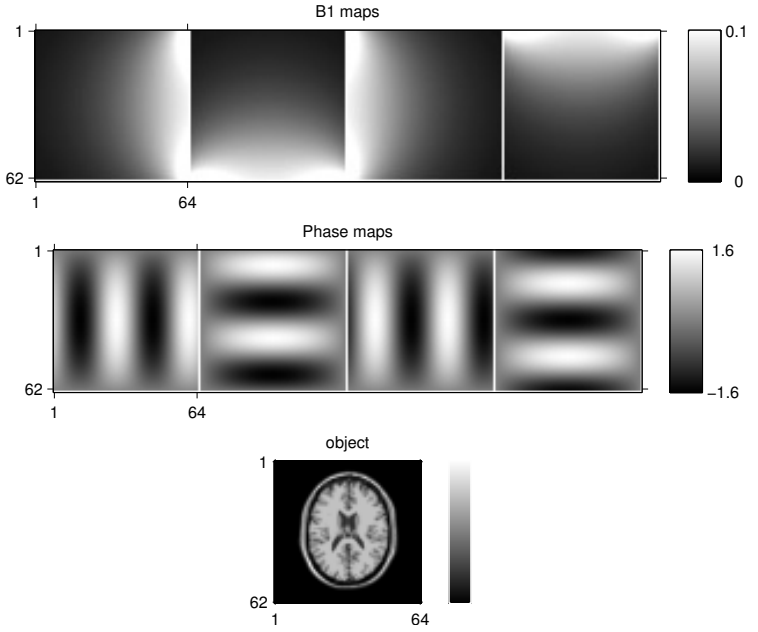

fig_mri_blmap_sim1_true

Figure 7.11.3: True B1 maps, phase maps, and object used in simulation.

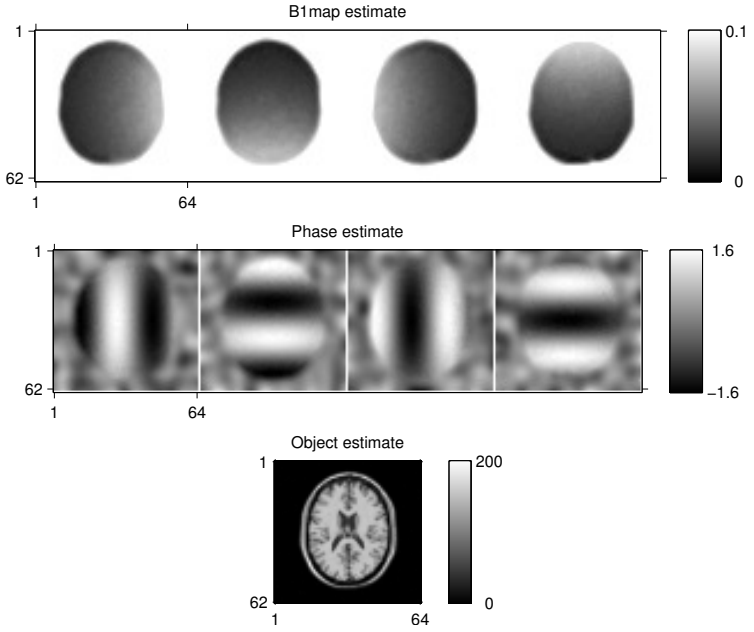

fig_mri_blmap_siml_hat

Figure 7.11.4: Regularized estimates of B1 maps, phase maps, and object.

s,mr,sense

7.12 Sensitivity encoded (SENSE) imaging (s,mr,sense)

The standard Fourier model considered in Chapter 6 ignores the nonuniform sensitivity of receive coils used in MR imaging. For qualitative MR imaging, these nonuniform sensitivities are a minor inconvenience and just cause some image shading. For quantitative purposes like image segmentation, nonuniform coil sensitivity creates a significant challenge and numerous post-processing methods have been developed for correcting these effects, often called **bias correction**, *e.g.*, [152–160]. When multiple receive coils are available, each with a distinct sensitivity pattern, the partial spatial localization provided by the coils can be exploited to accelerate scanning. This is known as **parallel imaging** in MRI. We focus here on **sensitivity encoded** or (**SENSE**) imaging [161, 162].

In sensitivity encoding MR imaging, the signal model becomes

$$s_l(t) = \int_{\mathcal{D}} f(\vec{\mathrm{x}})\, s_l(\vec{\mathrm{x}})\, \mathrm{e}^{-\imath 2\pi \vec{k}(t)\cdot \vec{\mathrm{x}}}\, \mathrm{d}\vec{\mathrm{x}},$$

where $s_l(\vec{\mathrm{x}})$ is the **sensitivity map** of the lth of L receive coils. Sampling and discretizing as in §7.2 yields the matrix formulation

e,mr,sense,B

$$\boldsymbol{y} = \boldsymbol{B}\boldsymbol{x} + \boldsymbol{\varepsilon}, \qquad \boldsymbol{y} = \begin{bmatrix} \boldsymbol{y}_1 \\ \vdots \\ \boldsymbol{y}_L \end{bmatrix}, \qquad \boldsymbol{B} = \begin{bmatrix} \boldsymbol{A}\boldsymbol{S}_1 \\ \vdots \\ \boldsymbol{A}\boldsymbol{S}_L \end{bmatrix}, \tag{7.12.1}$$

where $\boldsymbol{S}_l = \mathsf{diag}\{s_{lj}\}$ with $s_{lj} = s_l(\vec{\mathrm{x}}_j)$ and $\boldsymbol{A}$ is the Fourier encoding matrix given in (7.2.5). Given sensitivity maps $\{\boldsymbol{s}_1, \ldots, \boldsymbol{s}_L\}$, one can perform penalized-likelihood image reconstruction of $\boldsymbol{x}$ by minimizing the following cost function:

e,mr,sense,cost

$$\hat{\boldsymbol{x}} = \arg\min_{\boldsymbol{x}} \Psi(\boldsymbol{x}), \qquad \Psi(\boldsymbol{x}) = \frac{1}{2} (\boldsymbol{y} - \boldsymbol{B}\boldsymbol{x})' \boldsymbol{W} (\boldsymbol{y} - \boldsymbol{B}\boldsymbol{x}) + \mathsf{R}(\boldsymbol{x}), \tag{7.12.2}$$

where $\boldsymbol{W}$ denotes the inverse of the noise covariance matrix, *i.e.*, $\boldsymbol{W} = [\mathsf{Cov}\{\boldsymbol{y}\}]^{-1}$.

One can combine SENSE with other acceleration techniques including **compressed sensing** approaches [163].

7.12.1 Quadratic regularization

The estimator (7.12.2) is simplest if the regularizer $\mathsf{R}(\boldsymbol{x})$ in (7.12.2) is quadratic with Hessian R. We focus on that case hereafter. (This includes the particularly popular case where Tikhonov regularization is used, *i.e.*, $\mathsf{R}(\boldsymbol{x}) = \beta \frac{1}{2} \|\boldsymbol{x}\|^2$, in which case $\mathsf{R} = \beta \boldsymbol{I}$. In the quadratic case we have the analytical solution:

e,mr,sense,xh

$$\hat{\boldsymbol{x}} = [\boldsymbol{B}'\boldsymbol{W}\boldsymbol{B} + \mathsf{R}]^{-1} \boldsymbol{B}'\boldsymbol{W}\boldsymbol{y} = [\mathsf{F} + \mathsf{R}]^{-1} \boldsymbol{B}'\boldsymbol{W}\boldsymbol{y}, \tag{7.12.3}$$

where the Fisher information matrix is given by

$$\mathsf{F} = \boldsymbol{B}'\boldsymbol{W}\boldsymbol{B}.$$

Because of the data ordering in (7.12.1), the covariance matrix $\boldsymbol{W}$ will have the form

$$\boldsymbol{W} = \boldsymbol{K} \otimes \boldsymbol{I},$$

where $\boldsymbol{I}$ is a $n_\mathrm{d} \times n_\mathrm{d}$ identity matrix, and $\boldsymbol{K}$ is the inverse of the $L \times L$ covariance matrix of the $L \times 1$ vector $\boldsymbol{y}_{:,i} = (y_{1i}, \ldots, y_{Li})$. Thus the Fisher information matrix simplifies to

e,mr,sense,F

$$\mathsf{F} = \sum_{l'=1}^{L} \sum_{l=1}^{L} K_{l'l} \boldsymbol{S}_{l'}' \boldsymbol{A}' \boldsymbol{A} \boldsymbol{S}_l. \tag{7.12.4}$$

The simplest case is when $\boldsymbol{W} = \boldsymbol{I}$, in which case

$$\mathsf{F} = \sum_{l=1}^{L} \boldsymbol{S}_l' \boldsymbol{A}' \boldsymbol{A} \boldsymbol{S}_l.$$

For the case $\boldsymbol{R} = \beta \boldsymbol{I}$, one can choose β based on the maximum eigenvalue of F [164].

s,mr,sensemap

7.13 Sensitivity map estimation (s,mr,sensemap)

In sensitivity encoding MR imaging [161], many image reconstruction methods require estimates of the sensitivity maps of each receive coil. This section describes estimation methods for sensitivity maps.

7.13.1 Estimation from $L+1$ images

The standard approach to estimating sensitivity maps uses the following procedure. First one collects fully-sampled k-space data using both the body coil and each of the L individual receive coils. Then one reconstructs $L+1$ images from those measured k-space data sets. Assuming that the body coil has essentially uniform sensitivity over the field of view, one models the image $\boldsymbol{y}$ reconstructed from the body coil image as

e,mr,sensemap,yj

$$y_j = f_j + \varepsilon_j, \qquad j = 1, \dots, n_{\mathrm{p}}, \tag{7.13.1}$$

where $\boldsymbol{f} = f_1, \dots, f_{n_{\mathrm{p}}}$ denotes the true underlying object magnetization, and $\boldsymbol{\varepsilon}$ represents noise in that body coil image. Then one models the images reconstructed from each of the other receive coils as follows:

e,mr,sensemap,zlj

$$z_{lj} = s_{lj} f_j + \eta_{lj}, \qquad l = 1, \dots, L, \qquad j = 1, \dots, n_{\mathrm{p}}, \tag{7.13.2}$$

where $\boldsymbol{s}_l = (s_{l1}, \dots, s_{ln_{\mathrm{p}}})$ denotes the **sensitivity map** of the lth coil. The goal is to estimate the s_{lj} factors from the $L+1$ images $\boldsymbol{y}, \boldsymbol{z}_1, \dots, \boldsymbol{z}_L$. Because RF coil sensitivity factors are complex in general, one must use *complex* reconstructed images here.

7.13.1.1 Conventional approach for $L+1$ images

The conventional estimate is to simply *divide* the body coil image into each receive coil image as follows [162]:

e,mr,sensemap,usual

$$\hat{s}_{lj}^{\text{conventional}} = \frac{z_{lj}}{y_j}, \qquad l = 1, \dots, L, \qquad j = 1, \dots, n_{\mathrm{p}}. \tag{7.13.3}$$

This estimate would work adequately in the absence of noise, but, being a ratio, noise will severely corrupt this estimate anywhere that the body coil image magnitude is small. One can attempt to smooth the ratio to reduce the noise [162], under the (usually reasonable) assumption that the sensitivity map is a spatially smooth function. But such smoothing is difficult because the variance of the estimate is very nonstationary.

A preferable approach is to *avoid the division* altogether, by treating the task as an estimation problem. The following sections describe estimation methods both for the model (7.13.2) and for a practically preferable case where no body coil image is acquired.

7.13.1.2 Maximum-likelihood estimation for $L+1$ images

Following §7.9.2, we first analyze a ML approach to finding $\{\boldsymbol{s}_1, \dots, \boldsymbol{s}_L\}$ and $\boldsymbol{f}$ from $\boldsymbol{y}$ and $\{\boldsymbol{z}_1, \dots, \boldsymbol{z}_L\}$. We assume that the measurement noise values in (7.13.1) and (7.13.2) are all complex white gaussian with the same variance σ^2 and independent. Defining $\boldsymbol{s} = (\boldsymbol{s}_1, \dots, \boldsymbol{s}_L)$, the joint negative log-likelihood of $\boldsymbol{f}$ and $\boldsymbol{s}$ is

e,mr,sensemap,ll

$$\begin{aligned}
\mathsf{L}(\boldsymbol{f}, \boldsymbol{s}) &= -\log \mathsf{p}(\boldsymbol{y}; \boldsymbol{f}) - \sum_{l=1}^{L} \log \mathsf{p}(\boldsymbol{z}_l; \boldsymbol{f}, \boldsymbol{s}_l) \\
&\equiv \sum_{j=1}^{n_{\mathrm{p}}} \left[|y_j - f_j|^2 + \sum_{l=1}^{L} |z_{lj} - s_{lj} f_j|^2 \right] \\
&= \frac{1}{2\sigma^2} \sum_{j=1}^{n_{\mathrm{p}}} \|\boldsymbol{a}_j f_j - \boldsymbol{b}_j\|^2 ,
\end{aligned} \tag{7.13.4}$$

where $\boldsymbol{a}_j \triangleq (1, s_{1j}, \dots, s_{Lj})$ and $\boldsymbol{b}_j \triangleq (y_j, z_{1j}, \dots, z_{Lj})$. Joint ML estimation of $\boldsymbol{f}$ and $\boldsymbol{s}$ involves the following optimization problem:

$$\arg\min_{\boldsymbol{s} \in \mathbb{C}^{n_{\mathrm{p}} \times L}} \arg\min_{\boldsymbol{f} \in \mathbb{C}^{n_{\mathrm{p}}}} \mathsf{L}(\boldsymbol{f}, \boldsymbol{s}) .$$

Minimizing first over $\boldsymbol{s}$ yields $\hat{s}_{lj} = z_{lj} / \hat{f}_j$, and then substituting this into (7.13.4) and minimizing over f_j yields $\hat{f}_j = y_j$. Combining these two ML estimates yields the usual sensitivity map estimator (7.13.3). Just as in the

fieldmap estimation problem, the conventional method for determining coil sensitivity patterns is in fact a ML estimator. Because this estimator is sensitive to noise, we again proceed to explore regularized alternatives.

In the fieldmap case, we first found the ML estimate of $\boldsymbol{f}$, substituted that into the log-likelihood, and then added a penalty function to discourage rough fieldmaps. We can also attempt the same approach here. The ML estimate of f_j for given value of $\boldsymbol{s}$ is

$$\hat{f}_j = \frac{\boldsymbol{a}_j' \boldsymbol{b}_j}{\|\boldsymbol{a}_j\|^2} = \frac{y_j + \sum_{l=1}^L s_{lj}^* z_{lj}}{1 + \sum_{l=1}^L |s_{lj}|^2}. \tag{7.13.5}$$

e,mr,sensemap,fhj

Substituting this estimate back into the log-likelihood and simplifying yields the following expression for the negative log-likelihood after optimizing over $\boldsymbol{f}$:

$$\mathsf{L}(\boldsymbol{s}) \triangleq \min_{\boldsymbol{f}} \mathsf{L}(\boldsymbol{f}, \boldsymbol{s}) \equiv \sum_{j=1}^{n_\mathrm{p}} \frac{\left|\boldsymbol{a}_j' \boldsymbol{b}_j\right|^2}{\|\boldsymbol{a}_j\|^2} = \sum_{j=1}^{n_\mathrm{p}} \frac{\left|y_j + \sum_{l=1}^L s_{lj}^* z_{lj}\right|^2}{1 + \sum_{l=1}^L |s_{lj}|^2}.$$

One could incorporate a roughness penalty for $\boldsymbol{s}$ and then optimize the resulting penalized-likelihood objective function by some gradient-based method to estimate the sensitivity maps $\boldsymbol{s}$. However, the form of the "reduced" log-likelihood $\mathsf{L}(\boldsymbol{s})$ seems more complicated than the original form in (7.13.4). Perhaps there is some quadratic approximation to $\mathsf{L}(\boldsymbol{s})$ that could be made, by analogy with (7.9.4), but finding one is an *open problem*. Instead, the next section formulates a penalized-likelihood approach using the original expression (7.13.4).

An alternative approach is given in [169]. That method assumes a certain noise model for the sensitivity maps $\hat{s}_{lj}$ and accounts for that variability in the data covariance. Other joint estimation approaches are in [170–172]. [173] [174] [175]. [176]

7.13.1.3 Penalized-likelihood approach for $L+1$ images

To control noise in the sensitivity maps $\boldsymbol{s}$, and to provide interpolation and extrapolation of those maps to voxels where the image magnitude is small, we propose a joint estimation approach based on the following penalized-likelihood objective function:

$$\mathsf{L}(\boldsymbol{f}, \boldsymbol{s}) + \beta \sum_{l=1}^L \mathsf{R}(\boldsymbol{s}_l), \tag{7.13.6}$$

e,mr,sensemap,pl

where $\mathsf{R}(\boldsymbol{s}_l)$ is a roughness penalty that encourages the lth sensitivity map to be smooth.

To compute the penalized-likelihood estimates, we propose an **alternating maximization** approach in which we alternate between updating the estimate of the image $\boldsymbol{f}$ using (7.13.5), and then using that new estimate to update all of the sensitivity maps. This two-step process is then repeated, hopefully leading to convergence. Given the current estimate of $\boldsymbol{f}$, the estimates of each $\boldsymbol{s}_l$ can proceed in parallel. To maximize the penalized-likelihood objective function with respect to $\boldsymbol{s}_l$ is equivalent to minimizing the following cost function:

$$\boldsymbol{s}_l{}^{\mathrm{new}} = \arg\min_{\boldsymbol{s}_l \in \mathbb{C}^{n_\mathrm{p}}} \Psi_l(\boldsymbol{s}_l), \quad \Psi_l(\boldsymbol{s}_l) = \left\| \boldsymbol{z}_l - \mathsf{diag}\left\{\hat{f}_j\right\} \boldsymbol{s}_l \right\|^2 + \beta\, \mathsf{R}(\boldsymbol{s}_l)\,. \tag{7.13.7}$$

e,mr,sensemap,pl,vsl

Some recent methods based on related formulations have used edge preserving regularization, *e.g.*, [177]. Because sensitivity maps are usually smooth, we usually use quadratic regularization, in which case (7.13.7) is a standard quadratically penalized least-squares problem. The QPWLS-CG algorithm can readily minimize $\Psi_l(\boldsymbol{s}_l)$.

7.13.1.4 Approximate regularized approach for $L+1$ images

If the SNR in the body coil image $\boldsymbol{y}$ is reasonable, then one might hope that the estimate of $\boldsymbol{f}$ in (7.13.5) would converge approximately to simply $\tilde{f}_j = y_j$. Substituting this approximation into (7.13.7) yields the following regularized least-squares cost function:

$$\tilde{\Psi}(\boldsymbol{s}_l) = \|\boldsymbol{z}_l - \mathsf{diag}\{y_j\}\, \boldsymbol{s}_l\|^2 + \beta\, \mathsf{R}(\boldsymbol{s}_l)\,. \tag{7.13.8}$$

e,mr,sensemap,kost,approx

With this approximation, we estimate each sensitivity map independently of the others by minimizing $\tilde{\Psi}(\boldsymbol{s}_l)$ using QPWLS-CG, or by a non-iterative method that exploits the fact that the Hessian is banded in this case. Computationally, (7.13.8) is preferable because there is no need to alternate between updating $\boldsymbol{s}$ and $\boldsymbol{f}$, but it has the potential drawback that it does not fully exploit the dependence of $\boldsymbol{z}_l$ on $\boldsymbol{f}$. A variational version of this simplified approach was presented in [178].

7.13.2 Sensitivity map estimation from L images

Acquiring a body coil image $\boldsymbol{y}$ requires extra data acquisition time, and can be inconvenient in some MR scan protocols. It would be preferable to estimate the L sensitivity maps $\boldsymbol{s}_1, \ldots, \boldsymbol{s}_L$ from the L receive coil images $\boldsymbol{z}_1, \ldots, \boldsymbol{z}_L$ alone, *without* using any body coil image $\boldsymbol{y}$. A few methods have been proposed for this problem, *e.g.*, [179, 180]. Because the underlying object image $\boldsymbol{f}$ is also unknown, this task may seem impossible because there are $L+1$ unknown vectors, but only L data vectors given.

7.13.2.1 Conventional approach for L images

When combining images from multiple coils, often one simply takes the square root of the sum-of-squares (**SSOS**) of the images [181, 182]:

$$z_j \triangleq \sqrt{\sum_{l=1}^{L} |z_{lj}|^2}. \tag{7.13.9}$$

e,mr,sensmap,ssos

The resulting image will be shaded by the nonuniformity of the SSOS of the coil sensitivity patterns, *i.e.*,

$$z_j \approx |f_j| \, \eta_j,$$

where

$$\eta_j \triangleq \sqrt{\sum_{l=1}^{L} |s_{lj}|^2}.$$

Often these factors $\{\eta_j\}$ are sufficiently smooth and uniform so the residual shading is tolerable. Post-processing methods can correct for such intensity variations, as mentioned in §7.12.

Assume that the phase of the sensitivity map is likely to be much smoother than the phase of the image $\boldsymbol{f}$. Combining this with the intuition of the SSOS approach leads to the following "conventional" approach for estimating sensitivity maps:

$$\hat{s}_{lj} \triangleq \frac{z_{lj}}{z_j} \mathrm{e}^{-\imath \angle z_{1j}}. \tag{7.13.10}$$

e,mr,sensemap,L,ratio

(The phase term is not always included, and the numerator and denominator may be smoothed prior to the ratio [182].) In the absence of noise, *i.e.*, if $z_{lj} = s_{lj} f_j$, then we would have

$$\hat{s}_{lj} = s_{lj} f_j \, \mathrm{e}^{-\imath \angle (s_{1j} f_j)} \, / \, (|f_j| \, \eta_j) = |s_{lj}| \, \mathrm{e}^{-\imath \angle (s_{lj} - s_{1j})} \, / \eta_j,$$

which would be adequate for SENSE reconstruction because the relative coil phases would be correct and the magnitudes would be approximately correct to within the SSOS factors η_j that are hopefully approximately spatially uniform. However, in the presence of noise, the ratio in (7.13.10) will be sensitive to noise in regions with low signal. We use the sum-of-squares example above and hereafter, but the ideas generalize readily to other such "normalization" methods. All such methods will exhibit similar problems in low-signal regions.

We know that physically the sensitivity maps are smooth, including in regions where the body coil image magnitude is small. This suggests that we can use regularization to estimate the sensitivity maps, avoiding the division.

7.13.2.2 SSOS revisited as a ML estimator

Using the conventional sensitivity map ratio estimate (7.13.10), the ML estimate for the object f_j, ignoring noise correlations, is similar to (7.13.5):

$$\hat{f}_j = \frac{\sum_{l=1}^{L} \hat{s}_{lj}^* z_{lj}}{\sum_{l=1}^{L} |\hat{s}_{lj}|^2} = \mathrm{e}^{\imath \angle z_{1j}} \, z_j \frac{\sum_{l=1}^{L} z_{lj}^* z_{lj}}{\sum_{l=1}^{L} |z_{lj}|^2} = \mathrm{e}^{\imath \angle z_{1j}} \, z_j, \tag{7.13.11}$$

e,mr,sensemap,ml,combine

which is the same as the SSOS estimate (7.13.9) except for the (optional) complex phase associated with the first coil. In other words, the SSOS estimate is a ML estimate of f_j based on the (noisy) ratio estimate (7.13.10) for the sensitivity maps.

A better approach is to use a regularized estimate of the sensitivity maps, as described next.

7.13.2.3 Regularized approach for L images

Rearranging the division in (7.13.10) suggests the following:

$$z_{lj} \approx s_{lj} z_j \, \mathrm{e}^{\imath \angle z_{1j}} ,$$

where $z_j \triangleq \sqrt{\sum_{l=1}^{L} |z_{lj}|^2}$. In the presence of noise with variance σ^2, it may be better to use the estimate:

$$z_j \triangleq \sqrt{\left[\left(\sum_{l=1}^{L} |z_{lj}|^2 \right) - L\sigma^2 \right]_+} .$$

Therefore we propose the following regularized cost function for estimating (separately) each sensitivity map:

$$\hat{\boldsymbol{s}}_l \triangleq \arg\min_{\boldsymbol{s} \in \mathbb{C}^{n_\mathrm{p}}} \frac{1}{2} \left\| \boldsymbol{z}_l - \mathsf{diag}\left\{ z_j \, \mathrm{e}^{\imath \angle z_{1j}} \right\} \boldsymbol{s} \right\|^2 + \beta \, \mathsf{R}(\boldsymbol{s}) . \tag{7.13.12}$$

e,mr,sensemap,reg

Spatial resolution analysis Chapter 22 shows that the effective regularization parameter here is β / z_j^2, so there is more smoothing in the regions with low signal, as desired. To simplify selecting β, we normalize the z_j values by the median of all values above 10% of the maximum z_j value prior to iterating.

To accelerate computation, it may be helpful to use a preconditioner such as the diagonal of the Hessian of the above cost function, given by

$$\boldsymbol{D} = \mathsf{diag}\left\{ |z_j|^2 \right\} + K\beta,$$

where K is the typical element of $\boldsymbol{C}'\boldsymbol{C}$ and corresponds to the number of neighbors or $\sum_k |c_{kj}|^2$.

For moderate sized images and quadratic regularization, one can solve (7.13.12) noniteratively using a sparse Cholesky decomposition [16].

MIRT *See* `mri_sensemap_denoise.m`.

After estimating the sensitivity maps using this regularized approach, one can perform the ML **coil combination** (7.13.11) to estimate f_j.

MIRT *See* `ir_mri_coil_combine.m`.

7.13.2.4 Regularized joint-estimation approach for L images

Because the sensitivity maps are smooth, the number of degrees of freedom needed to estimate each $\boldsymbol{s}_l$ should be less than the number of pixels n_p. This fact suggests that it may be possible to estimate the $L+1$ unknowns $\boldsymbol{s}_1, \ldots, \boldsymbol{s}_L$ and $\boldsymbol{f}$ from the L images $\boldsymbol{z}_1, \ldots, \boldsymbol{z}_L$ by using suitable regularization. For this problem we propose a joint estimation approach based on a regularized least-squares cost function:

$$(\hat{\boldsymbol{s}}_1, \ldots, \hat{\boldsymbol{s}}_L, \hat{\boldsymbol{f}}) = \arg\min_{\boldsymbol{s} \in \mathbb{C}^{n_\mathrm{p} \times L}} \arg\min_{\boldsymbol{f} \in \mathbb{C}^{n_\mathrm{p}}} \Psi(\boldsymbol{s}_1, \ldots, \boldsymbol{s}_L, \boldsymbol{f})$$

$$\Psi(\boldsymbol{s}_1, \ldots, \boldsymbol{s}_L, \boldsymbol{f}) \triangleq \sum_{l=1}^{L} \left[\left\| \boldsymbol{z}_l - \mathsf{diag}\{\boldsymbol{f}\} \, \boldsymbol{s}_l \right\|^2 + \mathsf{R}(\boldsymbol{s}_l) \right] + \mathsf{R}_0(\boldsymbol{f}), \tag{7.13.13}$$

e,mr,sensemap,kost,L

where $\mathsf{R}_0(\boldsymbol{f})$ is an optional regularizer for the object that can help control noise in areas where the object magnitude is small.

Again, a natural approach to minimizing the cost function Ψ is to use **alternating minimization**, wherein we alternate between updating the estimate of the image $\boldsymbol{f}$ and then updating the estimates of the sensitivity maps $\{\boldsymbol{s}_l\}$, always descending the cost function. We can form initial estimates of the sensitivity maps either by using physical models of the coils, or by strongly smoothing each coil image. For given estimates of $\{\boldsymbol{s}_l\}$, the cost function is quadratic in $\boldsymbol{f}$ and is minimized easily to update $\boldsymbol{f}$. Likewise, given an updated estimate of $\boldsymbol{f}$, one can easily minimize Ψ to update each $\{\boldsymbol{s}_l\}$ as described above.

If it is found that the above procedure does not constraint $\boldsymbol{s}$ sufficiently, then one could add another penalty term to the cost function that encourages the sensitivity map estimates to satisfy constraints such as those in the literature, *e.g.*, the sum of the logarithms of the $\boldsymbol{s}_l$ maps should be zero or nearly so [180].

There are alternative methods described in the parallel imaging literature that avoid the use of a sensitivity image altogether, *e.g.*, [183].

7.13.2.5 Estimation from L k-space data sets

The approach in the previous section may work poorly if the k-space trajectories are under-sampled, because in such cases the individual images $\{\boldsymbol{z}_l\}$ will have large aliasing artifacts. For such situations, it may be more effective to estimate $\boldsymbol{s}_1, \ldots, \boldsymbol{s}_L$ and $\boldsymbol{f}$ directly from the k-space data. A natural cost function is

$$\Psi(\boldsymbol{s}, \boldsymbol{f}) = \sum_{l=1}^{L} \left[\|\boldsymbol{y}_l - \boldsymbol{A} \,\mathsf{diag}\{\boldsymbol{s}_l\} \, \boldsymbol{f}\|^2 + \mathsf{R}(\boldsymbol{s}_l) \right]^2 + \mathsf{R}_0(\boldsymbol{f}), \tag{7.13.14}$$

e,mr,sensemap,kspace

where $\boldsymbol{y}_l$ denotes the k-space data for the lth array coil, and $\boldsymbol{A}$ denotes the encoding/system matrix that includes the k-space trajectory and perhaps field inhomogeneity effects, but does not include the coil sensitivity effects because those are modeled by the $\mathsf{diag}\{\boldsymbol{s}_l\}$ term. One can alternate between updating each $\boldsymbol{s}_l$ for fixed $\boldsymbol{f}$ and then updating $\boldsymbol{f}$ for fixed $\boldsymbol{s}$ using the usual CG algorithm.

A problem with (7.13.14) is that one can multiply the image $\boldsymbol{f}$ by a factor and divide each $\boldsymbol{s}_l$ map by that same factor and the data-fit term is unchanged, so the problem is essentially not identifiable. A more reasonable approach may be to minimize Ψ subject to an equality constraint on the sum of the image values to fix the "scale" of the image relative to some reference. Mathematically this can be expressed as the constraint $\mathbf{1}'\boldsymbol{f} = c$ for some constant c. To solve this constrained problem we use the Lagrange multiplier approach, in which we must minimize the augmented cost function

$$\Psi(\boldsymbol{s}_1, \ldots, \boldsymbol{s}_L, \boldsymbol{f}) + \lambda \left(\mathbf{1}'\boldsymbol{f} - c\right).$$

This changes only the update formulas for $\boldsymbol{f}$. Setting the gradient w.r.t. $\boldsymbol{f}$ to zero yields

$$\begin{aligned}
\hat{\boldsymbol{f}}_\lambda &= \hat{\boldsymbol{f}}_0 - \lambda \boldsymbol{u} \\
\hat{\boldsymbol{f}}_0 &= \left[\boldsymbol{A}'\boldsymbol{A} + \boldsymbol{C}'\boldsymbol{C}\right]^{-1} \boldsymbol{A}'\boldsymbol{y} \\
\boldsymbol{u} &= \left[\boldsymbol{A}'\boldsymbol{A} + \boldsymbol{C}'\boldsymbol{C}\right]^{-1} \mathbf{1},
\end{aligned}$$

where $\boldsymbol{A} \triangleq \begin{bmatrix} \boldsymbol{A}\,\mathsf{diag}\{\boldsymbol{s}_1\} \\ \vdots \\ \boldsymbol{A}\,\mathsf{diag}\{\boldsymbol{s}_L\} \end{bmatrix}$ and $\boldsymbol{C}$ and $\boldsymbol{y}$ are defined similarly. Satisfying the constraint requires

$$\hat{\lambda} = \frac{\mathbf{1}'\hat{\boldsymbol{f}}_0 - c}{\mathbf{1}'\boldsymbol{u}}.$$

So the final estimator $\hat{\boldsymbol{f}}_{\hat{\lambda}}$ requires two runs of the iterative CG algorithm to form $\hat{\boldsymbol{f}}_0$ and $\boldsymbol{u}$.

An alternative approach would be to constrain the sensitivity maps. Note that we can rewrite data-fit term as

$$\|\boldsymbol{y}_l - \boldsymbol{A}\,\mathsf{diag}\{s_{lj} / d_j\} \, (\boldsymbol{D}\boldsymbol{f})\|^2$$

for any diagonal matrix $\boldsymbol{D} = \mathsf{diag}\{d_j\}$. A natural choice is $d_j = \sqrt{\sum_{l=1}^{L} \left|s_{lj}^{(0)}\right|^2}$, where $s_{lj}^{(0)}$ is an initial estimate of the sensitivity maps. Then we could minimize $\Psi(\boldsymbol{s}, \boldsymbol{f})$ subject to the quadratic constraint $d_j^2 = \sum_{l=1}^{L} \left|s_{lj}^{(0)}\right|^2$. Comparing these methods is an *open problem*.

7.13.3 Simulation results

We simulated coil sensitivity patterns using the formula derived in [184] for four circular coils of radius 10cm, as shown in Fig. 7.13.1. Using a brain image from BrainWeb [185], we simulated noisy array coil scans $\{\boldsymbol{z}_l\}$ as shown in Fig. 7.13.2, as well as a body coil scan (not shown) having uniform RF sensitivity.

Fig. 7.13.3 shows the conventional sensitivity map estimates based on (7.13.3). There was considerable noise anywhere the signal magnitudes were small, including within the ventricles. To reduce this noise, we first computed the median of all s_{lj} estimates within voxels where $|z_{lj}|$ was above 5% of the maximum z_{lj} value. Then, anywhere $|z_{lj}|$ was below 5% of the maximum z_{lj} value, we replaced the corresponding s_{lj} estimate that median value. Fig. 7.13.4 shows the regularized sensitivity map estimates based on (7.13.8). The regularization controls the noise. Fig. 7.13.5 shows the error images for both the conventional and regularized estimates. The regularized method has reduced error within the head interior relative to the conventional ratio estimates.

MIRT *See* `mri_sensemap1.m`.

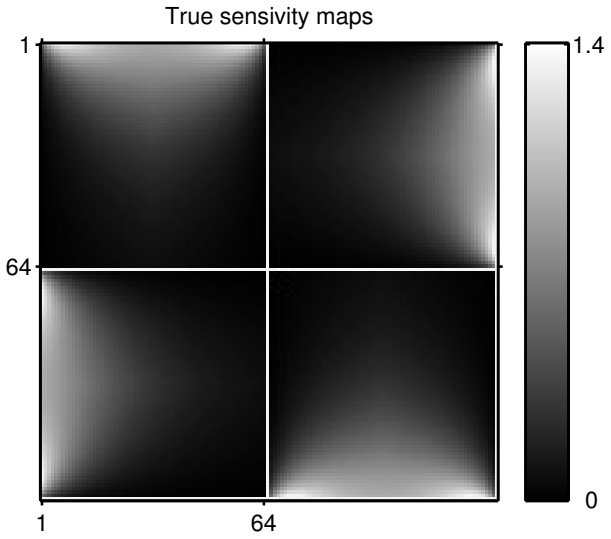

Figure 7.13.1: True sensitivity maps $\{s_l\}$ used in simulations. fig_m

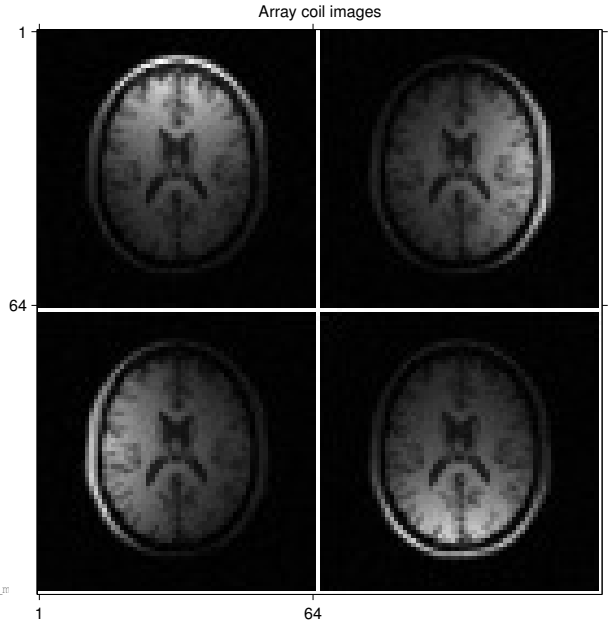

Figure 7.13.2: Noisy brain images $\{z_l\}$ with RF coil sensitivity effects. fig_mr_sensemap1_zl

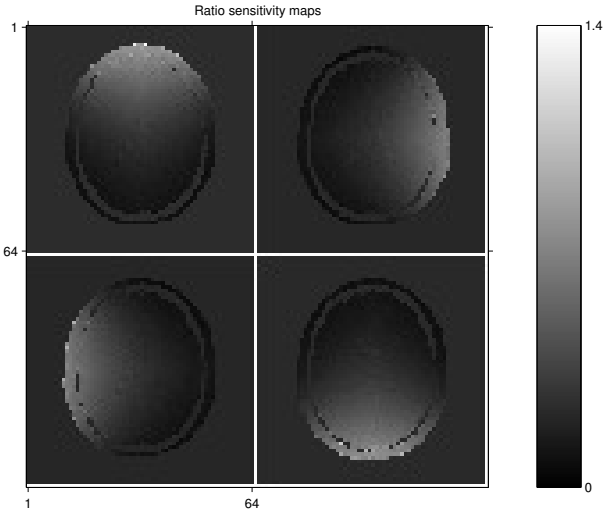

Figure 7.13.3: Conventional sensitivity map estimates based on (7.13.3). fig_mr_sensemap1_ratio

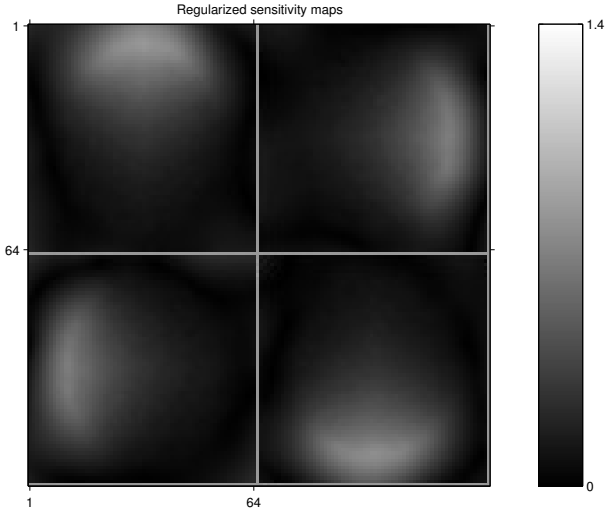

Figure 7.13.4: Regularized sensitivity map estimates based on (7.13.8). fig_mr_sensemap1_reg

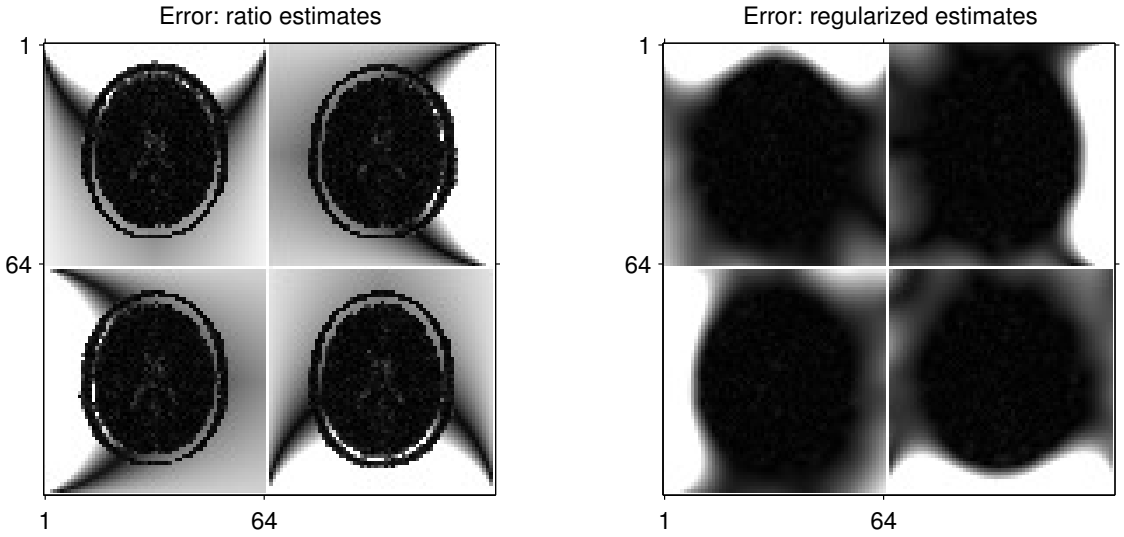

Figure 7.13.5: Error images for the estimates shown in Fig. 7.13.3 and Fig. 7.13.4, with gray scale display range from 0 to 0.25. fig_mr_sensemap1_err

7.14 Problems (s,mr,prob)

s,mr,prob

Problem 7.1 *In the presence of field inhomogeneity, determine whether the following estimators are invariant to a time-shift of the form $t_i \mapsto t_i + \tau$ in both the model and the estimator: (i) the conjugate phase method, (ii) unregularized least-squares, (iii) regularized least-squares with $\mathsf{R}(\boldsymbol{x}) = \|\boldsymbol{x}\|^2$, and (iii) regularized least-squares with a roughness penalty.*

7.15 Bibliography

kaiser:74:daf [1] R. Kaiser, E. Bartholdi, and R. R. Ernst. "Diffusion and field-gradient effects in NMR Fourier spectroscopy." In: *J. Chem. Phys.* 60.8 (Apr. 1974), 2966–79. DOI: 10.1063/1.1681477.

wu:90:eod [2] E. X. Wu and R. B. Buxton. "Effect of diffusion on the steady-state magnetization with pulsed field gradients." In: *J. Mag. Res.* 90.2 (Nov. 1990), 243–53. DOI: '10.1016/0022-2364(90)90131-R'.

carney:91:asa [3] C. E. Carney, S. T. S. Wong, and S. Patz. "Analytical solution and verification of diffusion effect in SSFP." In: *Mag. Res. Med.* 19.2 (June 1991), 240–6. DOI: 10.1002/mrm.1910190209.

le:13:aev [4] M. Le, S. Ramani, and J. A. Fessler. "An efficient variable splitting based algorithm for regularized SENSE reconstruction with support constraint." In: *Proc. Intl. Soc. Mag. Res. Med.* 2013, p. 2654. URL: http://archive.ismrm.org/year/2654.html.

quarteroni:07 [5] A. Quarteroni, R. Sacco, and F. Saler. *Numerical mathematics*. Springer, 2007. DOI: 10.1007/b98885.

bevilacqua:88:pso [6] R. Bevilacqua, B. Codenotti, and F. Romani. "Parallel solution of block tridiagonal linear systems." In: *Linear Algebra and its Applications* 104 (June 1988), 39–57. DOI: 10.1016/0024-3795(88)90305-9.

storath:14:fpo [7] M. Storath and A. Weinmann. "Fast partitioning of vector-valued images." In: *SIAM J. Imaging Sci.* 7.3 (2014), 1826–52. DOI: 10.1137/130950367.

ramani:11:pmi [8] S. Ramani and J. A. Fessler. "Parallel MR image reconstruction using augmented Lagrangian methods." In: *IEEE Trans. Med. Imag.* 30.3 (Mar. 2011), 694–706. DOI: 10.1109/TMI.2010.2093536.

seal:13:rpc [9] S. K. Seal, K. S. Perumalla, and S. P. Hirshman. "Revisiting parallel cyclic reduction and parallel prefix-based algorithms for block tridiagonal systems of equations." In: *J. of Parallel and Distributed Computing* 73.2 (2013), 273–80. DOI: 10.1016/j.jpdc.2012.10.003.

sameh:78:osp [10] A. H. Sameh and D. J. Kuck. "On stable parallel linear system solvers." In: *J. Assoc. Comput. Mach.* 25.1 (Jan. 1978), 81–91. DOI: 10.1145/322047.322054.

kulkarni:99:eot
[11] D. Kulkarni, D. Schmidt, and S-K. Tsui. "Eigenvalues of tridiagonal pseudo-Toeplitz matrices." In: *Linear Algebra and its Applications* 297.1-3 (Aug. 1999), 63–80. DOI: 10.1016/S0024-3795(99)00114-7.

polizzi:06:aph
[12] E. Polizzi and A. H. Sameh. "A parallel hybrid banded system solver: the SPIKE algorithm." In: *Parallel Computing* 32.2 (2006), 177–94. DOI: 10.1016/j.parco.2005.07.005.

polizzi:07:sap
[13] E. Polizzi and A. H. Sameh. "SPIKE: A parallel environment for solving banded linear systems." In: *Computers & Fluids* 36 (2007), 113–41. DOI: 10.1016/j.compfluid.2005.07.005.

mikkelsen:08:aot
[14] C. C. K. Mikkelsen and M. Manguoglu. "Analysis of the truncated SPIKE algorithm." In: *SIAM J. Matrix. Anal. Appl.* 30.4 (2008), 1500–19. DOI: 10.1137/080719571.

manguoglu:09:pap
[15] M. Manguoglu, A. H. Sameh, and O. Schenk. *PSPIKE: A parallel hybrid sparse linear system solver*. LNCS 5704 797-808. 2009. DOI: 10.1007/978-3-642-03869-3_74.

allison:13:are
[16] M. J. Allison, S. Ramani, and J. A. Fessler. "Accelerated regularized estimation of MR coil sensitivities using augmented Lagrangian methods." In: *IEEE Trans. Med. Imag.* 32.3 (Mar. 2013), 556–64. DOI: 10.1109/TMI.2012.2229711 (cit. on p. 7.42).

ghadimi:12:oto
[17] E. Ghadimi et al. "On the optimal step-size selection for the alternating direction method of multipliers." In: *Proc. IFAC Work. on Estimation and Control in Networked Systems* 45.26 (Sept. 2012), 139–4. DOI: 10.3182/20120914-2-US-4030.00038.

ghadimi:15:ops
[18] E. Ghadimi et al. "Optimal parameter selection for the alternating direction method of multipliers (ADMM): quadratic problems." In: *IEEE Trans. Auto. Control* 60.3 (Mar. 2015), 644–58. DOI: 10.1109/TAC.2014.2354892.

eckstein:92:otd
[19] J. Eckstein and D. P. Bertsekas. "On the Douglas-Rachford splitting method and the proximal point algorithm for maximal monotone operators." In: *Mathematical Programming* 55.1-3 (Apr. 1992), 293–318. DOI: 10.1007/BF01581204.

eckstein:94:pad
[20] J. Eckstein. "Parallel alternating direction multiplier decomposition of convex programs." In: *J. Optim. Theory Appl.* 80.1 (Jan. 1994), 39–62. DOI: 10.1007/BF02196592.

ramani:11:rpm
[21] S. Ramani and J. A. Fessler. "Regularized parallel MRI reconstruction using an alternating direction method of multipliers." In: *Proc. IEEE Intl. Symp. Biomed. Imag.* 2011, 385–8. DOI: 10.1109/ISBI.2011.5872429.

goldstein:09:tsb
[22] T. Goldstein and S. Osher. "The split Bregman method for L1-regularized problems." In: *SIAM J. Imaging Sci.* 2.2 (2009), 323–43. DOI: 10.1137/080725891.

allison:12:aco
[23] M. J. Allison and J. A. Fessler. "Accelerated computation of regularized field map estimates." In: *Proc. Intl. Soc. Mag. Res. Med.* 2012, p. 0413. URL: http://cds.ismrm.org/protected/12MProceedings/files/0413.pdf.

chan:89:teb
[24] R. Chan and G. Strang. "Toeplitz equations by conjugate gradients with circulant preconditioner." In: *SIAM J. Sci. Stat. Comp.* 10.1 (1989), 104–19. DOI: 10.1137/0910009.

chan:93:fbp
[25] R. H. Chan, J. G. Nagy, and R. J. Plemmons. "FFT-based preconditioners for Toeplitz-block least-squares problems." In: *SIAM J. Numer. Anal.* 30.6 (Dec. 1993), 1740–68. DOI: 10.1137/0730089.

chan:94:cpf
[26] T. F. Chan and J. A. Olkin. "Circulant preconditioners for Toeplitz-block matrices." In: *Numer. Algorithms* 6.1 (Mar. 1994), 89–101. DOI: 10.1007/BF02149764.

chan:96:cgm
[27] R. H. Chan and M. K. Ng. "Conjugate gradient methods for Toeplitz systems." In: *SIAM Review* 38.3 (Sept. 1996), 427–82. DOI: 10.1137/S0036144594276474 (cit. on pp. 7.13, 7.14, 7.15).

dembo:89:end
[28] A. Dembo, C. L. Mallows, and L. A. Shepp. "Embedding nonnegative definite Toeplitz matrices in nonnegative definite circulant matrices, with application to covariance estimation." In: *IEEE Trans. Info. Theory* 35.6 (Nov. 1989), 1206–12. DOI: 10.1109/18.45276.

dembo:88:bot
[29] A. Dembo. "Bounds on the extreme eigenvalues of positive-definite Toeplitz matrices." In: *IEEE Trans. Info. Theory* 34.2 (Mar. 1988), 352–5. DOI: 10.1109/18.2651.

ramani:13:ncm
[30] S. Ramani et al. "Non-Cartesian MRI reconstruction with automatic regularization via Monte-Carlo SURE." In: *IEEE Trans. Med. Imag.* 32.8 (Aug. 2013), 1411–22. DOI: 10.1109/TMI.2013.2257829.

goldfarb:13:fal
[31] D. Goldfarb, S. Ma, and K. Scheinberg. "Fast alternating linearization methods for minimizing the sum of two convex functions." In: *Mathematical Programming* 141.1-2 (Oct. 2013), 349–82. DOI: 10.1007/s10107-012-0530-2.

hinshaw:76:ifb
[32] W. S. Hinshaw. "Image formation by nuclear magnetic resonance: The sensitive point method." In: *J. Appl. Phys.* 47.8 (Aug. 1976), p. 3709. DOI: 10.1063/1.323136.

ernst:66:aof
[33] R. R. Ernst and W. A. Anderson. "Application of Fourier transform spectroscopy to magnetic resonance." In: *Rev. Sci. Instrum.* 37.1 (Jan. 1966), 93–102. DOI: 10.1063/1.1719961.

bruder:88:ans
[34] H. Bruder et al. "A new steady-state imaging sequence for simultaneous acquisition of two MR images with clearly different contrasts." In: *Mag. Res. Med.* 7.1 (May 1988), 35–42. DOI: 10.1002/mrm.1910070105.

ruehm:98:mop
[35] S. Ruehm et al. "MRI of patellar articular cartilage: Evaluation of an optimized gradient-echo sequence (3D-DESS)." In: *J. Mag. Res. Im.* 8.6 (Nov. 1998), 1246–51. DOI: 10.1002/jmri.1880080611.

staroswiecki:12:seo
[36] E. Staroswiecki et al. "Simultaneous estimation of T2 and apparent diffusion coefficient in human articular cartilage in vivo with a modified three-dimensional double echo steady state (DESS) sequence at 3 T." In: *Mag. Res. Med.* 67.4 (2012), 1086–96. DOI: 10.1002/mrm.23090.

heule:13:tes
[37] R. Heule, C. Ganter, and O. Bieri. "Triple echo steady state (TESS) relaxometry." In: *Proc. Intl. Soc. Mag. Res. Med.* 2013, p. 467. URL: http://archive.ismrm.org/year/467.html.

gyngell:89:tss
[38] M. L. Gyngell. "The steady-state signals in short-repetition-time sequences." In: *J. Mag. Res.* 81.3 (Feb. 1989), 474–83. DOI: 10.1016/0022-2364(89)90083-8.

nielsen:13:stf
[39] J-F. Nielsen, D. Yoon, and D. C. Noll. "Small-tip fast recovery imaging using non-slice-selective tailored tip-up pulses and radiofrequency-spoiling." In: *Mag. Res. Med.* 69.3 (Mar. 2013), 657–66. DOI: 10.1002/mrm.24289.

sun:12:ado
[40] H. Sun, J. A. Fessler, and J. F. Nielsen. "Analytic description of steady-state imaging with dual RF pulses and gradient spoiling." In: *Proc. Intl. Soc. Mag. Res. Med.* 2012, p. 4183. URL: http://cds.ismrm.org/protected/12MProceedings/files/4183.pdf.

bieri:09:ssw
[41] O. Bieri and K. Scheffler. "SSFP signal with finite RF pulses." In: *Mag. Res. Med.* 62.5 (Nov. 2009), 1232–41. DOI: 10.1002/mrm.22116.

shinnar:89:tao
[42] M. Shinnar and J. S. Leigh. "The application of spinors to pulse synthesis and analysis." In: *Mag. Res. Med.* 12.1 (Oct. 1989), 93–8. DOI: 10.1002/mrm.1910120112.

pauly:91:prf
[43] J. Pauly et al. "Parameter relations for the Shinnar-Le Roux selective excitation pulse design algorithm." In: *IEEE Trans. Med. Imag.* 10.1 (Mar. 1991), 53–65. DOI: 10.1109/42.75611.

sebastiani:91:mpo
[44] G. Sebastiani and P. Barone. "Mathematical principles of basic magnetic resonance imaging in medicine." In: *Signal Processing* 25.2 (Nov. 1991), 227–50. DOI: 10.1016/0165-1684(91)90065-Q (cit. on p. 7.3).

liang:00
[45] Z-P. Liang and P. C. Lauterber. *Principles of magnetic resonance imaging*. New York: IEEE, 2000 (cit. on p. 7.3).

sacolick:10:bmb
[46] L. I. Sacolick et al. "B1 mapping by Bloch-Siegert shift." In: *Mag. Res. Med.* 63.5 (May 2010), 1315–22. DOI: 10.1002/mrm.22357.

funai:08:rfm
[47] A. K. Funai et al. "Regularized field map estimation in MRI." In: *IEEE Trans. Med. Imag.* 27.10 (Oct. 2008), 1484–94. DOI: 10.1109/TMI.2008.923956 (cit. on p. 7.27).

huber:81
[48] P. J. Huber. *Robust statistics*. New York: Wiley, 1981.

erdogan:99:maf
[49] H. Erdogan and J. A. Fessler. "Monotonic algorithms for transmission tomography." In: *IEEE Trans. Med. Imag.* 18.9 (Sept. 1999), 801–14. DOI: 10.1109/42.802758 (cit. on p. 7.29).

doneva:10:csf
[50] M. Doneva et al. "Compressed sensing for chemical shift-based water-fat separation." In: *Mag. Res. Med.* 64.6 (Dec. 2010), 1749–59. DOI: 10.1002/mrm.22563.

wiens:12:aca
[51] C. N. Wiens, C. M. McCurdy, and C. A. McKenzie. "A combined approach to compressed sensing and parallel imaging for fat-water separation with R2* estimation." In: *Proc. Intl. Soc. Mag. Res. Med.* 2012, p. 7. URL: http://cds.ismrm.org/protected/12MProceedings/files/0007.pdf.

waldspurger:16:prw
[52] I. Waldspurger. *Phase retrieval with random Gaussian sensing vectors by alternating projections*. 2016. URL: http://arxiv.org/abs/1609.03088.

sun:13:spd
[53] H. Sun et al. "Spoke pulse design in magnetic resonance imaging using greedy minimax algorithm." In: *Proc. IEEE Intl. Symp. Biomed. Imag.* 2013, 696–9. DOI: 10.1109/ISBI.2013.6556570.

yip:05:irp
[54] C. Yip, J. A. Fessler, and D. C. Noll. "Iterative RF pulse design for multidimensional, small-tip-angle selective excitation." In: *Mag. Res. Med.* 54.4 (Oct. 2005), 908–17. DOI: 10.1002/mrm.20631.

beck:09:fgb
[55] A. Beck and M. Teboulle. "Fast gradient-based algorithms for constrained total variation image denoising and deblurring problems." In: *IEEE Trans. Im. Proc.* 18.11 (Nov. 2009), 2419–34. DOI: 10.1109/TIP.2009.2028250.

kim:15:aof
[56] D. Kim and J. A. Fessler. "An optimized first-order method for image restoration." In: *Proc. IEEE Intl. Conf. on Image Processing*. 2015, 3675–9. DOI: 10.1109/ICIP.2015.7351490.

setsompop:08:mls
[57] K. Setsompop et al. "Magnitude least squares optimization for parallel radio frequency excitation design demonstrated at 7 Tesla with eight channels." In: *Mag. Res. Med.* 59.4 (Apr. 2008), 908–15. DOI: 10.1002/mrm.21513.

hoyosidrobo:14:ovs
[58] A. Hoyos-Idrobo et al. "On variant strategies to solve the magnitude least squares optimization problem in parallel transmission pulse design and under strict SAR and power constraints." In: *IEEE Trans. Med. Imag.* 33.3 (Mar. 2014), 739–48. DOI: 10.1109/TMI.2013.2295465.

sutton:03:fii
[59] B. P. Sutton, D. C. Noll, and J. A. Fessler. "Fast, iterative image reconstruction for MRI in the presence of field inhomogeneities." In: *IEEE Trans. Med. Imag.* 22.2 (Feb. 2003), 178–88. DOI: 10.1109/TMI.2002.808360 (cit. on pp. 7.3, 7.4, 7.5, 7.6, 7.7, 7.8, 7.14, 7.15, 7.19, 7.20).

sutton:01:seo
[60] B. P. Sutton, D. Noll, and J. A. Fessler. "Simultaneous estimation of image and inhomogeneity field map." In: *ISMRM Minimum Data Acquisition Workshop*. 2001, 15–8. URL: abs/01/sutton-01-seo.pdf (cit. on p. 7.3).

sutton:02:fci
[61] B. P. Sutton, J. A. Fessler, and D. C. Noll. "Field-corrected imaging using joint estimation of image and field map." In: *Proc. Intl. Soc. Mag. Res. Med.* 2002, p. 737. URL: http://cds.ismrm.org/ismrm-2002/PDF3/0737.PDF (cit. on p. 7.3).

sutton:04:dfm
[62] B. P. Sutton, D. C. Noll, and J. A. Fessler. "Dynamic field map estimation using a spiral-in / spiral-out acquisition." In: *Mag. Res. Med.* 51.6 (June 2004), 1194–204. DOI: 10.1002/mrm.20079 (cit. on pp. 7.3, 7.27).

lee:02:eor
[63] S. Lee et al. "Estimation of R_2^* using extended rosette acquisition." In: *Hum. Brain Map.* In NeuroImage 16(2 S1):151-2, 2002. 2002, 151–2. DOI: '10.1016/S1053-8119(02)90010-8' (cit. on p. 7.3).

olafsson:03:naf
[64] V. T. Olafsson, D. C. Noll, and J. A. Fessler. "New approach for estimating ΔR_2^* in fMRI." In: *Proc. Intl. Soc. Mag. Res. Med.* 2003, p. 132. URL: http://dev.ismrm.org//2003/0132.html (cit. on p. 7.3).

lee:02:ase
[65] S. Lee, J. A. Fessler, and D. Noll. "A simultaneous estimation of field inhomogeneity and R2* maps using extended rosette trajectory." In: *Proc. Intl. Soc. Mag. Res. Med.* 2002, p. 2327. URL: http://cds.ismrm.org/ismrm-2002/PDF8/2327.PDF (cit. on p. 7.3).

sutton:02:seo
[66] B. P. Sutton et al. "Simultaneous estimation of I_0, R_2^*, and field map using a multi-echo spiral acquisition." In: *Proc. Intl. Soc. Mag. Res. Med.* 2002, p. 1323. URL: http://cds.ismrm.org/ismrm-2002/PDF5/1323.PDF (cit. on p. 7.3).

peltier:02:seo
[67] S. J. Peltier et al. "Simultaneous estimation of I_0, R_2^*, and field map using a multi-echo spiral acquisition." In: *Hum. Brain Map.* In NeuroImage 16(2 S1):95-6, 2002. 2002, 95–6. DOI: '10.1016/S1053-8119(02)90010-8' (cit. on p. 7.3).

lee:04:era
[68] S. Lee, D. Noll, and J. A. Fessler. "EXTended Rosette ACquisition Technique (EXTRACT): a dynamic R2* mapping method using extended rosette trajectory." In: *Proc. Intl. Soc. Mag. Res. Med.* 2004, p. 2128. URL: http://cds.ismrm.org/ismrm-2004/Files/002128.pdf (cit. on pp. 7.3, 7.30).

olafsson:04:duo
[69] V. Olafsson, J. A. Fessler, and D. C. Noll. "Dynamic update of R2* and field map in fMRI." In: *Proc. Intl. Soc. Mag. Res. Med.* 2004, p. 45. URL: http://cds.ismrm.org/ismrm-2004/Files/000045.pdf (cit. on pp. 7.3, 7.27, 7.30).

sutton:01:imi
[70] B. P. Sutton, J. A. Fessler, and D. Noll. "Iterative MR image reconstruction using sensitivity and inhomogeneity field maps." In: *Proc. Intl. Soc. Mag. Res. Med.* 2001, p. 771. URL: http://cds.ismrm.org/ismrm-2001/PDF3/0771.pdf (cit. on p. 7.3).

sumanaweera:93:msm
[71] T. S. Sumanaweera et al. "MR susceptibility misregistration correction." In: *IEEE Trans. Med. Imag.* 12.2 (June 1993), 251–9. DOI: 10.1109/42.232253 (cit. on p. 7.3).

sumanaweera:95:mgd
[72] T. S. Sumanaweera et al. "MR geometric distortion correction for improved frame-based stereotaxic target localization accuracy." In: *Mag. Res. Med.* 34.1 (July 1995), 106–13. DOI: 10.1002/mrm.1910340116 (cit. on p. 7.3).

sutton:04:cfw [73] B. P. Sutton, D. C. Noll, and J. A. Fessler. "Compensating for within-voxel susceptibility gradients in BOLD fMRI." In: *Proc. Intl. Soc. Mag. Res. Med.* 2004, p. 349. URL: http://cds.ismrm.org/ismrm-2004/Files/000349.pdf (cit. on p. 7.3).

sutton:03:phd [74] B. P. Sutton. "Physics-based reconstruction for MRI: Compensating and estimating field inhomogeneity and T_2^* relaxation." PhD thesis. Ann Arbor, MI: Univ. of Michigan, Ann Arbor, MI, 48109-2122, 2003. URL: https://hdl.handle.net/2027.42/123963 (cit. on p. 7.3).

fessler:03:nff [75] J. A. Fessler and B. P. Sutton. "Nonuniform fast Fourier transforms using min-max interpolation." In: *IEEE Trans. Sig. Proc.* 51.2 (Feb. 2003), 560–74. DOI: 10.1109/TSP.2002.807005 (cit. on pp. 7.4, 7.6, 7.14).

noll:91:ahc [76] D. C. Noll et al. "A homogeneity correction method for magnetic resonance imaging with time-varying gradients." In: *IEEE Trans. Med. Imag.* 10.4 (Dec. 1991), 629–37. DOI: 10.1109/42.108599 (cit. on pp. 7.4, 7.5, 7.15).

pan:05:fhm [77] R. Pan and S. J. Reeves. "Fast Huber-Markov edge-preserving image restoration." In: *Proc. SPIE 5674 Computational Imaging III*. 2005, 138–46. DOI: 10.1117/12.587823 (cit. on p. 7.4).

pan:06:ehm [78] R. Pan and S. J. Reeves. "Efficient Huber-Markov edge-preserving image restoration." In: *IEEE Trans. Im. Proc.* 15.12 (Dec. 2006), 3728–35. DOI: 10.1109/TIP.2006.881971 (cit. on p. 7.4).

noll:91:rtf [79] D. C. Noll. "Reconstruction techniques for magnetic resonance imaging." PhD thesis. CA: Stanford, 1991 (cit. on p. 7.5).

irarrazabal:96:icu [80] P. Irarrazabal et al. "Inhomogeneity correction using an estimated linear field map." In: *Mag. Res. Med.* 35.2 (Feb. 1996), 278–82. DOI: 10.1002/mrm.1910350221 (cit. on pp. 7.5, 7.23).

man:97:mif [81] L-C. Man, J. M. Pauly, and A. Macovski. "Multifrequency interpolation for fast off-resonance correction." In: *Mag. Res. Med.* 37.5 (May 1997), 785–92. DOI: 10.1002/mrm.1910370523 (cit. on pp. 7.5, 7.6, 7.8).

moriguchi:03:bro [82] H. Moriguchi et al. "Block regional off-resonance correction (BRORC): A fast and effective deblurring method for spiral imaging." In: *Mag. Res. Med.* 50.3 (Sept. 2003), 643–8. DOI: 10.1002/mrm.10570 (cit. on p. 7.5).

gersho:79:aob [83] A. Gersho. "Asymptotically optimal block quantization." In: *IEEE Trans. Info. Theory* 25.4 (July 1979), 373–80. DOI: 10.1109/TIT.1979.1056067 (cit. on p. 7.5).

nieslony:03:afo [84] A. Nieslony and G. Steidl. "Approximate factorizations of Fourier matrices with nonequispaced knots." In: *Linear Algebra and its Applications* 366 (June 2003), 337–51. DOI: 10.1016/S0024-3795(02)00496-2 (cit. on p. 7.8).

lee:05:tt3 [85] J-Y. Lee and L. Greengard. "The type 3 nonuniform FFT and its applications." In: *J. Comp. Phys.* 206.1 (June 2005), 1–5. DOI: 10.1016/j.jcp.2004.12.004 (cit. on p. 7.8).

eggers:07:fic [86] H. Eggers, T. Knopp, and D. Potts. "Field inhomogeneity correction based on gridding reconstruction for magnetic resonance imaging." In: *IEEE Trans. Med. Imag.* 26.3 (Mar. 2007), 374–84. DOI: 10.1109/TMI.2006.891502 (cit. on p. 7.8).

noll:05:cpm [87] D. C. Noll, J. A. Fessler, and B. P. Sutton. "Conjugate phase MRI reconstruction with spatially variant sample density correction." In: *IEEE Trans. Med. Imag.* 24.3 (Mar. 2005), 325–36. DOI: 10.1109/TMI.2004.842452 (cit. on pp. 7.8, 7.19).

wajer:01:mso [88] F. Wajer and K. P. Pruessmann. "Major speedup of reconstruction for sensitivity encoding with arbitrary trajectories." In: *Proc. Intl. Soc. Mag. Res. Med.* 2001, p. 767. URL: http://cds.ismrm.org/ismrm-2001/PDF3/0767.pdf (cit. on p. 7.13).

eggers:02:cog [89] H. Eggers, P. Boernert, and P. Boesiger. "Comparison of gridding- and convolution-based iterative reconstruction algorithms for sensitivity-encoded non-cartesian acquisitions." In: *Proc. Intl. Soc. Mag. Res. Med.* 2002, p. 743. URL: http://cds.ismrm.org/ismrm-2002/PDF3/0743.PDF (cit. on p. 7.13).

fessler:99:cgp [90] J. A. Fessler and S. D. Booth. "Conjugate-gradient preconditioning methods for shift-variant PET image reconstruction." In: *IEEE Trans. Im. Proc.* 8.5 (May 1999), 688–99. DOI: 10.1109/83.760336 (cit. on pp. 7.15, 7.23).

koolstra::acs [91] K. Koolstra et al. "Accelerating compressed sensing in parallel imaging reconstructions using an efficient circulant preconditioner for Cartesian trajectories." In: *Mag. Res. Med.* (2018). DOI: 10.1002/mrm.27371 (cit. on p. 7.15).

schomberg:95:tgm
[92] H. Schomberg and J. Timmer. "The gridding method for image reconstruction by Fourier transformation." In: *IEEE Trans. Med. Imag.* 14.3 (Sept. 1995), 596–607. DOI: 10.1109/42.414625 (cit. on p. 7.15).

dahnke:08:sgm
[93] H. Dahnke et al. "Susceptibility gradient mapping (SGM): A new postprocessing method for positive contrast generation applied to superparamagnetic iron oxide particle (SPIO)-labeled cells." In: *Mag. Res. Med.* 60.3 (Sept. 2008), 595–603. DOI: 10.1002/mrm.21478 (cit. on p. 7.19).

fessler:05:tbi
[94] J. A. Fessler et al. "Toeplitz-based iterative image reconstruction for MRI with correction for magnetic field inhomogeneity." In: *IEEE Trans. Sig. Proc.* 53.9 (Sept. 2005), 3393–402. DOI: 10.1109/TSP.2005.853152 (cit. on pp. 7.19, 7.20).

fessler:06:rfe
[95] J. A. Fessler, D. Yeo, and D. C. Noll. "Regularized fieldmap estimation in MRI." In: *Proc. IEEE Intl. Symp. Biomed. Imag.* 2006, 706–9. DOI: 10.1109/ISBI.2006.1625014 (cit. on p. 7.20).

oster:92:tuo
[96] H. S. Oster and Y. Rudy. "The use of temporal information in the regularization of the inverse problem of electrocardiography." In: *IEEE Trans. Biomed. Engin.* 39.1 (Jan. 1992), 65–75. DOI: 10.1109/10.108129.

brooks:99:ieb
[97] D. H. Brooks et al. "Inverse electrocardiography by simultaneous imposition of multiple constraints." In: *IEEE Trans. Biomed. Engin.* 46.1 (Jan. 1999), 3–18. DOI: 10.1109/10.736746.

greensite:03:ttp
[98] F. Greensite. "The temporal prior in bioelectromagnetic source imaging problems." In: *IEEE Trans. Biomed. Engin.* 50.10 (Oct. 2003), 1152–9. DOI: 10.1109/TBME.2003.817632.

song:01:sao
[99] H. K. Song, L. Dougherty, and M. D. Schnall. "Simultaneous acquisition of multiple resolution images for dynamic contrast enhanced imaging of the breast." In: *Mag. Res. Med.* 46.3 (Sept. 2001), 503–9. DOI: 10.1002/mrm.1220.

song:04:dmw
[100] H. K. Song and L. Dougherty. "Dynamic MRI with projection reconstruction and KWIC processing for simultaneous high spatial and temporal resolution." In: *Mag. Res. Med.* 52.4 (Oct. 2004), 815–24. DOI: 10.1002/mrm.20237.

pipe:99:mcw
[101] J. G. Pipe. "Motion correction with PROPELLER MRI: Application to head motion and free-breathing cardiac imaging." In: *Mag. Res. Med.* 42.5 (Nov. 1999), 963–9. DOI: 10.1002/(SICI)1522-2594(199911)42:5<963::AID-MRM17>3.0.CO;2-L.

arfanakis:05:ksu
[102] K. Arfanakis et al. "K-space undersampling in PROPELLER imaging." In: *Mag. Res. Med.* 53.3 (Mar. 2005), 675–83. DOI: 10.1002/mrm.20380.

zhao:12:irf
[103] B. Zhao et al. "Image reconstruction from highly undersampled (k, t)-space data with joint partial separability and sparsity constraints." In: *IEEE Trans. Med. Imag.* 31.9 (Sept. 2012), 1809–20. DOI: 10.1109/TMI.2012.2203921.

candes:10:tpo
[104] E. J. Candes and T. Tao. "The power of convex relaxation: near-optimal matrix completion." In: *IEEE Trans. Info. Theory* 56.5 (May 2010), 2053–80. DOI: 10.1109/TIT.2010.2044061.

liang:94:aem
[105] Z-P. Liang and P. C. Lauterbur. "An efficient method for dynamic magnetic resonance imaging." In: *IEEE Trans. Med. Imag.* 13.4 (Dec. 1994), 677–86. DOI: 10.1109/42.363100.

liang:07:siw
[106] Z-P. Liang. "Spatiotemporal imaging with partially separable functions." In: *Proc. IEEE Intl. Symp. Biomed. Imag.* 2007, 988–91. DOI: 10.1109/ISBI.2007.357020.

haldar:09:rcs
[107] J. P. Haldar and D. Hernando. "Rank-constrained solutions to linear matrix equations using PowerFactorization." In: *IEEE Signal Proc. Letters* 16.7 (July 2009), 584–7. DOI: 10.1109/LSP.2009.2018223.

haldar:10:siw
[108] J. Haldar and Z-P. Liang. "Spatiotemporal imaging with partially separable functions: a matrix recovery approach." In: *Proc. IEEE Intl. Symp. Biomed. Imag.* 2010, 716–9. DOI: 10.1109/ISBI.2010.5490076.

zhao:10:lrm
[109] B. Zhao et al. "Low rank matrix recovery for real-time cardiac MRI." In: *Proc. IEEE Intl. Symp. Biomed. Imag.* 2010, 996–9. DOI: 10.1109/ISBI.2010.5490156.

hu:12:afm
[110] Y. Hu, S. Lingala, and M. Jacob. "A fast majorize minimize algorithm for the recovery of sparse and low-rank matrices." In: *IEEE Trans. Im. Proc.* 21.2 (Feb. 2012), 742–53. DOI: 10.1109/TIP.2011.2165552.

balzano:11:oia
[111] L. Balzano, R. Nowak, and B. Recht. *Online identification and tracking of subspaces from highly incomplete information*. 2011. URL: http://arxiv.org/abs/1006.4046.

lingala:12:abc
[112] S. G. Lingala and M. Jacob. "A blind compressive sensing framework for accelerated dynamic MRI." In: *Proc. IEEE Intl. Symp. Biomed. Imag.* 2012, 1060–3. DOI: 10.1109/ISBI.2012.6235741.

jain:12:lrm
[113] P. Jain, P. Netrapalli, and S. Sanghavi. *Low-rank matrix completion using alternating minimization*. 2012. URL: http://arxiv.org/abs/1212.0467.

garnier:95:mri
[114] S. J. Garnier et al. "Magnetic resonance image restoration." In: *J. Math. Im. Vision* 5.1 (Feb. 1995), 7–19. DOI: 10.1007/BF01250250 (cit. on p. 7.22).

bernstein:94:rop
[115] M. A. Bernstein et al. "Reconstructions of phase contrast, phased array multicoil data." In: *Mag. Res. Med.* 32.3 (Sept. 1994), 330–334. DOI: 10.1002/mrm.1910320308 (cit. on p. 7.22).

jacobson:07:aet
[116] M. W. Jacobson and J. A. Fessler. "An expanded theoretical treatment of iteration-dependent majorize-minimize algorithms." In: *IEEE Trans. Im. Proc.* 16.10 (Oct. 2007), 2411–22. DOI: 10.1109/TIP.2007.904387 (cit. on pp. 7.22, 7.33).

bamler:98:sar
[117] R. Bamler and P. Hartl. "Synthetic aperture radar interferometry." In: *Inverse Prob.* 14.4 (Aug. 1998), R1–. DOI: 10.1088/0266-5611/14/4/001 (cit. on p. 7.22).

fessler:94:pwl
[118] J. A. Fessler. "Penalized weighted least-squares image reconstruction for positron emission tomography." In: *IEEE Trans. Med. Imag.* 13.2 (June 1994), 290–300. DOI: 10.1109/42.293921 (cit. on p. 7.23).

xu:98:ssa
[119] C. Xu and J. L. Prince. "Snakes, shapes, and gradient vector flow." In: *IEEE Trans. Im. Proc.* 7.3 (Mar. 1998), 359–69. DOI: 10.1109/83.661186 (cit. on p. 7.23).

fessler:96:srp
[120] J. A. Fessler and W. L. Rogers. "Spatial resolution properties of penalized-likelihood image reconstruction methods: Space-invariant tomographs." In: *IEEE Trans. Im. Proc.* 5.9 (Sept. 1996), 1346–58. DOI: 10.1109/83.535846 (cit. on p. 7.25).

unser:91:rrf
[121] M. Unser, A. Aldroubi, and M. Eden. "Recursive regularization filters: design, properties, and applications." In: *IEEE Trans. Patt. Anal. Mach. Int.* 13.3 (Mar. 1991), 272–7. DOI: 10.1109/34.75514 (cit. on p. 7.25).

fessler:04:iir
[122] J. A. Fessler and D. C. Noll. "Iterative image reconstruction in MRI with separate magnitude and phase regularization." In: *Proc. IEEE Intl. Symp. Biomed. Imag.* 2004, 209–12. DOI: 10.1109/ISBI.2004.1398511 (cit. on pp. 7.27, 7.30).

roopchansingh:03:ssm
[123] V. Roopchansingh et al. "Single-shot magnetic field mapping embedded in echo-planar time-course imaging." In: *Mag. Res. Med.* 50.4 (Oct. 2003), 839–43. DOI: 10.1002/mrm.10587 (cit. on p. 7.27).

zibetti:10:sma
[124] M. V. W. Zibetti and A. R. D. Pierro. "Separate magnitude and phase regularization in MRI with incomplete data: preliminary results." In: *Proc. IEEE Intl. Symp. Biomed. Imag.* 2010, 0736–9. DOI: 10.1109/ISBI.2010.5490069 (cit. on p. 7.27).

zhao:12:sma
[125] F. Zhao et al. "Separate magnitude and phase regularization via compressed sensing." In: *IEEE Trans. Med. Imag.* 31.9 (Sept. 2012), 1713–23. DOI: 10.1109/TMI.2012.2196707 (cit. on p. 7.27).

zibetti:17:ics
[126] M. V. W. Zibetti and A. R. De Pierro. "Improving compressive sensing in MRI with separate magnitude and phase priors." In: *Multidimensional Systems and Signal Processing* 28.4 (Oct. 2017), 1109–31. DOI: 10.1007/s11045-016-0383-6 (cit. on p. 7.27).

lu:07:opd
[127] K. Lu, T. T. Liu, and M. Bydder. "Optimal phase difference reconstruction: comparison of two methods." In: *Mag. Res. Im.* 26.1 (Jan. 2007), 142–5. DOI: 10.1016/j.mri.2007.04.015 (cit. on p. 7.27).

reber:98:coo
[128] P. J. Reber et al. "Correction of off resonance-related distortion in echo-planar imaging using EPI-based field maps." In: *Mag. Res. Med.* 39.2 (Feb. 1998), 328–30. DOI: 10.1002/mrm.1910390223 (cit. on p. 7.27).

aksit:07:tpm
[129] P. Aksit, J. A. Derbyshire, and J. L. Prince. "Three-point method for fast and robust field mapping for EPI geometric distortion correction." In: *Proc. IEEE Intl. Symp. Biomed. Imag.* 2007, 141–4. DOI: 10.1109/ISBI.2007.356808 (cit. on p. 7.27).

mckenzie:99:fao
[130] C. A. McKenzie et al. "Fast acquisition of quantitative T2 maps." In: *Mag. Res. Med.* 41.1 (Jan. 1999), 208–12. DOI: 10.1002/(SICI)1522-2594(199901)41:1<208::AID-MRM30>3.0.CO;2-T (cit. on p. 7.28).

song:00:ksw
[131] H. K. Song and L. Dougherty. "K-space weighted image contrast (KWIC) for contrast manipulation in projection reconstruction MRI." In: *Mag. Res. Med.* 44.6 (Dec. 2000), 825–32. DOI: '10.1002/1522-2594(200012)44:6<825::AID-MRM2>3.0.CO;2-D' (cit. on p. 7.28).

altbach:05:por
[132] M. I. Altbach et al. "Processing of radial fast spin-echo data for obtaining T_2 estimates from a single k-space data set." In: *Mag. Res. Med.* 54.3 (Sept. 2005), 549–59. DOI: 10.1002/mrm.20611 (cit. on pp. 7.28, 7.30).

gensanne:05:app
[133] D. Gensanne et al. "A post-processing method for multiexponential spin-spin relaxation analysis of MRI signals." In: *Phys. Med. Biol.* 50.16 (Aug. 2005), 3755–72. DOI: 10.1088/0031-9155/50/16/007 (cit. on p. 7.28).

liu:99:cbf
[134] H-L. Liu et al. "Cerebral blood flow measurement by dynamic contrast MRI using singular value decomposition with an adaptive threshold." In: *Mag. Res. Med.* 42.1 (July 1999), 167–72. DOI: '10.1002/(SICI)1522-2594(199907)42:1<167::AID-MRM22>3.0.CO;2-Q' (cit. on p. 7.30).

akoka:93:rmo
[135] S. Akoka et al. "Radiofrequency map of an NMR coil by imaging." In: *Mag. Res. Im.* 11.3 (1993), 437–41. DOI: 10.1016/0730-725X(93)90078-R (cit. on p. 7.31).

wang:05:mac
[136] J. Wang et al. "Measurement and correction of transmitter and receiver induced nonuniformities in vivo." In: *Mag. Res. Med.* 53.2 (Feb. 2005), 408–17. DOI: 10.1002/mrm.20354 (cit. on p. 7.31).

wang:05:ivm
[137] J. Wang, M. Qiu, and R. T. Constable. "In vivo method for correcting transmit/receive nonuniformities with phased array coils." In: *Mag. Res. Med.* 53.3 (Mar. 2005), 666–74. DOI: 10.1002/mrm.20377 (cit. on p. 7.31).

callaghan:06:mcs
[138] M. F. Callaghan et al. "Measuring coil sensitivities of transmit and receive arrays with demonstration of RF shimming." In: *Proc. Intl. Soc. Mag. Res. Med.* 2006, p. 2627. URL: http://dev.ismrm.org//2006/2627.html (cit. on p. 7.31).

cunningham:06:sda
[139] C. H. Cunningham, J. M. Pauly, and K. S. Nayak. "Saturated double-angle method for rapid B_1+ mapping." In: *Mag. Res. Med.* 55.6 (June 2006), 1326–33. DOI: 10.1002/mrm.20896 (cit. on p. 7.31).

kerr:06:sct
[140] A. B. Kerr et al. "Self-calibrated transmit SENSE." In: *Proc. Intl. Soc. Mag. Res. Med.* 2006, p. 2561. URL: http://dev.ismrm.org//2006/2561.html (cit. on p. 7.31).

jin:96:coe
[141] J. M. Jin et al. "Computation of electromagnetic fields for high-frequency magnetic resonance imaging applications." In: *Phys. Med. Biol.* 41.12 (Dec. 1996), 2719–38. DOI: 10.1088/0031-9155/41/12/011 (cit. on p. 7.32).

alecci:01:rfm
[142] M. Alecci et al. "Radio frequency magnetic field mapping of a 3 Tesla birdcage coil: Experimental and theoretical dependence on sample properties." In: *Mag. Res. Med.* 46.2 (Aug. 2001), 379–85. DOI: 10.1002/mrm.1201 (cit. on p. 7.32).

bohning:88:moq
[143] D. Böhning and B. G. Lindsay. "Monotonicity of quadratic approximation algorithms." In: *Ann. Inst. Stat. Math.* 40.4 (Dec. 1988), 641–63. DOI: 10.1007/BF00049423 (cit. on p. 7.32).

wang:06:fif
[144] J. Wang et al. "Factors influencing flip angle mapping in MRI: RF pulse shape, slice-select gradients, off-resonance excitation, and B0 inhomogeneities." In: *Mag. Res. Med.* 56.2 (Aug. 2006), 463–68. DOI: 10.1002/mrm.20947.

tang:08:ana
[145] W. Tang, S. J. Reeves, and D. B. Twieg. "A new approach for joint estimation of magnitude, decay, and frequency from a single-shot MRI signal." In: *Proc. SPIE 6814 Computational Imaging VI*. 2008, p. 68140C. DOI: 10.1117/12.774013.

noll:94:moe
[146] D. C. Noll, J. M. Pauly, and A. Macovski. *Method of enhancing the focus of magnetic resonance images*. US Patent 5,311,132. 1994.

janzen:00:moc
[147] D. L. Janzen et al. *Method of correcting for magnetic field inhomogeneity in magnetic resonance imaging*. US Patent 6,150,815. 2000.

sumanaweera:94:maa
[148] T. S. Sumanaweera, G. H. Glover, and J. R. Adler. *Method and apparatus for correcting spatial distortion in magnetic resonance images due to magnetic field inhomogeneity including inhomogeneity due to susceptibility variations*. US Patent 5,351,006. 1994.

zhou:03:maa
[149] X. Zhou, J. K. Maier, and S. J. Huff. *Method and apparatus to reduce the effects of maxwell terms and other perturbation magnetic fields in MR images*. US Patent 6,528,998. 2003.

yoder:04:msw
[150] D. A. Yoder et al. "MRI simulator with object-specific field map calculations." In: *Mag. Res. Im.* 22.3 (Apr. 2004), 315–28. DOI: 10.1016/j.mri.2003.10.001.

barmet:04:eir
[151] C. Barmet, J. Tsao, and K. P. Pruessmann. "Efficient iterative reconstruction for MRI in strongly inhomogeneous B_0." In: *Proc. Intl. Soc. Mag. Res. Med.* 2004, p. 347. URL: http://cds.ismrm.org/ismrm-2004/Files/000347.pdf.

haselgrove:86:aaf
[152] J. Haselgrove and M. Prammer. "An algorithm for compensating of surface-coil images for sensitivity of the surface coil." In: *Mag. Res. Im.* 4.6 (1986), 469–72. DOI: 10.1016/0730-725X(86)90024-X (cit. on p. 7.38).

meyer:95:rco
[153] C. R. Meyer, P. H. Bland, and J. Pipe. "Retrospective correction of intensity inhomogeneities in MRI." In: *IEEE Trans. Med. Imag.* 14.1 (Mar. 1995), 36–41. DOI: 10.1109/42.370400 (cit. on p. 7.38).

brinkmann:98:ohu
[154] B. H. Brinkmann, A. Manduca, and R. A. Robb. "Optimized homorphic unsharp masking for MR grayscale inhomogeneity correction." In: *IEEE Trans. Med. Imag.* 17.2 (Apr. 1998), 161–71. DOI: 10.1109/42.700729 (cit. on p. 7.38).

sled:98:anm
[155] J. G. Sled, A. P. Zijdenbos, and A. C. Evans. "A nonparametric method for automatic correction of intensity nonuniformity in MRI data." In: *IEEE Trans. Med. Imag.* 17.1 (Feb. 1998), 87–97. DOI: 10.1109/42.668698 (cit. on p. 7.38).

lai:99:anv
[156] S-H. Lai and M. Fang. "A new variational shape-from-orientation approach to correcting intensity inhomogeneities in magnetic resonance images." In: *Med. Im. Anal.* 3.4 (Dec. 1999), 409–24. DOI: 10.1016/S1361-8415(99)80033-4 (cit. on p. 7.38).

styner:00:peo
[157] M. Styner et al. "Parametric estimate of intensity inhomogeneities applied to MRI." In: *IEEE Trans. Med. Imag.* 19.3 (Mar. 2000), 153–. DOI: 10.1109/42.845174 (cit. on p. 7.38).

luo:05:cob
[158] J. Luo et al. "Correction of bias field in MR images using singularity function analysis." In: *IEEE Trans. Med. Imag.* 24.8 (Aug. 2005), 1067–1085. DOI: 10.1109/TMI.2005.852066 (cit. on p. 7.38).

tustison:10:nin
[159] N. J. Tustison et al. "N4ITK: improved N3 bias correction." In: *IEEE Trans. Med. Imag.* 29.6 (June 2010), 1310–20. DOI: 10.1109/TMI.2010.2046908 (cit. on p. 7.38).

zhang:13:aea
[160] H. Zhang, X. Ye, and Y. Chen. "An efficient algorithm for multiphase image segmentation with intensity bias correction." In: *IEEE Trans. Im. Proc.* 22.10 (2013), 3842–51. DOI: 10.1109/TIP.2013.2262291 (cit. on p. 7.38).

ra:93:fiu
[161] J. B. Ra and C. Y. Rim. "Fast imaging using subencoding data sets from multiple detectors." In: *Mag. Res. Med.* 30.1 (July 1993), 142–5. DOI: 10.1002/mrm.1910300123 (cit. on pp. 7.38, 7.39).

pruessmann:99:sse
[162] K. P. Pruessmann et al. "SENSE: sensitivity encoding for fast MRI." In: *Mag. Res. Med.* 42.5 (Nov. 1999), 952–62. DOI: '10.1002/(SICI)1522-2594(199911)42:5<952::AID-MRM16>3.0.CO;2-S' (cit. on pp. 7.38, 7.39).

liang:09:asu
[163] D. Liang et al. "Accelerating SENSE using compressed sensing." In: *Mag. Res. Med.* 62.6 (Dec. 2009), 1574–84. DOI: 10.1002/mrm.22161 (cit. on p. 7.38).

bydder:07:oos
[164] M. Bydder, J. Perthen, and J. Du. "Optimization of sensitivity encoding with arbitrary k-space trajectories." In: *Mag. Res. Im.* 25.8 (Oct. 2007), 1123–9. DOI: 10.1016/j.mri.2007.01.003 (cit. on p. 7.38).

liu:08:gfm
[165] B. Liu et al. "G-factor maps of conjugate gradient SENSE reconstruction." In: *Proc. Intl. Soc. Mag. Res. Med.* 2008, p. 1285. URL: http://cds.ismrm.org/ismrm-2008/files/01285.pdf.

setsompop:11:wca
[166] K. Setsompop et al. "Wave-CAIPIRHINA: a method for reducing g-factors in highly accelerated 3D acquisitions." In: *Proc. Intl. Soc. Mag. Res. Med.* 2011, p. 478.

setsompop:10:bcf
[167] K. Setsompop et al. "Blipped CAIPIRHINA for simultaneous multi-slice EPI with reduced G-factor penalty." In: *Proc. Intl. Soc. Mag. Res. Med.* 2010, p. 551. URL: http://archive.ismrm.org/2010/0551.html.

setsompop:12:bca
[168] K. Setsompop et al. "Blipped-controlled aliasing in parallel imaging for simultaneous multislice echo planar imaging with reduced g-factor penalty." In: *Mag. Res. Med.* 67.5 (May 2012), 1210–24. DOI: 10.1002/mrm.23097.

raj:07:aml
[169] A. Raj, Y. Wang, and R. Zabih. "A maximum likelihood approach to parallel imaging with coil sensitivity noise." In: *IEEE Trans. Med. Imag.* 26.8 (Aug. 2007), 1046–57. DOI: 10.1109/TMI.2007.897364 (cit. on p. 7.40).

ying:07:jir
[170] L. Ying and J. Sheng. "Joint image reconstruction and sensitivity estimation in SENSE (JSENSE)." In: *Mag. Res. Med.* 57.6 (June 2007), 1196–1202. DOI: 10.1002/mrm.21245 (cit. on p. 7.40).

uecker:08:irb
[171] M. Uecker et al. "Image reconstruction by regularized nonlinear inversion - Joint estimation of coil sensitivities and image content." In: *Mag. Res. Med.* 60.3 (Sept. 2008), 674–82. DOI: 10.1002/mrm.21691 (cit. on p. 7.40).

keeling:12:ais
[172] S. L. Keeling et al. "An image space approach to Cartesian based parallel MR imaging with total variation regularization." In: *Med. Im. Anal.* 16.1 (2012), 189–200. DOI: 10.1016/j.media.2011.07.002 (cit. on p. 7.40).

majumdar:12:clm
[173] A. Majumdar and R. K. Ward. "Calibration-less multi-coil MR image reconstruction." In: *Mag. Res. Im.* 30.7 (2012), 1032–45. DOI: 10.1016/j.mri.2012.02.025 (cit. on p. 7.40).

knoll:12:piw
[174] F. Knoll et al. "Parallel imaging with nonlinear reconstruction using variational penalties." In: *Mag. Res. Med.* 67.1 (2012), 34–41. DOI: 10.1002/mrm.22964 (cit. on p. 7.40).

padormo:15:ppr
[175] F. Padormo et al. "PRIMO: Precise radiofrequency inference from multiple observations." In: *Mag. Res. Med.* (2015). DOI: 10.1002/mrm.25404 (cit. on p. 7.40).

benning:15:paw
[176] M. Benning et al. *Preconditioned ADMM with nonlinear operator constraint*. 2015. URL: http://arxiv.org/abs/1511.00425 (cit. on p. 7.40).

huang:05:aop
[177] F. Huang et al. "Application of partial differential equation-based inpainting on sensitivity maps." In: *Mag. Res. Med.* 53.2 (Feb. 2005), 388–97. DOI: 10.1002/mrm.20346 (cit. on p. 7.40).

keeling:04:ava
[178] S. L. Keeling and R. Bammer. "A variational approach to magnetic resonance coil sensitivity estimation." In: *Appl. Math. Comp.* 158.2 (Nov. 2004), 53–82. DOI: 10.1016/j.amc.2003.08.110 (cit. on p. 7.40).

lin:03:awb
[179] F. H. Lin et al. "A wavelet-based approximation of surface coil sensitivity profiles for correction of image intensity inhomogeneity and parallel imaging reconstruction." In: *Hum. Brain Map.* 19.2 (Mar. 2003), 96–111. DOI: 10.1002/hbm.10109 (cit. on p. 7.41).

cao:05:eoi
[180] M. Cao, V. A. Stenger, and W. Eddy. "Estimation of images and sensitivities for multi-coil MRI." In: *Proc. Intl. Soc. Mag. Res. Med.* 2005, p. 2447. URL: http://cds.ismrm.org/ismrm-2005/Files/02447.pdf (cit. on pp. 7.41, 7.42).

roemer:90:tnp
[181] P. B. Roemer et al. "The NMR phased array." In: *Mag. Res. Med.* 16.2 (Nov. 1990), 192–225. DOI: 10.1002/mrm.1910160203 (cit. on p. 7.41).

bydder:02:cos
[182] M. Bydder, D. J. Larkman, and J. V. Hajnal. "Combination of signals from array coils using image-based estimation of coil sensitivity profiles." In: *Mag. Res. Med.* 47.3 (Mar. 2002), 539–48. DOI: 10.1002/mrm.10092 (cit. on p. 7.41).

griswold:02:gap
[183] M. A. Griswold et al. "Generalized autocalibrating partially parallel acquisitions (GRAPPA)." In: *Mag. Res. Med.* 47.6 (June 2002), 1202–10. DOI: 10.1002/mrm.10171 (cit. on p. 7.42).

wang:00:dop
[184] Y. Wang. "Description of parallel imaging in MRI using multiple coils." In: *Mag. Res. Med.* 44.3 (Sept. 2000), 495–9. DOI: 10.1002/1522-2594(200009)44:3<495::AID-MRM23>3.0.CO;2-S (cit. on p. 7.43).

collins:98:dac
[185] D. L. Collins et al. "Design and construction of a realistic digital brain phantom." In: *IEEE Trans. Med. Imag.* 17.3 (June 1998), 463–8. DOI: 10.1109/42.712135 (cit. on p. 7.43).

lai:10:elr
[186] P. Lai et al. "Efficient L1SPIRiT reconstruction (ESPIRiT) for highly accelerated 3D volumetric MRI with parallel imaging and compressed sensing." In: *Proc. Intl. Soc. Mag. Res. Med.* 2010, p. 345. URL: http://archive.ismrm.org/2010/0345.html.

walsh:00:aro
[187] D. O. Walsh, A. F. Gmitro, and M. W. Marcellin. "Adaptive reconstruction of phased array MR imagery." In: *Mag. Res. Med.* 43.5 (May 2000), 682–690. DOI: '10.1002/(SICI)1522-2594(200005)43:5<682::AID-MRM10>3.0.CO;2-G'.

zhang:13:ccf
[188] T. Zhang et al. "Coil compression for accelerated imaging with Cartesian sampling." In: *Mag. Res. Med.* 69.2 (Feb. 2013), 571–82. DOI: 10.1002/mrm.24267.

lee:16:mbc
[189] J. Lee, J. Shin, and D-H. Kim. "MR-based conductivity imaging using multiple receiver coils." In: *Mag. Res. Med.* 76.2 (Aug. 2016), 530–9. DOI: 10.1002/mrm.25891.

park:86:rvr
[190] H. W. Park, M. H. Cho, and Z. H. Cho. "Real-value representation in inversion-recovery NMR imaging by use of a phase-correction method." In: *Mag. Res. Med.* 3.1 (Feb. 1986), 15–23. DOI: 10.1002/mrm.1910030104.

liu:90:aap
[191] J. Liu and J. L. Koenig. "An automatic phase correction method in nuclear magnetic resonance imaging." In: *J. Mag. Res.* 86.3 (Feb. 1990), 593–604. DOI: 10.1016/0022-2364(90)90036-9.

sarkar:99:aoh
[192] S. Sarkar et al. "Applications of high-resolution echoplanar spectroscopic imaging for structural imaging." In: *J. Mag. Res. Im.* 10.1 (July 1999), 1–7. DOI: '10.1002/(SICI)1522-2586(199907)10:1<1::AID-JMRI1>3.0.CO;2-C'.

bretthorst:08:apo-1
[193] G. L. Bretthorst. "Automatic phasing of MR images. Part I: Linearly varying phase." In: *J. Mag. Res.* 191.2 (Apr. 2008), 184–92. DOI: 10.1016/j.jmr.2007.12.010.

hardy:09:apc
[194] E. H. Hardy et al. "Automated phase correction via maximization of the real signal." In: *Mag. Res. Im.* 27.3 (Apr. 2009), 393–400. DOI: 10.1016/j.mri.2008.07.009.

cauley:17:awc
[195] S. F. Cauley et al. "Autocalibrated wave-CAIPI reconstruction; Joint optimization of k-space trajectory and parallel imaging reconstruction." In: *Mag. Res. Med.* 78.3 (Sept. 2017), 1093–9. DOI: 10.1002/mrm.26499.

levine:17:dda
[196] E. Levine and B. Hargreaves. "Differential domain analysis for 3D Cartesian sampling." In: *Proc. Intl. Soc. Mag. Res. Med.* 2017, p. 0443.